Design study of a Compton camera for prompts-gamma imaging during ion beam therapy

Marie-Hélène Richard

▶ **To cite this version:**

Marie-Hélène Richard. Design study of a Compton camera for prompts-gamma imaging during ion beam therapy. Other [cond-mat.other]. Université Claude Bernard - Lyon I, 2012. English. NNT : 2012LYO10124 . tel-00934715

HAL Id: tel-00934715

https://theses.hal.science/tel-00934715

Submitted on 22 Jan 2014

HAL is a multi-disciplinary open access archive for the deposit and dissemination of scientific research documents, whether they are published or not. The documents may come from teaching and research institutions in France or abroad, or from public or private research centers.

L'archive ouverte pluridisciplinaire **HAL**, est destinée au dépôt et à la diffusion de documents scientifiques de niveau recherche, publiés ou non, émanant des établissements d'enseignement et de recherche français ou étrangers, des laboratoires publics ou privés.

Thèse de l'université de Lyon

⋆

délivrée par
l'université Claude Bernard Lyon1

Ecole doctorale PHAST

⋆

DESIGN STUDY OF A COMPTON CAMERA FOR PROMPT-GAMMA IMAGING DURING ION BEAM THERAPY

⋆

Marie-Hélène RICHARD

dirigée par

Cédric RAY ,
Institut de Physique Nucléaire de Lyon (IPNL)
ET
Jean Michel LETANG
Centre de Recherche en Acquisition et Traitement de l'Image pour la Santé (CREATIS)

⋆

septembre 2009 - septembre 2012

Contents

CHAPTER 1

Introduction

1 Ion beam therapy

1.1 Principles of ion beam therapy

Ion beam therapy was first proposed in 1946 by R. Wilson [Wilson1946]. The idea was to use the physical properties of ions to improve the precision in radiotherapy treatments. Fig. 1 illustrates the depth dose curve of 21 MV photons, 148 MeV protons and 270 MeV/u carbon ions in water. Carbon ions and protons deposit a maximum of energy at the end of their trajectory in what is called the Bragg peak. On the contrary the dose deposited by photons is maximum close to the beginning of their trajectory and decreases exponentially. Thus in classical radiotherapy multiple irradiation fields corresponding to different incidence angles are needed to concentrate the dose in the tumour. Yet this leads to a large quantity of low dose in the surrounding tissues. In ion beam therapy, with only one or two irradiation fields it is possible to deliver an homogeneous dose to the tumour with a largely reduced dose to the surrounding tissue. Fig. 2 shows the comparison of two treatment plans of a target volume in the base of the skull for a two carbon-ion fields irradiation (a) and a nine fields intensity modulated radiotherapy (IMRT) irradiation (b). We observe indeed a large reduction in the total dose to the healthy tissues and the organ at risk.

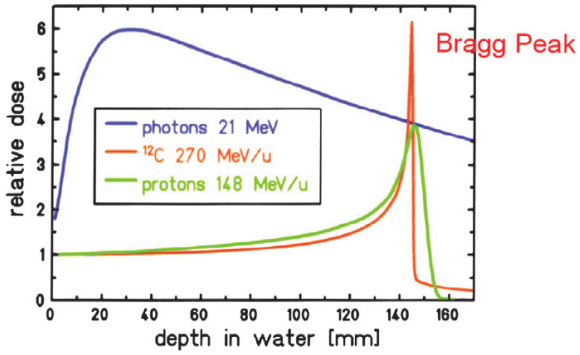

Figure 1: Depth dose distribution for photons and monoenergetic Bragg curves for carbon ions and protons [Fokas2009].

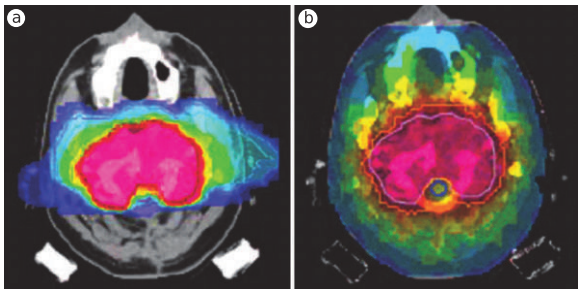

Figure 2: Comparison of treatment plans for a large target volume in the base of the skull. a: Plan for carbon ions (two fields). b: Plan for IMRT (nine fields) [Durante2010].

The therapeutic interest of ions heavier than protons also relies on their high relative biological effectiveness (RBE) [Fokas2009]. Indeed when increasing the charge of the incident ions, the ionisation density increases and so does the probability of severe DNA damage. The RBE depends also on the energy of the ions. Slow ions have a high RBE and fast ions have a low RBE (i.e. comparable to that of photons). In particular, with carbon ions, RBE is low in the entrance channel (i.e. the healthy tissues) and high in the Bragg peak region (i.e. the tumour). Carbon ion irradiation mainly targets inoperable or radio-resistant tumours. Ions heavier than carbon are not suitable for therapy because they are characterised first by a too high RBE in the entrance channel and by a too large fragmentation. The use of ions lighter than carbon such as helium, lithium or boron, is the subject of on-going investigations: they present less lateral scattering and a sharper distal edge than protons. Moreover the required accelerators are smaller, and thus cheaper and less technically demanding, than those needed in carbon therapy.

1.2 Beam delivery

Basically, in ion beam therapy, two types of accelerators are used: synchrotrons and cyclotrons. The main difference concerns the energy selection and the time structure of the beam. Cyclotrons deliver a continuous beam of fixed energy which has to be degraded with passive absorbers. Synchrotrons deliver a cyclic beam divided in spills. The beam energy can be varied from spill to spill without any passive absorber. In proton therapy both accelerators are used, see for instance [Schardt2010] for more details. For technical reasons, in carbon therapy only synchrotrons are used currently. A compact superconducting isochronous cyclotron

has been designed by the IBA-JINR collaboration and will be built within the framework of the ARCHADE project in Caen (France) [Jongen2010].

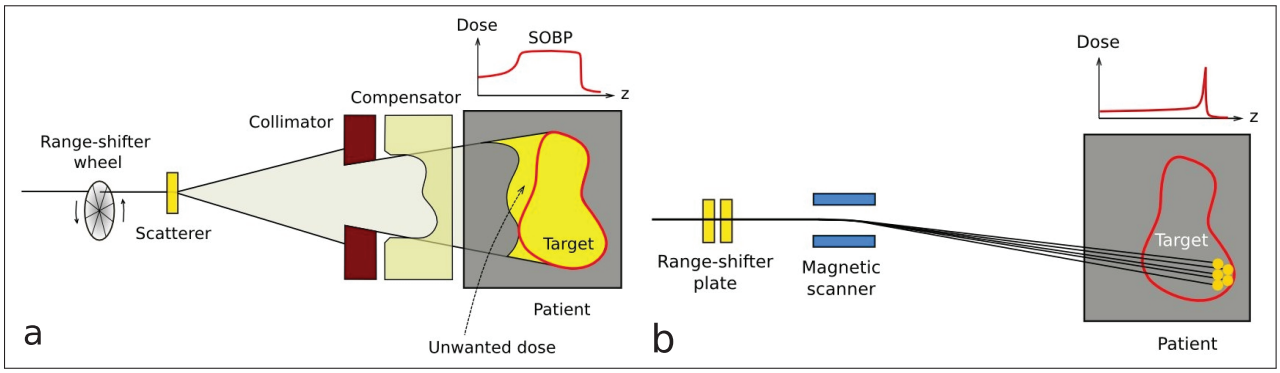

Figure 3: Basic principle of a: passive beam shaping and b: scanning systems.

Irradiation with monoenergetic ion beams would lead to very narrow dose distributions. To distribute the beam over the planned target volume (PTV) accurately and homogeneously, different energies have to be superimposed. The resultant dose distribution is called spread-out Bragg peak (SOBP). To produce a SOBP, two different beam delivery systems are used: passive beam shaping and scanning systems. The basic principles of these two techniques are represented on Fig. 3. In a passive system, a narrow monoenergetic beam is broadened by a scattering device and spread out by a range shifter wheel. Then the beam is shaped like the tumour with a patient specific collimator and a patient specific compensator. In an active system, the tumour is irradiated by a series of thin pencil beams. No patient specific devices are required. The energy and angle of each beam is fixed by means of, respectively, a range shifter plane and a magnetic scanner. The passive system has been used until now in almost all centres, yet the trend is toward scanning techniques [Gottschalk2008]. Indeed, with scanning techniques, the neutron contamination is significantly reduced. Moreover we obtain less unwanted dose as illustrated on Fig. 3 and a better conformation is achievable. Specific problems as penumbra between the spots and organ motion need to be considered carefully during the planning.

1.3 Uncertainties

During an irradiation, the possible sources of error in the dose delivery are: patient mispositionning, evolution of patient or/and tumour morphology and treatment planning errors. In classical radiotherapy, they are taken into account by irradiating a volume slightly larger than the tumour itself. This volume is called the planning target volume (PTV), it includes the clinical target volume (CTV, i.e. the tumour volume) and extra margins. To limit these errors, and thus reduce as much as possible the margins, the treatment rooms are equipped with patient positioning systems and position verification systems composed of X-ray imaging devices. The patient position can currently be verified with an absolute accuracy of approximately 2 mm [Jakel2001].

The sharpness of the dose distribution makes an ion irradiation more sensitive than a photon irradiation to any of these deviations: an ion range shorter than prescribed results in serious underdosage of the target volume, and a higher range could damage an organ at risk beyond the tumour in addition to an underdosage in the target volume. Moreover, the use of ion beams introduce additional uncertainties. In particular, the calibration between the CT images and the ion stopping powers during the elaboration of the treatment plan can lead to an uncertainty of up to 3% on the ion ranges [Smith2009]. For these reasons the margins are increased [ICRU2007Report78], and this limits the achievable conformation of the dose to the tumour. For instance, at the Massachusetts General Hospital (MGH), treatment planning assumes an uncertainty in the proton beam range of 3.5 % of the range plus an additional 1 mm [Paganetti2012]. Other centres follow similar margin recipes. Real time monitoring of the range seems necessary to reduce these margins, fully exploit the advantages of ion beam and detect as soon as possible during the irradiation any deviation of one

of the irradiation parameters. The current verification systems are not sufficient and specific devices need to be developed.

2 Monitoring of the beam

Ion beam therapy require beam energies high enough to treat tumours located at depths up to 30 cm. This corresponds to energies up to 220 MeV for protons, 430 MeV/u for ^{12}C ions. At these energies, the main interactions of the incident ions are inelastic collisions with the atomic electrons of the target. These collisions are responsible for dose deposition. As the ions penetrate into matter, their velocity decreases and the corresponding stopping power increases. As a consequence, the energy loss plotted as a function of target depth results in a sharp peak near the stopping point, the so-called Bragg peak. The peak is broadened by the statistical fluctuations of the number of interactions over the ion paths. Ions also undergo elastic Coulomb interactions with the target nuclei. This causes a lateral spread of the beam.

In addition, some ions undergo a collision with an atomic nucleus (nuclear reaction) (about 20% for 160 MeV protons in water [Gottschalk2008], 15% for 100 MeV/u carbon ions and 70% for 400 MeV/u carbon ions in water [Schall1996]). For geometrical reasons, the most frequently occurring nuclear reactions are peripheral collisions where the beam particles may lose one or several nucleons [Gunzert-Marx2008]. This process can be described by the abrasion-ablation model as a two step process. In the first step nucleons are abrated in the overlapping reaction zone ("fireball"), prefragments are produced within approximately 10^{-22} s, while the outer spectator nucleons are only slightly affected. In the second step (ablation), the remaining projectile and target fragments as well as the fireball de-excite by evaporating nucleons and light clusters. While neutrons and clusters from target-like fragments are emitted isotropically, the projectile-like fragments (in the case of carbon ions) keep a direction very close from the direction of the incident ion and continue to interact in the target until either they stop or they undergo a nuclear reaction.

As all primary ions are stopped within the target, the only way to control dose deposition is to detect the secondary particles that have enough energy to escape the target and to reconstruct the distribution of their emission position. Yet while dose is deposited through electronic processes, these particles are emitted through nuclear reactions. This may cause differences between the distribution of their emission position and the dose distribution and specific calibration would be needed for a quantitative correspondence.

It is possible to detect either delayed emission of radiation from the decay of unstable nuclei formed in the target or prompt emission of photons or light charged particles. The detection of the β^+ emitter fragments with positron emission tomography (PET) is currently used in clinical routine. Other techniques as prompt γ-ray imaging with either a collimated or a Compton camera and proton interaction vertex imaging (PIVI) based on secondary, or higher order, proton detection are also investigated.

2.1 Positron emission tomography

The only technique which is currently used in clinical routine is PET imaging [Enghardt2004]. The success of this technique relies on the good correlation between the β^+ activity distribution and the dose distribution (see Fig. 4). To implement it into clinical centres, two strategies can be applied. An in-beam system consisting of a partial ring can be integrated into the treatment room, measuring the activity contribution from short-lived emitters such as ^{15}O (2 min half-life). Such a system has been integrated into the carbon ion therapy beam line at the heavy ion synchrotron of GSI and it has been employed routinely for monitoring almost all of the 440 patients treatments delivered there. It was demonstrated that in-beam PET is capable of revealing deviations in the maximum particle ranges due to (i) inaccuracies of the physical beam model in treatment planning, (ii) minor positioning errors and (iii) particle range deviations due to local modifications of the density distributions relative to the planning CT [Enghardt2004]. A technically less complex alternative consists in using commercial full-ring PET scanners, measuring the activity contribution from long-lived emitters such as ^{11}C (20 min half-life) shortly after treatment (offline). The choice of the optimal strategy is still under discussion [Parodi2008].

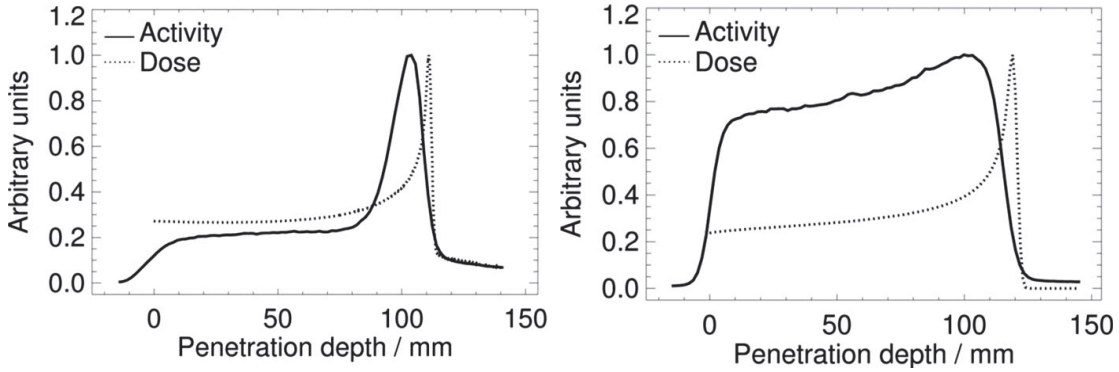

carbon ions at 260 MeV/u protons at 140 MeV

Figure 4: Autoactivation of thick PMMA targets by beams of 260 MeV/u carbon ions (left) and 140 MeV protons (right). The solid line shows the depth profile of the measured β^+ activity. For comparison the depth-dose profile of the primary beam is shown by a dotted line [ParodiPhd2004].

In both cases, the data acquired is reconstructed after the treatment fraction. The deviations that might have been detected can only be taken into account in the next treatment fraction. Moreover image quality is limited by the low induced activity, typically ten times lower than activities injected in nuclear medicine applications, and by the washout effect caused by metabolism, especially for the offline technique. Dose and range monitoring during the treatment fraction is not possible with the current technology. Because it would decrease significantly the reconstruction time, time of flight (TOF) PET might overcome this problem [Crespo2007].

2.2 Prompt γ-ray imaging

As mentioned before, an other possibility is to detect the prompt γ-rays emitted subsequently to the nuclear reactions. We can divide the gamma energy spectra in three domains. Over 30 MeV γ-rays are mainly produced by nucleon-nucleon bremsstrahlung, between 10 and 30 MeV they are mainly produced by giant dipole resonance deexcitation and under 10 MeV they are mainly produced by excited fragments during the last step of the nuclear reaction. Fig. 5 illustrates this energy spectrum in the case of the irradiation of a water target by a ^{12}C ion beam at 310 MeV/u. As they are emitted almost instantaneously (within times well below ns), their distribution is not affected by physiological processes and their is no wash-out effect.

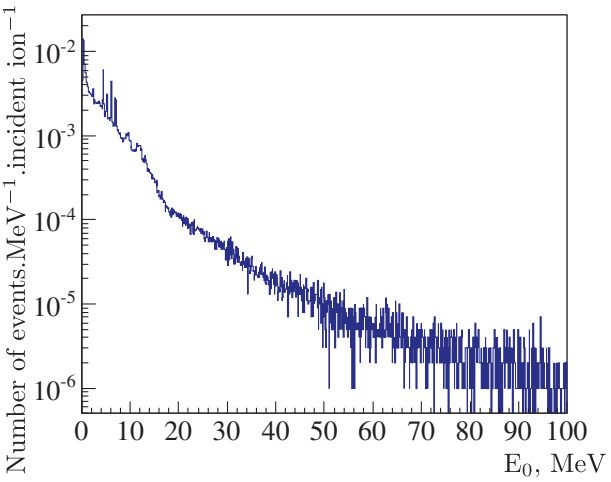

Figure 5: Emission spectrum (Geant4 simulations) in 4π steradians of prompt γ-rays between 0.5 and 100 MeV for ^{12}C ions at 310 MeV/u in water.

The feasibility of range monitoring in ion beam therapy by means of prompt γ-ray measurements was

first supported in 2003 by Stichelbaut *et al.* [Stichelbaut2003]. In 2006 Min *et al.* verified experimentally the correlation between the prompt γ-ray and the dose profile for monoenergetic proton beams in a PMMA target with a heavily collimated 4 cm thick CsI detector [Min2006]. The 71 cm thick collimator consisted of three layers: a parafin layer and a B_4C powder to moderate and capture the fast neutrons also emitted during the nuclear reactions and a lead layer to collimate the γ rays. In fact, even if the secondary neutron momentum is mainly oriented in the beam direction, the neutron rates at 90° is still comparable to the γ-ray rates. Similar measurements were performed with a 5 cm thick NaI detector by my co-workers for a carbon ion beam [Testa2008]. Collimation was reduced to a 20 cm thick lead collimator and prompt γ-rays were discriminated from neutrons by a time of flight (TOF) technique. This is possible provided the distance between the target and the detector is sufficiently large. Fig. 6 shows the profile corresponding to the γ-ray signal and the one corresponding to the neutron signals. It can be observed that the fall-off of the prompt γ-ray profile corresponds to the expected value of the ion range whereas the neutron profile is almost flat because the lead collimator does not allow an efficient attenuation of neutrons.

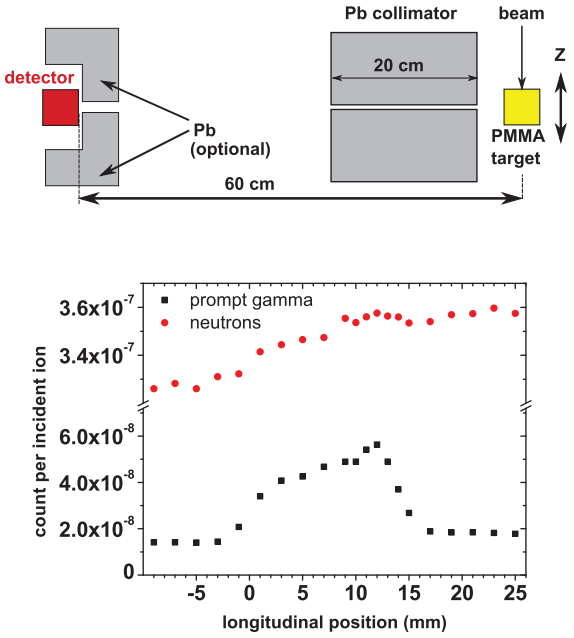

Figure 6: Detection rates (E>1 MeV) as a function of longitudinal position of target for two different TOF ranges: 2<TOF<10 ns (prompt γ-rays, squares) and TOF>10 ns (mostly neutrons, circles). The experiment used a beam of 73 MeV/u $^{13}C^{6+}$ ions. [Testa2008]

To confirm the clinical applicability of prompt γ-ray imaging, a detection efficiency high enough to reconstruct relevant information as soon as possible during the irradiation must be achieved. The most critical information is the distal position of the dose distribution, for which a millimetric precision is desired. Ideally, the detection system should be able to determine this position after the irradiation of each pencil beam (in the case of active beam delivery) or after the first mGys (in the case of passive beam delivery).

Two types of detection systems can be considered: either a mechanically collimated detector, γ camera like or an electronically collimated detector, Compton camera like. A multi-slit collimated detector capable of acquiring scans in a single acquisition is under development at IPNL [TestaM2010]. Fig. 7 summarises the principle of the proposed system. It combines a beam hodoscope, a multi-slit collimator and several scintillator detectors. The prompt γ-ray emission points are reconstructed by intersecting the ion trajectories (given by the hodoscope) with the γ-ray trajectories (given by the camera). TOF measurements between the hodoscope and the scintillators are planned in order to suppress the neutron background. The main advantage of such a system is its relative simplicity. Yet, the collimator needs to be designed with care, as the γ-ray energy is significantly higher compared to the energy used in nuclear medicine (of the order of a few hundred keV). A Compton camera is an electronically collimated system and it is likely to provide a higher detection efficiency. It might even provide a better spatial resolution. The aim of my PhD is to

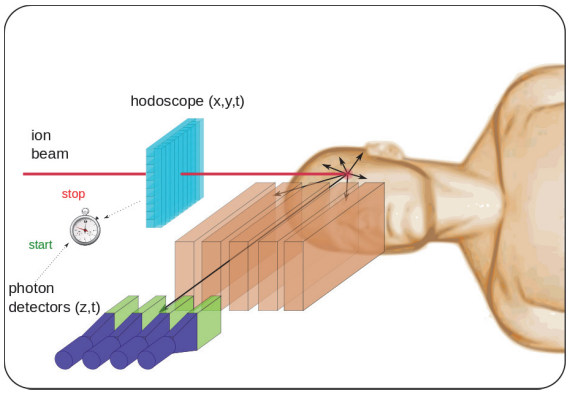

Figure 7: Principle of prompt γ-ray imaging with collimated scintillators.

specially study this type of camera.

2.3 Interaction vertex imaging

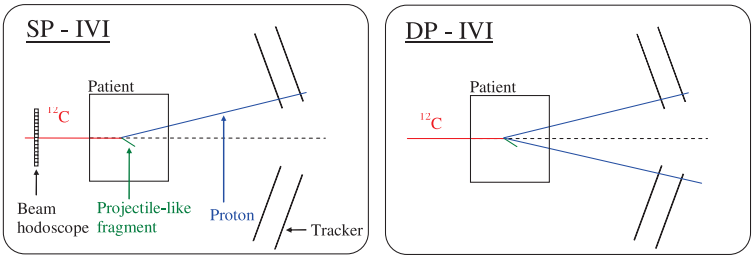

Figure 8: Principle of single proton interaction vertex imaging (SP-IVI) on the left and of double proton interaction vertex imaging (DP-IVI) on the right (adapted from [Henriquet2012]).

Another method called Interaction Vertex Imaging (IVI) is under investigation. It is based on secondary, or higher order, proton detection [Amaldi2010][Henriquet2012]. In the case of carbon ion therapy, it has been shown that a large number of protons are generated during nuclear collisions along the primary ion path [Gunzert-Marx2008]. These protons are highly forward oriented and their velocity is close to the one of the incident ion. So they can be detected with a particle detector located downstream the patient. Fig. 8 illustrates two different approaches of IVI. The fragmentation vertex location can be reconstructed by intersecting the incident ion trajectory, given by the hodoscope, and the secondary proton trajectory, given by a set of tracking detectors (single proton interaction vertex imaging, SP-IVI). Or it can be reconstructed by intersecting the trajectories of two protons emitted from the same interaction vertex given by two different sets of tracking detectors (double proton interaction vertex imaging, DP-IVI).

3 Monte Carlo simulations in ion beam therapy

Monte Carlo simulations are widespread in medical physics and several codes are available for a very broad range of applications. The most widely applied codes to conventional radiation therapy with photon and electron beams are EGS (Electron Gamma Shower) [Bielajew1994] and PENELOPE (Penetration and Energy Loss Of Positrons and Electrons) [Baro1995]. Other multipurpose simulation codes like FLUKA [Ballarini2007], Geant4 [Agostinelli2003], MCNPX [James2006], SHIELD-HIT [Gudowska2004] and PHITS [Nose2005] have gained high potential in ion beam therapy applications since they handle hadronic interactions. Besides and more specifically for the field of medical imaging, dedicated Monte Carlo tools for PET and SPECT like SimSET and more recently GATE [Jan2004] are rapidly gaining interest in the nuclear medicine community. I used Geant4 because it is flexible in geometry and physics modeling and because my coworkers and I had prior experience with it.

The simulations of ion beam therapy situations require the accurate modelling of the interaction with matter of photons, electrons, positrons and hadrons (protons, neutrons and light ions). The interactions of photons, positrons and electrons are well known and the corresponding interaction models are well documented and validated, see for instance [Cirrone2010], [Kadri2007] and [Mantero2007]. For the interactions of hadrons with matter, models for energies ranging from 10 to 250 MeV for protons and from 10 to 400 MeV/nucleon for ions and for neutrons are required. It was shown that the current simulation tools are capable of reproducing with a satisfactory agreement the depth dose profiles (i.e. the electromagnetiec physics) in water [Grevillot2010, Lechner2010] in the case of proton and carbon ion therapy.

An accurate modelling of the nuclear reactions and of the resulting secondary particle distributions are needed because, especially in the case of carbon therapy, nuclear reactions lead to significant effects at large penetration depths on dose deposition. This is due to differing ranges and angular distributions of the fragments. This is also needed for simulations of imaging techniques aiming at in vivo dose monitoring. Despite the recent efforts to improve the modelling of nuclear reactions, discrepancies between simulations and measurements remain (see for instance [Bohlen2010] and [Lefoulher2010]).

To describe the inelastic interactions of hadrons, two models are widely used in Monte Carlo simulations: the QMD model [Koi2010] and the binary cascade [Folger2004]. The binary cascade applies to protons and neutrons and for heavier ions, an extension of the binary cascade, the binary light ion reaction applies. In these two models, the inelastic reaction is divided in two parts: a dynamic part modelling the collision, and a static part modelling the deexcitation. Concerning the dynamic part, there are two main differences between the models: first, the binary cascade does not account for interactions between nucleons of the same nucleus whereas QMD does; second, the Hamiltonian is calculated from a time-independent potential in the binary cascade whereas the potential is dynamically changed in QMD. The deexcitation part is common to both models except that the binary cascade includes a transition between the two parts (precompound model). So, from a theoretical point of view, the QMD model is more detailed and is expected to give better results. From an experimental point of view, Böhlen *et al.* showed that the QMD model is preferable over the binary light ion reaction model for the correct prediction of fragment yields in the case of a 400 MeV/u carbon ion beam in a water target [Bohlen2010].

Co-workers are currently working on improving these different models in order to define the most suitable set of models to be used and to achieve the desired prediction accuracy required in the context of development and optimisation of beam monitoring devices [Dedes2012]. The improvement of the models are checked against theoretical quantities such as ground state nuclear properties, and thoroughly validated with experimental defined observables such as secondary particle emission properties.

4 Context and objective of the PhD

Since the first treatment with a proton beam in 1954 in Berkeley, USA, proton therapy has become an established clinical modality. At the end of 2010, about 68000 patients had been treated with proton beams in the world, including 9400 in France [Amaldi2011]. Carbon therapy is more specific, because of the high biological efficiency of carbon ions, and more complex to operate. Currently it is limited to few centres in the world. About 6000 patients have been treated with carbon ion beams since the first treatment in Chiba, Japan, in 1994. As a result of the promising clinical results obtained with carbon-ion beams in Japan and in Germany, the plans for new clinical centres for heavy-ion or combined proton and heavy-ion therapy have recently received a substantial boost. Yet, several research issues, both clinical and technical, are currently under study to enable a wide application of carbon therapy. The main challenges are related to the development of more compact and cheaper acceleratosr and to the capability to treat moving targets with scanning beams.

In France, proton therapy is performed in Orsay and in Nice since 1991. Another proton therapy centre is planned in Toulouse. In Caen, the ARCHADE centre will be devoted exclusively to research in ion beam therapy. In Lyon, the ETOILE centre is foreseen to treat the first patient in 2016. It will includes both proton and carbon ion beams. As a consequence, the ion-beam-therapy research pole in Lyon is quite active.

My thesis was carried out in the context of a collaboration between the group “Imagerie tomographique et thérapie par rayonnements“ (tomographic imaging and therapy with radiation) from CREATIS laboratory

and the group "Collisions atomiques dans les solides et physique pour l′hadronthérapie et les applications Biomédicales" (Atomic Collisions in Solids and Physics for Hadrontherapy and biomedical applications) from the Nuclear Physics Institute of Lyon (IPNL). The background of the people involved in this collaboration (mainly x-ray imaging and algorithmics for the people from CREATIS, nuclear physics and electronics for the people from IPNL) made it possible to work on monitoring modalities during ion beam therapy. Two different modalities are investigated: prompt γ-ray imaging and interaction vertex imaging. This work can be divided into two main tasks: first the conception and the optimisation of the detection systems by means of both simulations and experimental studies ([HenriquetPhd2011, TestaMPhd2010]) and then the improvement and the validation of the physics models used in the simulations [LefoulherPhd2010].

The objective of my thesis is to perform, by means of Monte Carlo simulations, a preliminary feasibility study of prompt γ-ray imaging during ion beam therapy with a Compton camera. The first step consisted in elaborating an appropriate geometry for the camera and then optimising it for this particular application. Design guidelines were to be provided to help in building a small size prototype. This prototype is being built in IPNL, within the framework of the GDRMI2B, the Regional Program of Research in Hadrontherapy, the ANR Gamhadron and FP7 ENVISION (European NoVel Imaging Systems for ION therapy) projects. These projects are presented in more details in Chap. 2.

CHAPTER 2

Prompt γ-ray imaging with a Compton camera State of the art

1 Compton effect

The Compton effect governs the interaction of photons in a Compton camera: it is an incoherent scattering of a photon with an electron. The photon with an incident energy E_0 is scattered through an angle ϑ with a remaining energy E_1. The electron is given a kinetic energy $K_e = E_0 - E_1$. The relation between E_0, ϑ and E_1 is given by the Compton equation:

$$\cos(\vartheta) = 1 - m_e c^2 \left(\frac{1}{E_1} - \frac{1}{E_0} \right), \tag{2.1}$$

where m_e is the electron mass at rest and c the speed of light.

The distribution of the Compton scattering angles is predicted with a very good approximation by the Klein-Nishina formula given in Eq. 2.2. The differential cross-section $\frac{d\sigma_e(E_0,\Omega)}{d\Omega}$ is the probability per electron that a photon undergoes a Compton scattering into a unit solid angle $d\Omega$ with an angle ϑ. It is represented for different photon incident energies in polar coordinates in Fig. 1. At high energies, there is a strong tendency for forward scattering. At low energies, the scattering angle distribution is less peaked and the probability of back-scattering is higher.

$$\frac{d\sigma_e(E_0,\Omega)}{d\Omega} = r_0^2 \left(\frac{1+\cos^2\vartheta}{2} \right) \left[\frac{1}{1+\alpha(1-\cos\vartheta)} \right]^2 \left\{ 1 + \frac{\alpha^2(1-\cos\vartheta)^2}{[1+\alpha(1-\cos\vartheta)]\,(1+\cos^2\vartheta)} \right\}, \tag{2.2}$$

where $\alpha = \frac{E_0}{m_e c^2}$ and r_0 is the classical electron radius given by $r_0 = \frac{e^2}{4\pi\varepsilon_0 m_e c^2}$ where e is the elementary charge.

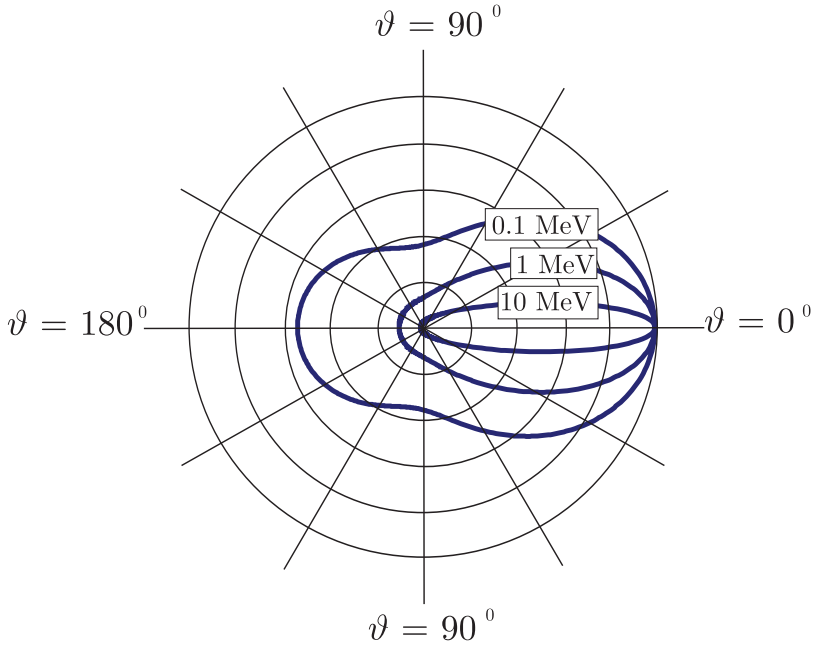

Figure 1: Klein-Nishina cross-section as a function of the Compton scatter angle ϑ for different energies. Each curve was normalised for $\vartheta = 0°$.

Eq. 2.1 and Eq. 2.2 wrongly assume that the struck electron is unbound and at rest. The electron binding energy can be taken into account in the differential cross-section by multiplying the Klein-Nishina formula by a correction factor $S(q,Z)$ called the incoherent scattering function which depends on q, the momentum transfer to the electron after scattering, and Z, the atomic number. This factor decreases the cross section at small scattering angles (i.e. in the forward direction), and increases it at large angles.

The momentum of the struck electron introduces an uncertainty in the energy spectrum of the scattered photons. For a given scattering angle, the value of the scattered photon energy E_1 is not unique. It is given

by :

$$E_1 = \left[\frac{p_z cq}{E_0 m_e c} + 1\right]\left[\frac{E_0}{1+\alpha(1-\cos\vartheta)}\right], \tag{2.3}$$

where p_Z is the projection of the initial momentum of the electron on the direction of scattering. This effect is called Doppler broadening by the imaging scientific community, and Compton profile by physicists. The study of Compton profiles in itself is of interest for the electronic structure of atoms, molecules and solids.

The distribution of azimuthal scattering angles in photon interactions, and in particular in Compton scattering, is modulated by polarisation. This property can be used to determine the photon degree and angle of polarisation [Takeda2010]. Because of these polarisation effects, even for randomly polarised photons, after two Compton scatterings there is a high probability that $\mathbf{k_0}$, $\mathbf{k}_1$ and $\mathbf{k}_2$ are coplanar, where the $\mathbf{k}_i$ are respectively the photon momentum before the first Compton scattering, after the first Compton scattering and after the second Compton scattering [Wightman1948]. In other words, the distribution of the azimuthal angle of $\mathbf{k}_2$ around the axis of $\mathbf{k}_1$ is maximal at 0° and minimal at 90°. This property can be used in multiple scattering Compton Cameras to improve the reconstruction [Dogan1992].

2 Compton cameras

2.1 General principle

Compton cameras are electronically collimated emission photon imaging devices. They were designed as alternatives to the classical gamma cameras to image photons with higher energies. Indeed, whereas mechanical collimators are efficient only until a few hundreds keV, the useful range of Compton cameras extends to a region from a few hundreds keV to beyond a few MeV where the most likely interaction process is Compton scattering. Of course the energy range where Compton interaction dominates depends on the material (see Fig. 2). Compton cameras also provide a larger efficiency, a larger field of view and the ability to reconstruct 3D images without having to move the camera.

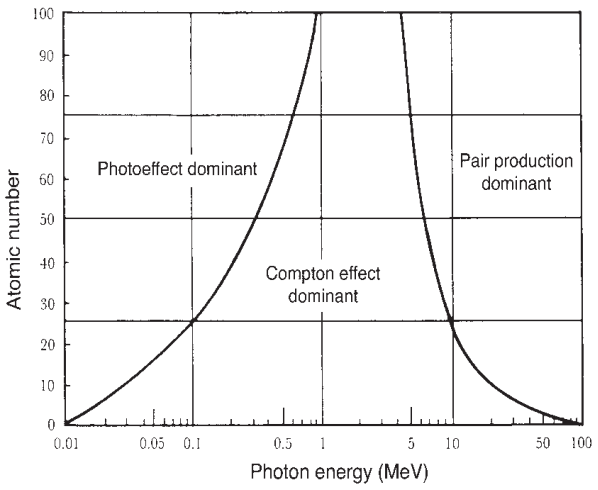

Figure 2: Regions of relative predominance of the three main forms of photon interaction with matter. The left curve represents the region where the atomic attenuation coefficients for the photoelectric and Compton effects are equal, the right curve is for the region where the atomic attenuation Compton coefficient equals the atomic attenuation pair production coefficient [Podgorsak2003].

In general, a Compton camera consists of one scatter detector and one absorber detector [Phillips1995]. Photons scatter in the first detector and are absorbed in the second one. Provided that photons are totally absorbed in the second detector or their incident energy is known, it is possible, from the measurement

of the deposited energies and interaction positions in both detectors, to reconstruct cones containing their incident trajectories (see Fig. 3). The apex of these cones are the interaction points in the scatter detector, their axis are the lines formed by the interaction points in the scatter detector and by the interaction points in the absorber detector. Finally, their aperture angles ϑ are given by the following equations:

$$\cos(\vartheta) = 1 - m_e c^2 \left(\frac{1}{E_1} - \frac{1}{E_0} \right) \tag{2.4}$$

$$E_0 = \text{edep}_1 + E_1 \tag{2.5}$$

$$E_1 = \text{edep}_2 \tag{2.6}$$

where ϑ is the scattering angle of the photon in the first detector, E_0 the photon incident energy, E_1 its energy after the Compton scattering, edep_1 and edep_2 the energies deposited in each detector by the photon, m_e the electron mass at rest and c the speed of light. Eq. 2.6 is verified only if the photon is fully absorbed in the second detector. At the end, the source position distribution can be reconstructed by intersecting all the reconstructed cones (see Fig. 3).

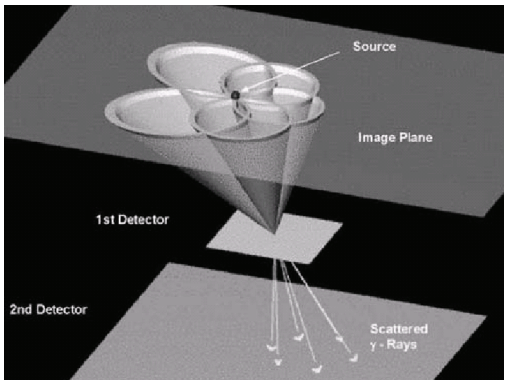

Figure 3: General principle of a Compton camera [Studen2004], see text for more details.

2.2 Applications

Compton cameras were first built and tested for applications in astronomy and in nuclear medicine. In astronomy they are used to image photons with an energy between approximately 0.4 and 50 MeV. This energy regime is crucial for the study of a rich variety of high-energy astrophysical processes [Herzo1975]. In nuclear medicine, where extended monochromatic sources are observed, the idea is to improve the cameras used for Single Photon Emission Computed Tomography (SPECT), either by lowering the delivered dose for a given image quality or by improving image quality while delivering a similar dose to the patient [Singh1983]. Compton cameras could also be used to image higher energy isotopes provided medical applications are found. More recently, Compton cameras have been tested in the field of industrial imaging, homeland security [Niedermayr2005] and ion beam therapy.

Because the prompt γ-ray incident energy ranges from a few hundreds keV to a few MeV, a Compton camera meets the requirements of on-line monitoring purposes. Note that the polychromatic nature of the energy spectrum implies that the photon incident energy is unknown. This application of Compton cameras is currently investigated by several groups worldwide. It was first proposed in 2009 by Kang *et al.* [Kang2009]. It is also investigated within the framework of the European FP7 ENVISION (European NoVel Imaging Systems for ION therapy) project. This project started in 2010, it involves all the major actors in the field of ion beam therapy in Europe. It addresses the problem of in-vivo monitoring of delivered dose and quality assurance for clinical therapy. The proposed developments are divided in five strongly correlated fields: in-beam Positron-Emission-Tomography (PET) monitoring, monitoring with single particles, in-vivo dosimetry and moving organs, in-vivo dosimetry and treatment planning and Monte Carlo simulations of in-vivo dosimetry. Three different Compton cameras are compared within the work package

3 (In-beam single particle tomography). The different options which are currently under investigation are presented in more details in § 2.4.

2.3 Figures of merit

The performances of a Compton camera are often characterised by its detection efficiency and its spatial and/or angular resolution. Depending on the required performances for the considered application and on the photon source characteristics (mainly its energy spectrum), the geometry and the choice of the detector materials need to be optimised. Several considerations have to be taken into account:

- the detection efficiency can be separated into two components: a geometric efficiency and an interaction efficiency. The geometric efficiency is determined by the detector shapes, dimensions and the inter-detector distances. The interaction efficiency is fixed by the detector thicknesses and materials and by the source energy spectrum;
- each Compton cone is reconstructed from its apex, its axis and its aperture angle. The achievable accuracy for each of these features is fixed by the spatial resolution of the scatter detector, the spatial resolution of both detectors and the energy resolution of both detectors. Moreover, Doppler broadening introduces an additional uncertainty on the cone angle;
- reconstruction is made assuming the photon undergoes a single Compton interaction in the scatter detector without energy escape (the recoil electron deposits all its energy in the detector), and at least one interaction in the absorber detector. If the incident energy of the photon is unknown (which is the case for instance for a poly-energetic source), it is also assumed that photons are fully absorbed in the last detector. Other interaction sequences are likely to deposit energy in both the scatter and the absorber detectors. For instance, the recoil electron may escape from the scatter detector and deposit energy in the absorber detector or a photon may undergo one pair creation in the scatter detector and one of the secondary particles may escape and deposit energy in the absorber detector. Several examples of such interaction sequences are illustrated in Fig. 9 of Chap. I.1 in the case of the double scattering Compton camera. Experimentally it is not possible to distinguish between the different types of interactions. The reconstruction of these "wrong" events is a source of degradation of the camera resolution.

2.4 Detectors

Semi-conductors are often used for the scatter detector. Si detectors provide a higher percentage of Compton interactions and less Doppler broadening than other semi-conductors. Ge and CdTe detectors provide a better energy resolution and a better efficiency than Si detectors[Harkness2009, Oonuki2007]. Several thin semi-conductor detectors can be stacked to increase the detection efficiency. With a stack of scatter detector, it is possible to track the Compton electrons which escape from one of the scatter detector and deposit energy in the following ones and to reduce the reconstructed cone distribution to a small cone section. This strategy is used for instance in the MEGA telescope built in Germany for an application in astronomy by Andritschke *et al.* (see Fig. 4 (a)). A prototype consisting of 99 double-sided silicon strip detectors and a CsI absorber detector was built. It has proven the feasibility of the concept (see [Andritschke2005] for more details).

Gaseous Time Projection Chambers (TPC) can also be used as scatter detector. Despite a lower efficiency compared to semi-conductors, they provide a tracking of the recoil electron, in this case also the reconstruction is limited to a small cone section.This is the case for instance for the camera developed by Takada *et al.* (see Fig. 4 (b)).

For the absorber detector, both semi-conductors and scintillators are used. Semi-conductors provide a better energy and position resolution and low noise but scintillators are more robust, cheaper and they provide a better efficiency. If a full absorption of the scattered photons is required, the absorber detector should have a high photo-electric cross section and a high density. Moreover, if time of flight measurements are required, the use of a detector with a good time resolution is necessary.

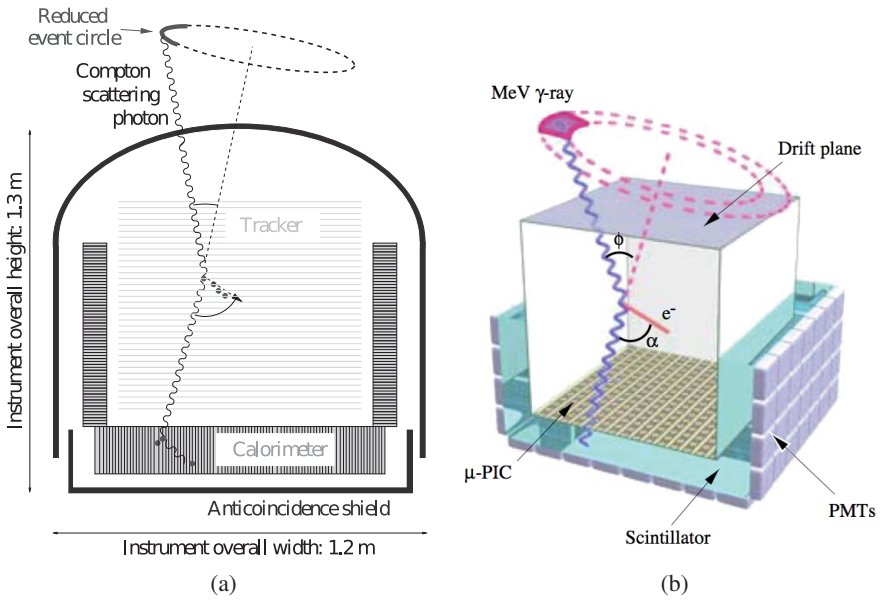

Figure 4: Principle of Compton imaging with: (a) a stack of detectors (adapted from [Andritschke2005])(b) a TPC [Takada2005]. In (b) μ-PIC stands for micro Pixel Chamber, PMTs stands for Photomultipliers Tubes.

A classical Compton camera consists of two parallel plane detectors. Several innovative designs have been proposed to optimise the performances of the camera. First, because the spatial distribution of the scattered photons is not uniform, using non parallel detectors is likely to improve the camera performances. This depends mostly on the photon energy spectrum. Then a multiple scatter Compton camera will offer a higher imaging resolution, at the expense of a lower imaging sensitivity [Seo2008]. They built a proof-of-principle system for such a high-resolution Compton camera, using two double-sided silicon strip detectors (DSSDs) and an NaI(Tl) absorber detector. For a source located at 3.7 cm of the camera, the imaging resolution was 9.0 and 4.8 mm FWHM and the detection efficiency 4.15×10^{-8} and 6.5×10^{-8} for 511 and 1275 keV, respectively. They expect to improve further the imaging resolution by employing more sophisticated detectors and DAQ electronics (see [Seo2010] for more details). Multiple scattering Compton cameras, and in particular double scattering Compton cameras, are useful also if the photon incident energy is unknown [Kroeger2002] (see Chap I.1 § 1.1).

Kang *et al.* proposed to use the TPC Compton camera developed by Takada *et al.*, originally for astronomy applications, to detect prompt γ-ray during ion beam therapy [Kang2009]. Kurosawa *et. al* have recently tested such a prototype with a GSO absorber detector [Kurosawa2012]. A qualitative match of the dose falloff to the reconstructed γ distribution was obtained. It was shown that this correlation is better in the high energy range (800-2000 keV region) than in the low energy range (511 keV peak). The overall efficiency of their current prototype is approximately 3×10^{-6}. A gain of 150 is expected by adopting a higher pressure in the TPC, increasing the number of units around the patients and improving the tracking algorithm.

The cameras investigated within WP3 of the ENVISION project are two Compton cameras with a semiconductor scatter detector and an scintillator absorber detector and one Compton camera with scintillators as scatter and absorber detector. The three prototypes under construction are sketched on Fig. 5. A first prototype with a CZT scatter detector and a LSO absorber detector is being built in Dresden [Fiedler2011]. A detection efficiency of the order of 10^{-4} is expected. They have recently performed tests with a ^{22}Na source. They have reconstructed the source position with a spatial resolution FWHM of 6 mm at a distance of 7 cm [Kormoll2011].

A second prototype consisting of several layers of continuous $LaBr_3$ crystals coupled to silicon photomultiplier (SiPM) arrays is under development in Valencia [Llosa2010]. They measured an energy resolution of 6.5 % FWHM @ 511 keV and a time resolution of 3.1 ns FWHM.

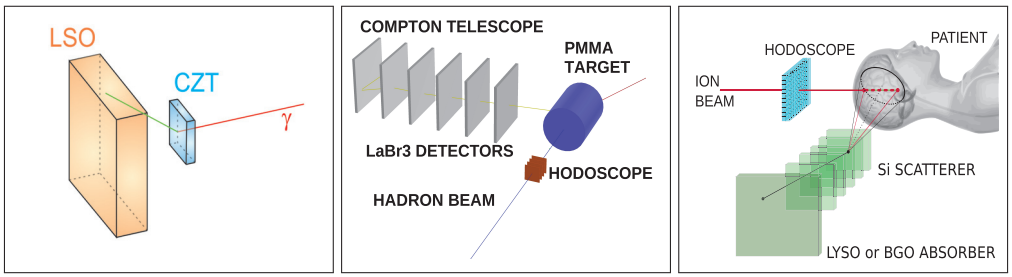

Figure 5: Illustration of the three Compton camera prototypes developed within the ENVISION European project: on the left the German prototype, in the middle the Spanish one and on the right the French one.

The purpose of this document is to present my contributions to the design study carried out in Lyon.

Finally, in Houston, Robertson *et al.* have optimised a three-stage Compton camera. Several material including germanium, BGO, NaI, xenon, silicon and $LaBr_3$ have been evaluated by Monte Carlo simulations [Robertson2011]. A detection efficiency between 9.56×10^{-5} and 1.15×10^{-4} is expected.

2.5 Reconstruction

In imaging, we want to reconstruct the activity distribution $A(x,y,z,E)$, where x, y and z are the coordinates of a point in the 3D space and E the source energy. We perform measurements $M(x,y,z,E)$ with a detection system which can be modeled by the transfer function $S(x,y,z,E)$. The corresponding noise is described by the function $N(x,y,z,E)$. The relationship between activity, measurements and noise is given by:

$$M = S \otimes A + N. \tag{2.7}$$

The goal of image reconstruction is to invert this equation. This problem is common to Compton imaging, PET, SPECT and CT. It can be solved either analytically or iteratively.

In the case of PET, SPECT and CT, analytical reconstruction methods use the Radon inverse transform, offering a direct mathematical solution for the image from known projections. These methods are very fast but they are based on an idealised model of the detection system. A complete data set, point-like perfect detectors, no physical or biological degradation effects and no statistical noise are assumed. This can lead to images with reduced resolution and poor noise properties, often in the form of streaking artifacts.

Iterative methods usually intend to get close to the maximum of the likelihood function, i.e the probability of the observed measurements M given an activity distribution A. They are necessary if the assumptions quoted in the previous paragraph do not hold (which is often the case, except for CT) and if the artifacts in the analytically reconstructed image are too damaging. Also, they can improve image quality compared to analytic image reconstruction through more accurate physical and statistical modeling of photon production and detection processes. Yet, they can be very computationally demanding both in terms of time and memory, and no guarantee exists that the algorithm will converge to the maximum likelihood solution. Moreover, it is difficult to choose the number of iterations establishing a compromise between image resolution and noise, since the theoretical convergence of these algorithms is not achieved in practice. A review of the statistically based iterative methods used currently in emission computed tomography can be found in [Qi2006].

In the case of Compton cameras, the projection and back-projection operations are performed on conical surfaces rather than along straight lines. The acquired data consists of two interaction positions and two energies. Thus the data space can have a dimension of up to eight. As in emission tomography, the reconstruction problem can be solved either with analytical or with iterative methods. Several analytical methods have been proposed [Cree1994], [Basko1998], [Parra2000], [Hirasawa2003] or [Maxim2009]. Note that, the projections acquired are truncated because of the small solid angle covered by the scatter detector at a point of the source and limited because they correspond mostly to small cone aperture angles [Lojacono2011a].

In the case of iterative reconstruction algorithms, because the dimension of the data space can reach eight, the matrix of the system is very large. This increases the memory and computational time requested. Thus the recourse to list mode algorithm is mandatory [Wilderman1998]. Some examples of iterative algorithms developed for Compton cameras can be found in [Schone2010], [Lojacono2011b] or [Zoglauer2011].

In our case, the beam hodoscope greatly simplifies the reconstruction problem. Reconstruction can be done event by event and the reconstruction algorithm can be limited to a simple analytic line-cone intersection. Such an algorithm is very fast, yet it does not include any modeling of the detectors. It made it possible to obtain easily an idea of the performances of our camera, yet in clinical conditions a more elaborated algorithm might be necessary to improve the quality of the reconstructed images. Both iterative and analytical algorithms are currently being developed in Lyon by coworkers in the CREATIS laboratory [Lojacono2011a][Maxim2009].

Part I

Response of the camera to a polyenergetic photon point source

---

This part focuses on the theoretical feasibility of the reconstruction of the position of a photon point source by a Compton camera. I present here the study I led with Frauke Roellinghoff, a MSc student at that time under my supervision, of the response of two different Compton cameras in terms of point spread function and detection efficiency. We first considered a double scattering Compton camera because of the high energy of the prompt γ-rays. Indeed, we thought at first not reasonable to assume that the incident energy of the γ rays could be deduced by adding the energies deposited in the detectors of a Compton camera. The influence of various parameters such as the photon energy and the inter-detector distances was studied. The camera geometry was optimised accordingly. Yet, even in an optimal configuration, the detection efficiency of such a Compton camera remained too low for an application in ion beam therapy.

So, in a second step, we investigated the use of a single scattering Compton camera instead. The major issue was to determine, whether or not, despite the high energy of the prompt γ-rays, the photons incident energies could be deduced by adding the energies deposited in the scatter and in the absorber detector without deteriorating too much the reconstruction result. To increase even more the detection efficiency we replaced the thick scatter detectors by one stack of thin semi-conductor layers with the same overall thickness. Again, we optimised the camera geometry.

In the following chapters, I first present the methods we used to study the response of both Compton cameras to a photon point source followed by the results of these studies. I conclude this part with a discussion of the applicability of Compton cameras in ion beam therapy.

Most of the results presented in this part have been published in [Richard2011], [Roellinghoff2011]. Another article was submitted and is currently under review [Richard2012]. The second appendix of this document if the preprint version of this article.

CHAPTER I.1

Method

1 The detection system

The principle of our detection system, which combines a Compton camera (either a double scattering or a single scattering Compton camera) and a beam hodoscope, is illustrated in Fig. 1 in the case of the double scattering camera. The incident ions are tagged, both spatially and temporally by the beam hodoscope and the prompt γ-rays emitted subsequently to the nuclear fragmentations resulting from the ion interactions in the patient are detected by the Compton camera. The prompt γ-ray emission points are reconstructed by intersecting the ion trajectories, given by the hodoscope and the Compton cones, reconstructed with the camera. Time-of-flight measurements between the hodoscope and the absorber detector of the Compton camera are used to discriminate the prompt γ-rays from the neutrons (also produced during nuclear reactions) which interact in the detector. The detector with lowest counting rate (the absorber detector) is chosen as start signal to minimise the number of void events for which a start signal does not have a corresponding stop signal.

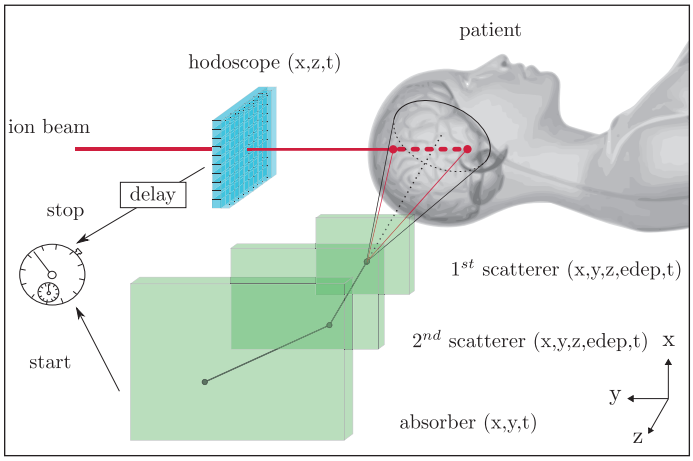

Figure 1: Configuration of the monitoring system: the prompt γ-ray emission points are reconstructed by intersecting the ion trajectory, given by the hodoscope and the Compton cone, reconstructed with the camera. Time-of-flight measurements between the absorber detector and the beam hodoscope (with an appropriate delay) are planned.

1.1 The Compton camera

As explained in the introduction, we first investigated the use of a double scattering Compton camera and then of a single scattering Compton camera. The principle of a single scattering Compton camera was explained in Chap. 2 § 2.1. It is reminded here in Fig. 2. The principle of a double scattering camera is illustrated in Fig. 3. In this case, the incident photons undergo one Compton scattering in each of the first two detectors and then interact in the third detector. The Compton cone is reconstructed in the same way as for a single scattering Compton camera: the cone apex is the interaction position in the first scatter detector, the cone axis is defined by the interaction positions in the first two detectors and the cone aperture half-angle ϑ_1 is deduced from Eq. I.1.4 to Eq. I.1.8: ϑ_1 and ϑ_2 are the photon scattering angles in the first two detectors. E_0, E_1 and E_2 are the photon energies before it reaches respectively, the first scatter detector, the second one and the third one. $\mathbf{r_1}$, $\mathbf{r_2}$ and $\mathbf{r_3}$ are the interaction positions in the three detectors. edep_1 and edep_2 are the energies deposited in the two scatter detectors.

As the photon incident energy E_0 is unknown, in the case of the single scattering Compton camera, a correct reconstruction is possible only if Eq. I.1.3 is verified, i.e. only if the photon deposits all its energy in the absorber detector. In the case of the double scattering camera, this is not required. Note also that in the case of the double scattering camera, the absorber detector measures only the interaction position and not the energy deposited in the detector.

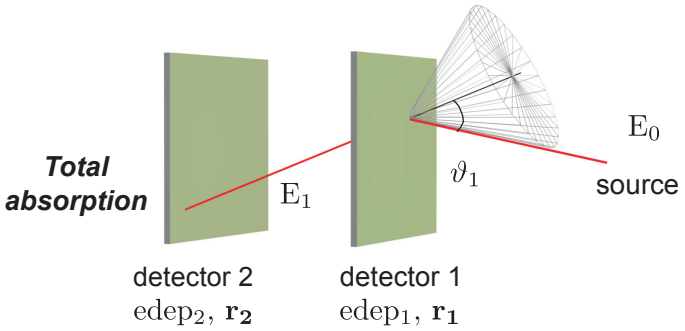

$$\cos(\vartheta_1) = 1 - m_e c^2 \left(\frac{1}{E_1} - \frac{1}{E_0} \right) \qquad \text{(I.1.1)}$$

$$E_0 = \text{edep}_1 + E_1 \qquad \text{(I.1.2)}$$

$$E_1 = \text{edep}_2 \qquad \text{(I.1.3)}$$

Figure 2: Principle of a single scattering Compton camera.

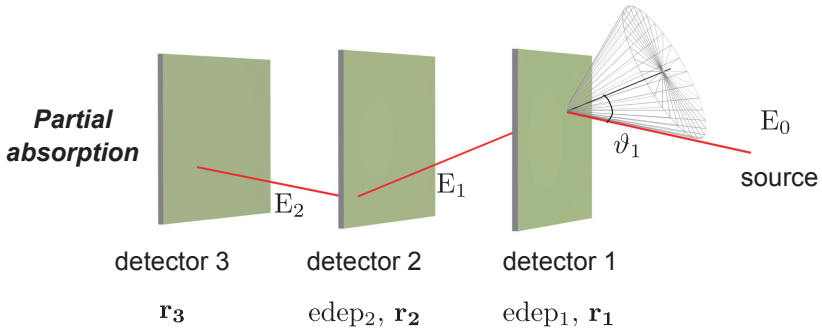

$$\cos(\vartheta_1) = 1 - m_e c^2 \left(\frac{1}{E_1} - \frac{1}{E_0} \right) \qquad \text{(I.1.4)}$$

$$\cos(\vartheta_2) = 1 - m_e c^2 \left(\frac{1}{E_2} - \frac{1}{E_1} \right) \qquad \text{(I.1.5)}$$

$$E_0 = \text{edep}_1 + E_1 \qquad \text{(I.1.6)}$$

$$E_1 = \text{edep}_2 + E_2 \qquad \text{(I.1.7)}$$

$$\cos(\vartheta_2) = \frac{(\mathbf{r_1} - \mathbf{r_2}) \cdot (\mathbf{r_2} - \mathbf{r_3})}{\|\mathbf{r_1} - \mathbf{r_2}\| \cdot \|\mathbf{r_2} - \mathbf{r_3}\|} \qquad \text{(I.1.8)}$$

Figure 3: Principle of a double scattering Compton camera.

When we went from a double to a single scattering Compton camera, the idea was to increase significantly the detection efficiency. Similarly, we decided to replace the thick scatter detector by a stack of thin detectors while keeping the same overall thickness, in order to get about the same solid angle sustended at the source by the scatter detector. This option also allowed to decrease the overall cost of the detectors. Initially, we opted for silicon and LYSO position-sensitive and energy-resolved detectors. Silicon is a semi-conductor that provides a high Compton scattering cross-section and an excellent spatial and energy resolutions. The use of silicon scatter detectors also limits Doppler broadening and its impact on the camera spatial resolution [Zoglauer2003]. A LYSO absorber detector provides a high interaction probability (for the energy range studied here: 100 keV-20 MeV) and a time resolution good enough for time-of-flight measurements. The choice of the absorber material, is discussed in further details in Chap. I.3 § 3.

1.2 The beam hodoscope

The originality of the set-up proposed here relies on the use of a beam hodoscope with the Compton camera. The role of this hodoscope, which is being developed in our lab, is to tag the incident ions both spatially and temporally. The knowledge of the ion beam position, with a resolution in the mm range, greatly simplifies the reconstruction problem. Indeed, it makes it possible to reconstruct each event independently by reducing the reconstruction problem to the intersection between a straight line given by the hodoscope and a cone whereas with a classical Compton camera several cones are needed to reconstruct the source positions [Maxim2009]. This assumes that ion lateral straggling is negligible, that the fragmentations occur along the ion trajectory and that the hodoscope is infinitely precise. Any deviation from these assumptions would translate into a parallax error. As the γ-rays enter the camera at small angles with respect to the transverse plane it seems reasonable not to consider this error.

The time information provided by the hodoscope is necessary to discriminate the interactions in the absorber detector of the prompt γ-rays from the interactions of the secondary neutrons (also produced during irradiation). This requires a time resolution in the ns range, as the fastest neutrons exhibit a velocity close to a third of c and a source-detector distance of several tenths of centimetre.

To be efficient, the hodoscope must provide an individual tag for each ion. In clinical conditions, where particle fluencies can reach up to of 10^8 ^{12}C ions/s and 10^{10} protons/s [Peters2008], this is technically challenging. Such performances could be obtained with synthetic-diamond detectors [RebiszPomorska2010] or scintillating fibers [Achenbach2008]. Both kinds of hodoscopes are currently being developed either in our laboratory or by collaborators from CEA-List Saclay France [Bergonzo2001].

2 The simulations

2.1 Geometry

In this part, the geometry is limited to an isotropic photon point source in air. Fig. 4 illustrates the set-up of the simulations I carried out for the double (left) and single (right) scattering Compton camera. In all simulations, unless otherwise specified, the source was located in the centre of the camera field of view. Table 1 and Table 2 give the default values of the geometry parameters used in the simulations. When the simulation geometry was changed, it is clearly indicated in the corresponding section.

Both Compton cameras are pyramid shaped so that the photons scattered with a large angle (typically up to $\pi/6$) will still impinge on the absorber detector. The values of d_0, d_1, d_2 and n indicated in these tables are the values we adopted after having studied the influence of these parameters on the performances of the camera.

Both monoenergetic and polyenergetic sources were simulated. The spectrum used in the polyenergetic simulations is represented in Fig. 5. The incident energy of each photon was randomly selected in a list of 3×10^5 photon energies. This list corresponds to the prompt γ-ray emission spectrum in 4π steradians obtained when a water phantom is irradiated by 10^5 carbon ions at 310 MeV/u. It was calculated by means of Geant4 version 9.2 simulations. These simulations underlined that this spectrum is largely independent of the carbon ion energy. Moreover, its global shape is consistent with measurements of our collabora-

tion [Lefoulher2010][Envision2012]. Studies by Polf et al. [Polf2009] also showed that the prompt γ-ray spectrum measured during a proton irradiation is similar.

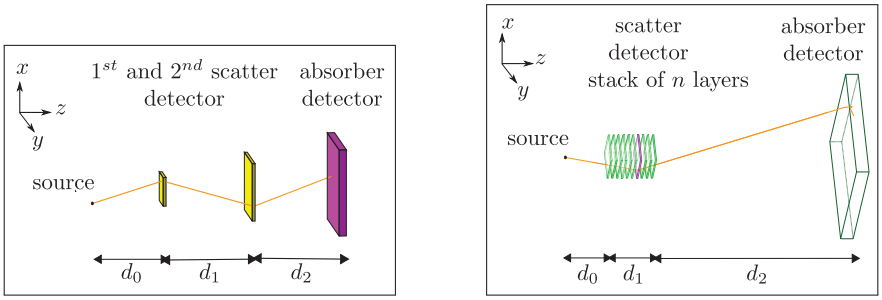

Figure 4: Simulated set-up. On the left, double scattering Compton camera: d_0 is the distance between the source and the centre of the 1st scatter detector, d_1 is the distance between the centres of the 1st and 2nd scatter detector and d_2 is the distance between the centres of the 2nd scatter detector and of the absorber detector. On the right, single scattering Compton camera: d_0 is the distance between the source and the centre of the 1st layer of the scatter detector, d_1 is the distance between the centres of the 1st and last layer of the scatter detector, d_2 is the distance between the centres of the last layer of the scatter detector and of the absorber detector and n is the number of layer in the stack.

Table 1: Default configuration - double scattering Compton camera

	1st scatter detector	2nd scatter detector	absorber detector
material	silicon	silicon	LYSO
$x \times y \times z$, cm^3	10×10 ×1	20×20×1	30×30×2.5

d_0, cm	d_1, cm	d_2, cm
10	30	30

Table 2: Default configuration - single scattering Compton camera

	scatter detector	absorber detector
material	silicon	LYSO
$x \times y \times z$, cm	8×8 ×0.2	30×30×2.5

d_0, cm	d_1, cm	n	d_2, cm
10	9	10	40

2.2 Physics list

All simulations were carried out using Geant4 9.2 and Geant4 9.4. The release number is specified when needed. In this part, only photon and electron interactions into matter were considered. The interactions included in the physics list are listed in Fig. 6. The physics list was restricted to electromagnetic processes and no optical photon process was simulated. The "G4LivermorePolarizedComptonModel" process was used in order to model Compton scattering accurately, i.e. taking into account Doppler broadening and polarisation. These two effects influence the achievable angular resolution in the detectors and the distribution of the azimuthal angle of the photon after the Compton interaction in the second scatter detector [Dogan1992],

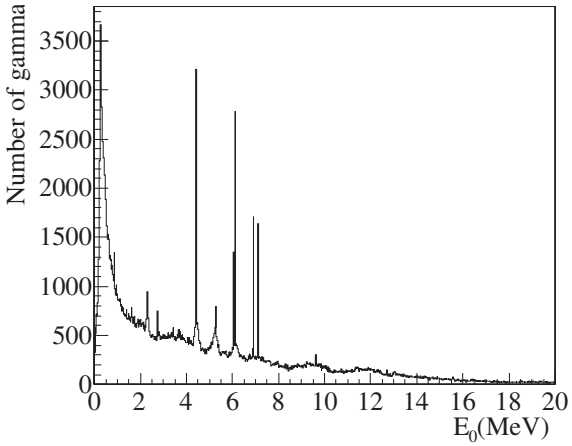

Figure 5: Emission spectrum (Geant4 version 9.2 simulations) in 4π steradians of prompt γ-rays between 0.5 and 20 MeV obtained with 10^5 ^{12}C @ 310 MeV/u in water.

respectively. For the other interaction processes, the standard electromagnetic processes of Geant4 were used. The implementation of these processes has been validated by several studies and good agreement with external reference libraries was found (see for instance [Cirrone2010]). Note that atomic relaxation (Auger electrons and Fluorescence photons) is not considered.

Photon interactions:	e-/e+ interactions:
• photo-electric effect (without atomic relaxation)	• multiple scattering
• Compton effect with Doppler broadening and polarisation (no induced Fluorescence)	• ionisation
• Pair creation	• bremsstrahlung
	• (for e+ only) annihilation

Figure 6: List of the interaction processes included in our simulations.

The production cuts were set to 1 µm for all particles and all materials. These cuts correspond to a threshold below which no secondary particle is generated. They are defined as a distance, or range cut-off, which is internally converted to an energy for individual materials.

2.3 Energy and position recording

In Geant4, one event corresponds to one incident photon. Each event is treated separately, assuming that possible pile-up of interactions corresponding to different events in the same detector is negligible. This might not be the case in a clinical situation. This is discussed in Chap. II.1. For each event, when energy is deposited in one detector, two quantities are calculated: the total energy deposited in the corresponding detector and a global interaction position. As we advanced in our study, we refined the models I use in the simulations. The global position was first defined as the centroid of all the interaction positions in the detectors (method used for all results presented in Chap. I.2). Then it was defined as a deposited-energy weighted barycentre instead (method used for all results presented in Chap. I.3 and in Chap I.4 § 2.3). I observed no significative change in the simulation results.

The energy and position resolutions of the detectors are taken into account by using a Gaussian model. Table 3. summarises the energy and position resolutions used in the simulations. We intend to measure the lateral interaction location with a FWHM resolution of approximately 1 mm in the silicon detectors. No

measurement of the depth of interaction is planned. The energy resolution in the silicon detectors was first assumed to be constant for all energy values. In a second time (for all results presented in Chap. I.3 § 3 and § 4) I used the Fano formula [Struder2000]:

$$\Delta E_{FWHM} = 2.355w\sqrt{N_{\mathrm{ENC}}^2 + \frac{F \times \mathrm{edep}}{w}} \tag{I.1.9}$$

where w=3.65 eV is the pair creation energy in silicon, N_{ENC} the equivalent noise charge (i.e. the rms fluctuation of the read out noise expressed in number of electrons), F=0.115 the Fano factor and edep the energy deposited in silicon.

We intend to obtain an equivalent noise charge of less than 600. We might even reach N_{ENC} = 200 with an appropriate cooling of the detectors. Fig. 7 illustrates the distribution of the energy deposited in the silicon detectors for the reconstructed events (see definition in next §) in the case of the single scattering Compton camera (default configuration). The energy deposited in the silicon detectors of the stack typically lies between 0 and 200 keV. Fig. 8 represents the distribution of ΔE_{FWHM} for various values of N_{ENC} and the influence of N_{ENC} on ΔE_{FWHM} for various values of E. For N_{ENC} between 200 and 600, ΔE_{FWHM} is almost independent of the value of the energy deposited in the detector. So our previous model was not completely inappropriate. A value of 2 keV FWHM was just maybe a too optimistic value. In the simulations, I used N_{ENC}=600, which corresponds to $\Delta E_{FWHM} \approx 5$ keV.

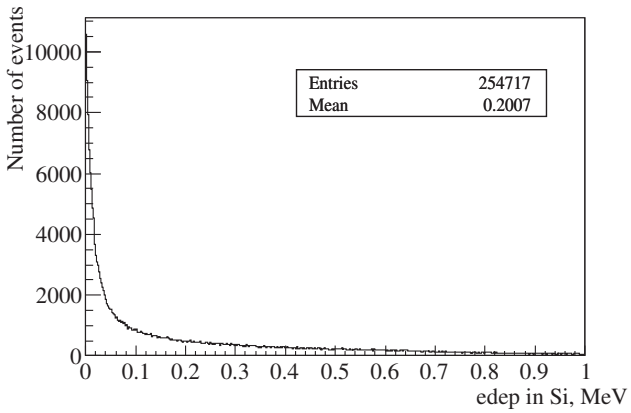

Figure 7: Histogram of the energy deposited in the Si detectors (reconstructed events only)

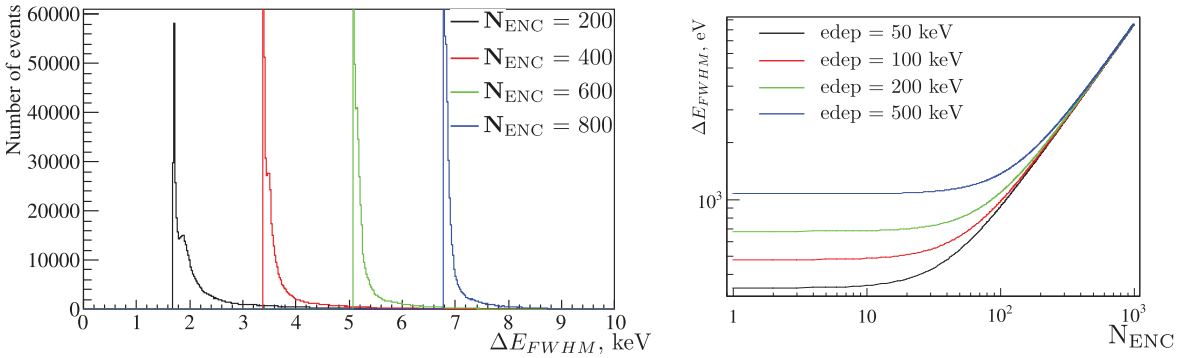

Figure 8: Influence of noise equivalent charge N_{ENC} on the Si energy resolution

The scintillator detector will be read out by photomultiplier tubes and with an Anger logic, the lateral position resolution is expected to be of the order of 5 mm [Zeng2004]. Again no measurement of the depth of interaction is planned, as discussed in Chap. I.3 § 4. According to Kataoka *et al.* [Kataoka2009], the FWHM energy resolution for 1 MeV deposited in a LYSO detector is expected to be as good as 8 % with an energy resolution inversely proportional to the square root of the energy deposited.

Table 3: Detector FWHM resolutions

	Silicon	LYSO
Δ_{XY}, mm	1	5
Δ_E	2 keV $\forall$ edep, or Fano formula	8% @ 1 MeV

2.4 Reconstruction

In the case of the double scattering Compton camera, all the events corresponding to an energy deposit in all three detectors are reconstructed. Eventually, an energy threshold is used, if this is the case, the threshold values are specified in the corresponding paragraphs. The source position should ideally be reconstructed from events (called true events thereafter) corresponding to one Compton scattering in each scatter detector without energy escape (the recoil electrons deposit all their energy in the corresponding scatter detector) and at least one interaction of the scattered photon in the absorber detector. Several other interactions are likely to deposit energy in the three detectors of the Compton camera. For a photon point source, an energy deposit in the first scatter detector may have been produced by:

- the interaction(s) of a primary photon:
  - one Compton interaction without energy escape
  - one Compton interaction with energy escape
  - a pair creation
  - multiple interactions
- the interaction of a secondary particle originating from another detector (a secondary photon, an electron or a positron)
- the interaction of both a primary photon and a secondary particle.

Similarly, in the second scatter detector and in the absorber detector, an energy deposit may have been produced by the interactions of a primary photon, of a photon originating from the Compton interaction of a primary photon or by the interactions of others secondary particles. Fig. 9 illustrates several of these cases. *A priori*, it is not possible to discriminate the true events among all these events but we will see later that the use of upper energy thresholds in both scatter detectors makes it possible to reject most of the bad events (which are systematically wrongly reconstructed).

In the case of the single scattering Compton camera, all the events corresponding to an energy deposit in a single layer of the stack and in the absorber detector are reconstructed. No energy threshold are used. Here, the true events correspond to one Compton interaction in a single layer of silicon without energy escape and at least one interaction of the scattered photon in the absorber detector. Note that this includes events corresponding to a partial absorption in the absorber detector. As for the double scattering Compton camera, energy deposits in both the scatter and the absorber detector may have been produced by other interaction sequences. Mainly it can happen that the Compton electron does not deposit all its energy in one silicon layer or pair creation may occur in silicon. In both cases, secondary charged particles often interact in the neighboring silicon layers and in the absorber detector. For this reason, it is necessary to reconstruct only events in which energy is deposited in one layer of the stack, thus energy thresholds are no longer required.

In all simulations, the coordinates of the source in the transverse plane ((x,z) on Fig. 4) are supposed to be known exactly (the consequences of this hypothesis are discussed in § 1.2). Thus, for each reconstructible events, once all the Compton cone characteristics are determined (apex, axis and aperture angle), the source position is reconstructed by intersecting the Compton cone with the y axis which would stand, in

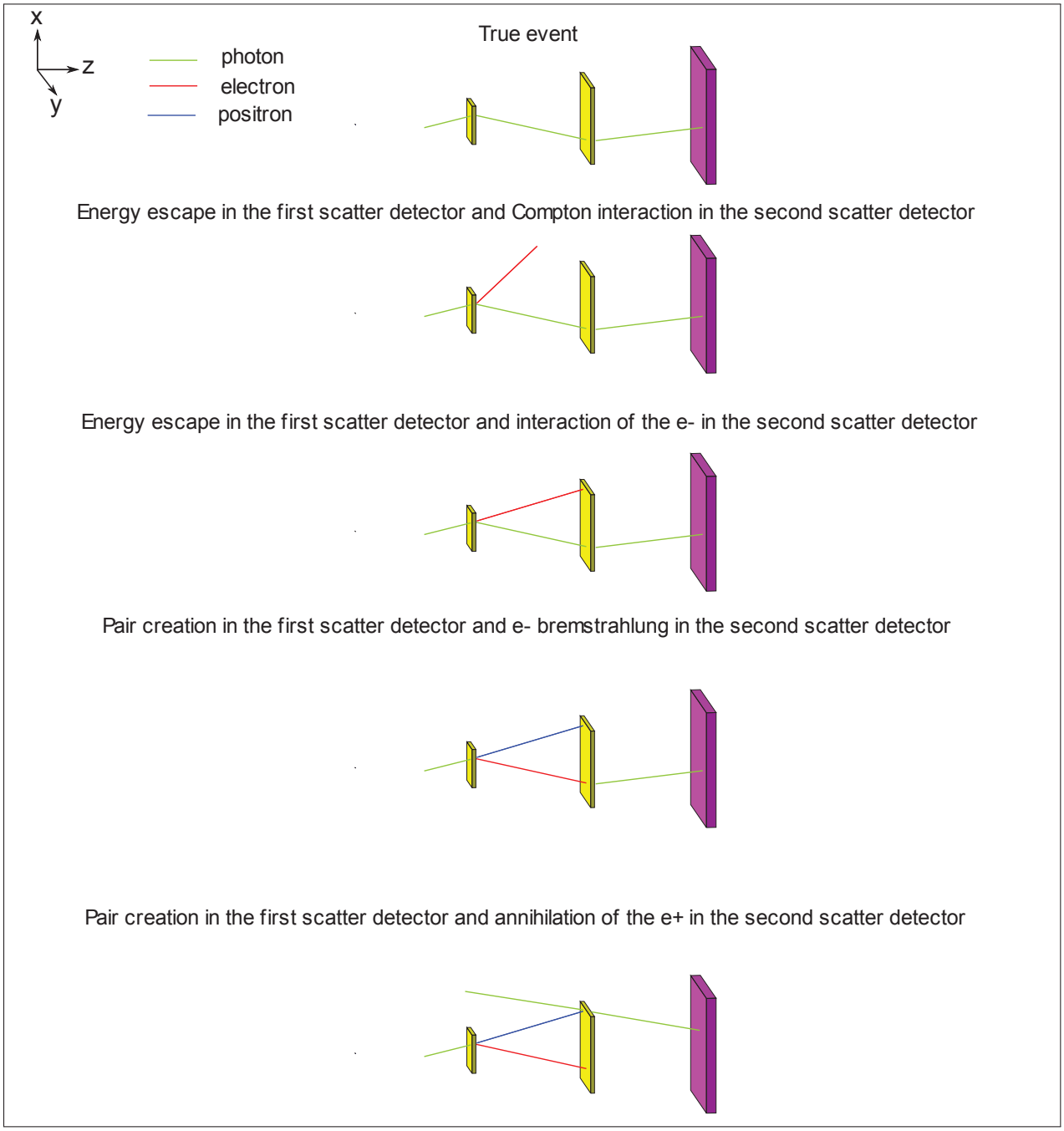

Figure 9: Several interaction sequences corresponding to energy deposit in the three detectors of a double scattering Compton camera.

a realistic set-up, for the beam direction. This intersection problem is likely to have 2, 1 or 0 solution(s). The histogram containing these solutions is the 1D point spread function (PSF) of the camera.

The line-cone intersection problem is solved analytically [Eberly2002]. A point is a solution of this problem if its coordinate vector $\mathbf{r}$ verify the two following equations:

$$\mathbf{r} = \mathbf{r_h} + m \cdot \mathbf{u_h}, \tag{I.1.10}$$

$$\frac{\mathbf{c} \cdot (\mathbf{r} - \mathbf{r_v})}{||(\mathbf{r} - \mathbf{r_v})||} = \cos(\vartheta), \tag{I.1.11}$$

where $m \in \mathbb{R}$ defines the line, $\mathbf{r_h}$ and $\mathbf{u_h}$ are, respectively, a point on the line and its direction vector, $\mathbf{r_v}$ the vertex of the cone, $\mathbf{c}$ its axis direction vector and ϑ its half opening-angle. Note that $||\mathbf{u_h}|| = 1$ and $||\mathbf{c}|| = 1$.

To eliminate the square root calculation, Eq. (I.1.11) has to be squared:

$$(\mathbf{c} \cdot (\mathbf{r} - \mathbf{r_v}))^2 = \cos^2(\vartheta) \cdot ||(\mathbf{r} - \mathbf{r_v})||^2 \tag{I.1.12}$$

And can be brought into the form:

$$(\mathbf{r} - \mathbf{r_v})^T . M . (\mathbf{r} - \mathbf{r_v}) = 0 \qquad \text{with} \qquad M = (\mathbf{c} \cdot \mathbf{c}^T - \cos^2(\vartheta) . I), \tag{I.1.13}$$

where I is the identity matrix.

Combining Eq. (I.1.10) and Eq. (I.1.13) gives

$$a_2 m^2 + 2a_1 m + a_0 = 0 \qquad \text{with} \qquad \begin{aligned} a_2 &= \mathbf{u_h}^T . M . \mathbf{u_h} \\ a_1 &= \mathbf{u_h}^T . M . (\mathbf{r_h} - \mathbf{r_v}) \\ a_0 &= (\mathbf{r_h} - \mathbf{r_v})^T . M . (\mathbf{r_h} - \mathbf{r_v}) \end{aligned} \tag{I.1.14}$$

If $a_2 = a_1 = a_0 = 0$, the line is tangent to the cone.
If $a_2 = 0$, $a_1 = 0$ and $a_0 \neq 0$, there is no solution.
If $a_2 = 0$ and $a_1 \neq 0$, the equation is linear and :

$$m = \frac{-a_0}{a_1} \tag{I.1.15}$$

If $a_2 \neq 0$, the quadratic equation has to be solved. If the discriminant $(a_1^2 - a_2 \cdot a_0) \geq 0$, there are two solutions (otherwise there is no solution) :

$$m_\pm = \frac{-a_1 \pm \sqrt{a_1^2 - a_2 \cdot a_0}}{a_2} \tag{I.1.16}$$

Finally, m can be inserted in equation (I.1.10), giving the intersection position(s). As Eq. I.1.11 was squared, the solutions correspond to the intersections of a double cone with a line. The second cone is the symmetric of the first one with respect to the vertex. Here, this will not be a problem as the first cone will always be directed toward the patient, so there will never be any intersection between the beam axis and the second cone.

In our case, $\mathbf{r_h}$ is simply $(0,0,0)$ and $\mathbf{u_h}$ the direction of the y-axis, i.e. $(0,1,0)$. The location of the vertex of the cone $\mathbf{r_v}$ is the position of interaction in the scatter detector. The cone axis $\mathbf{c}$ is defined by the position of interaction in the first two detectors (the two scatter detectors in the case of the double scattering camera, the scatter and the absorber detector in the case of the single scattering camera):

$$\mathbf{c} = \begin{pmatrix} \frac{(x_1 - x_2)}{\sqrt{(d^2 + (z_1 - z_2)^2)}} \\ \frac{(y_1 - y_2)}{\sqrt{(d^2 + (z_1 - z_2)^2)}} \\ \frac{(z_1 - z_2)}{\sqrt{(d^2 + (z_1 - z_2)^2)}} \end{pmatrix} \qquad \text{with} \qquad d = \sqrt{(x_1 - x_2)^2 + (y_1 - y_2)^2}, \tag{I.1.17}$$

where x_1, y_1, z_1, x_2, y_2, z_2 are the coordinates of the points of interaction in the first two detectors.

2.5 Figures of merit

The spatial resolution of the Compton camera is defined as the full width at half maximum (FWHM) of the PSF. I used two methods to calculate this FWHM: either it was calculated by fitting the histogram with a Lorentzian function or by finding the indices of the first bins with a content lower/higher than half the histogram maximum. The main problem of the first method comes from the choice of the fit limits. As long as the extent of the PSF does not change too much, this method is satisfactory. But, when the shape of the PSF changes too much, the fit limits need to be adjusted very carefully by hand which is not convenient. The second method requires sufficient statistics to be reliable. The method used is specified in the corresponding sections.

The detection efficiency is defined by

$$D_E = \frac{N_r}{N_i}, \tag{I.1.18}$$

where N_r is the number of reconstructed Compton events and N_i the number of photons emitted isotropically in 4π sr. The true efficiency is defined by

$$T_E = \frac{N_{\text{true}}}{N_i}, \tag{I.1.19}$$

where N_{true} is the number of true events, as previously defined.

In the case of the double scattering Compton camera, we decomposed the true efficiency into several components to better understand the influence of the camera geometry on its performances:

- $p_{0\to1}$ is the probability for a photon to reach the first scatter detector,
- p_1 the probability that the photon undergoes a Compton scattering in the first scatter detector without energy escape and that no secondary particle interacts in the detector,
- $p_{1\to2}$ the probability for the photon to reach the second scatter detector,
- p_2 the probability that the photon undergoes one Compton scattering in the second scatter detector without energy escape and that no secondary particle interacts in the detector,
- $p_{2\to3}$ the probability that the photon reaches the absorber detector,
- p_3 the probability that the photon only undergoes at least one interaction in it,
- and p_{th} the probability for a true event not to be rejected because of the energy thresholds.

All the probabilities are conditional probabilities. For instance, $p_{1\to2}$ is the probability for the photon to reach the second scatter detector knowing that it underwent one Compton interaction in the first one. The true efficiency T_E can be expressed as a function of these probabilities:

$$T_E = p_{0\to1} \times p_1 \times p_{1\to2} \times p_2 \times p_{2\to3} \times p_3 \times p_{\text{th}} \tag{I.1.20}$$

The optimisation of the geometry of our Compton camera was carried out focusing on these three characteristics (spatial resolution, detection efficiency and true efficiency).

CHAPTER I.2

Results - Double scattering Compton camera

This chapter presents the optimisation of the double scattering Compton camera presented on Fig. 4 of Chap. I.1. In § 1, the spatial resolution and detection efficiency that can be reached are evaluated, in § 2 the influence of the photon energy and of the inter-detector distances are studied. Finally in § 3 design guidelines are provided. In this chapter, all simulations were performed with Geant4 9.2 and all FWHM calculations were made using a Lorentzian fit.

1 Performances of the double scattering Compton camera

1.1 Energy deposited in the scatter detectors

Fig. 1 represents the energies deposited by the true and the bad events in each scatter detector in the case of the double scattering Compton camera. Most of the true events deposit less than a few hundred keV in each scatter detector. Thanks to the Monte Carlo simulations, the bad events can be sorted out in three main categories:

1. The energy deposit in each detector results only from interactions of the primary photon. Either, one of the recoil electrons does not deposit all its energy in the scatter detector or the photon undergoes more than one Compton interaction in one of the scatter detectors. These events correspond to energy deposits of less than 1 MeV in each scatter detector.

2. A high energy electron (or positron) originating from the first scatter detector (Compton interaction or pair creation) deposits energy in the second one. Such electrons and positrons are minimum ionising particles (MIP). They deposit an amount of energy which depends mostly on the silicon thickness they cross. For a 1 cm detector, they deposit between 3 and 6 MeV. The primary photon may also have deposited energy in the second detector.

3. A bremsstrahlung or an annihilation photon originating from the first scatter detector deposits less than 200 keV in the second detector. For these events the energy deposited in the first detector can reach several MeV.

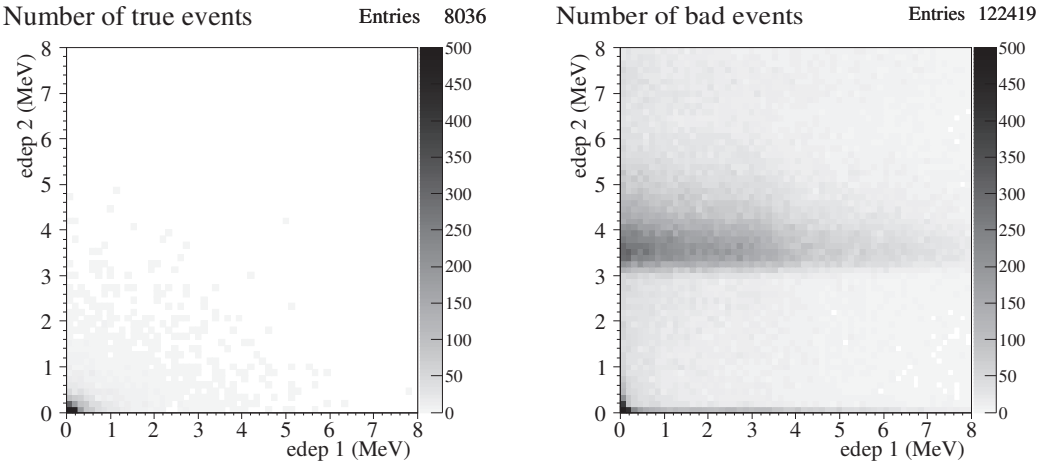

Figure 1: Energies deposited in the first (edep 1) and second (edep 2) scatter detectors by true and bad events for 10^9 polyenergetic photons shot uniformly in the solid angle defined by the geometrical limits of the camera (see Chap. I.1).

In our configuration (detection geometry and energy spectrum), 2 MeV seems to be an adequate upper energy threshold for the two scatter detectors, *i.e.* we reject systematically every event that deposits more than 2 MeV in one of the scatter detectors. This makes it possible to reject 92 % of the bad events while rejecting only 5 % of the true events. The signal-to-noise ratio then improves from 1.1 to 1.8.

1.2 PSF and detection efficiency

Fig. 2 presents the PSF of the Compton camera for a source with a typical prompt γ-ray energy spectrum before (left) and after (right) applying an upper energy threshold of 2 MeV in both scatter detectors. In our configuration, most of the events are bad events from category 2 (events with the interaction in the second detector of a high energy electron or positron originating from the first scatter detector). In Fig. 2 these events are represented by a red dotted line labelled c. In comparison to the true events (represented by a green continuous line labelled b), there are very few other bad events (represented by a blue dotted line labelled d). So, the thresholds must be chosen in order to reject a maximum of the category 2 bad events. That is why we chose 2 MeV thresholds. Fig. 2 confirms that this choice is suitable. Indeed, after applying such thresholds, the true events become dominant and the spatial resolution falls from approximately 20 mm to 6 mm.

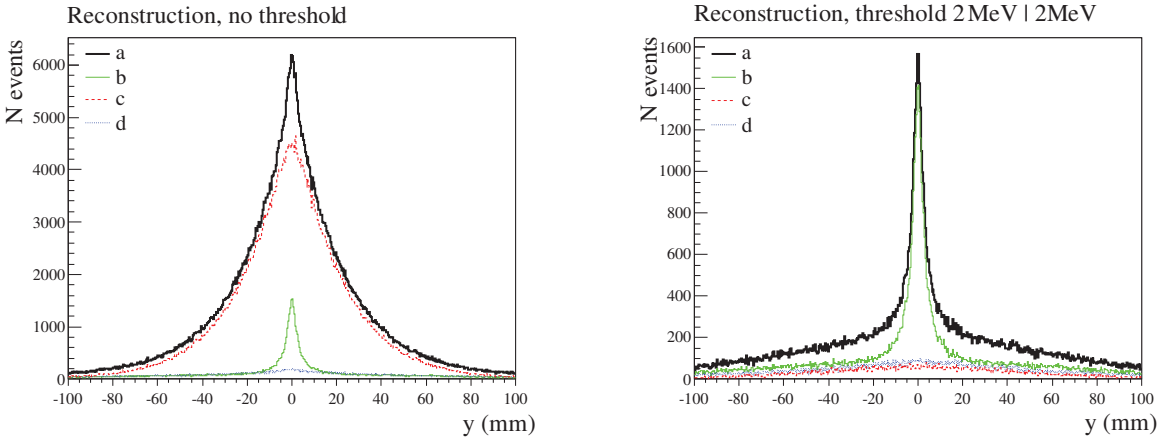

Figure 2: Reconstructed source position with various selections. a: all events, b: true events, c: bad events from category 2, d: other events, mainly events from category 1 and 3.

In our configuration and for a photon point source with a typical prompt γ-ray spectrum, the detection efficiency is 1.5×10^{-5} and the true efficiency 0.70×10^{-5}. The values of the true efficiency components (see chap. I.1 § 2.5 for the definition of each term) are given in Table 1. The true efficiency can be expressed as the products af all components mentioned in this table. $p_{0\to1}$, $p_{1\to2}$ and $p_{2\to3}$, which are the probability for a photon to reach the next detection level, are related to the camera geometry. They can be increased by reducing the inter-detector distances. p_1, p_2 and p_3 are the probability of interaction in each detector. They can be increased by increasing the detector thicknesses or choosing material with higher cross-section of interaction. Yet, the extent to what each of these terms can be increased is limited. First, the camera geometry not only determines the detection efficiency but also the spatial resolution, and very often a configuration favorable to a high detection efficiency corresponds to a poor spatial resolution. Then, we are also limited by the available technology and by cost considerations. In the next §, we fixed the detector dimensions and materials and we studied the influence of the photons incident energy and of the inter-detector distances on these terms and on the camera performances.

Table 1: True efficiency

$p_{0\to1}$	p_1	$p_{1\to2}$	p_2	$p_{2\to3}$	p_3	p_{th}
0.069	0.058	0.11	0.11	0.19	0.75	0.95

2 Influence of the camera geometry on its performances

2.1 Influence of the incident energy of the photons

Fig. 3 and 4 show the variation of the efficiencies and of the camera spatial resolution when increasing E_0 from 0.5 to 20 MeV. From Fig. 3, we can see that overall, the detection efficiency (black squares) decrease when increasing the incident energy of the photons E_0. We also observe a slight rise of the detection efficiency at about 3 MeV. This results from the combination of the variation of the number of true events (green triangles) and the number of bad events (red circles) when increasing E_0 :

- When increasing E_0, the scatter angles are smaller and the photons are more likely to be scattered toward the next detector ($p_{1\to2}$ and $p_{2\to3}$ increase). But the Compton cross section (and more generally the total attenuation cross section) decreases and therefore p_1, p_2 and p_3 decrease. Moreover, at higher energies it is more likely that the recoil electrons escape the scatter detectors and deposit energy in the following detector. So, the true efficiency (green triangles) decreases when increasing E_0.

- Up to about 4 MeV, the contribution of the bad events (red circles) increases. The Compton electrons are MIP (their collision stopping power is about 3.5 MeV per cm). Below 4 MeV, they are sufficiently energetic to escape a scatter detector and generate a 3 hit event. But, most likely, they deposit less than 2 MeV in the scatter detector and these events are not cut by the thresholds. When E_0 increases from 0.5 to 4 MeV, the number of recoil electrons escaping the first scatter detector increases and the number of bad events increases. Above 4 MeV, the recoil electrons energy is high enough so that it both escape the first scatter detector and deposit more than 2 MeV in the second one, the corresponding events are cut by the thresholds.

- Finally for incident energies above 6 MeV, the pair creation cross section becomes comparable and then higher than the Compton one. As a consequence, the number of true events (green triangles) becomes negligible compared to the number of bad events (red circles).

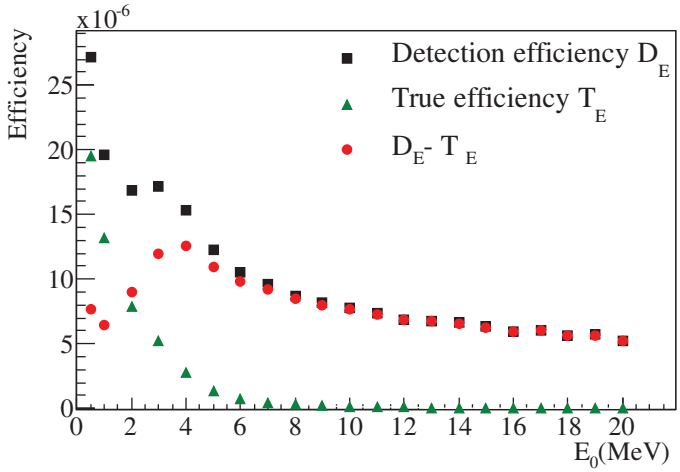

Figure 3: Influence of the photon incident energy on various efficiencies (after applying the energy thresholds).

In Fig. 4 we represented the variation of the spatial resolution with E_0 only between 0.5 and 6 MeV. Over 6 MeV the proportion of true events is negligible, even after applying energy thresholds, and the spatial resolution ε increases dramatically. The spatial resolution decreases between 0.5 and 3 MeV, it reaches a minimum and then it increases between 3 and 6 MeV. This variation is mainly the result of two effects. The relative energy uncertainty due to Doppler broadening is higher at low energies. Thus, the contribution of Doppler broadening to the spatial resolution decreases when increasing E_0. Then, as explained in the

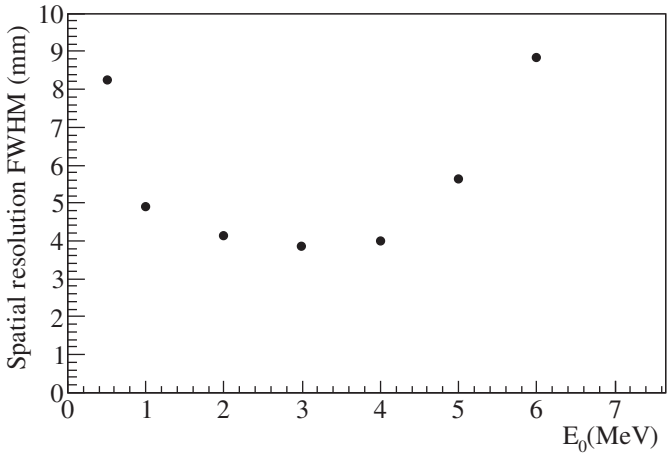

Figure 4: Influence of the photon incident energy on the spatial resolution

previous paragraph, over 3 MeV the proportion of true events drops and the spatial resolution worsens. We will see in next chapter (Chap. I.3 § 1.4) that the increase of the spatial resolution at high energies is also due to the increase of the effect of the detector resolutions.

2.2 Influence of the inter-detector distances

Fig. 5 presents the detection efficiency dependence as a function of the inter-detector distances d_0, d_1 and d_2 for a source with the energy spectrum presented in Chap. I.1. The non-varying distances are d_0 = 10 cm, d_1 = 30 cm and d_2 = 30 cm. We can see that D_E decreases when the inter-detector distances increase from 5 to 50 cm. D_E decreases by a factor of 30 for d_0, a factor of 17 for d_1 and a factor of 9 for d_2. The influence of d_0 is therefore more pronounced.

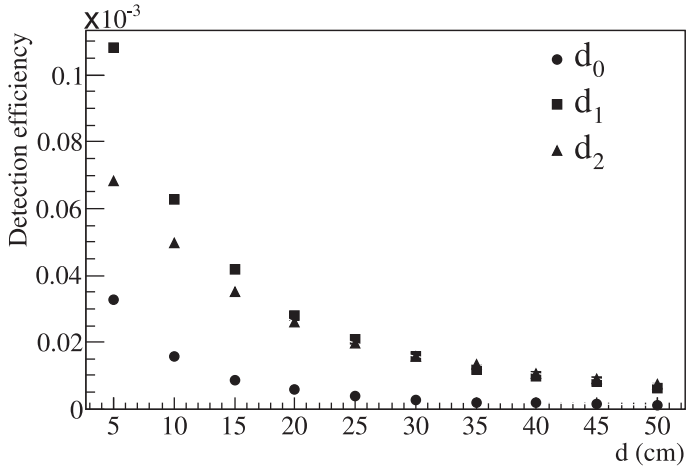

Figure 5: Influence of d_0, d_1 and d_2 on D_E, the non-varying distances are d_0 = 10 cm, d_1 = 30 cm and d_2 = 30 cm.

Fig. 6 presents the influence of d_0, d_1 and d_2 respectively on $p_{0\to1}$, $p_{1\to2}$ and $p_{2\to3}$. When d_0 increases, the predominant effect is the decrease of the solid angle subtended by the first scatter detector at the source, thus the decrease of $p_{0\to1}$. Similarly, when d_1 (resp. d_2) increases, the predominant effect is the decrease of the solid angle subtended by the second scatter detector (resp. by the absorber) at the first (resp. second) scatter detector, thus the decrease of $p_{1\to2}$ (resp. $p_{2\to3}$). The other components of the true efficiency exhibit very limited dependence on d_0, d_1 and d_2 (graphs not shown).

On Fig. 7, we can see the dependence of the resolution ε on d_0, d_1 and d_2. ε increases almost linearly

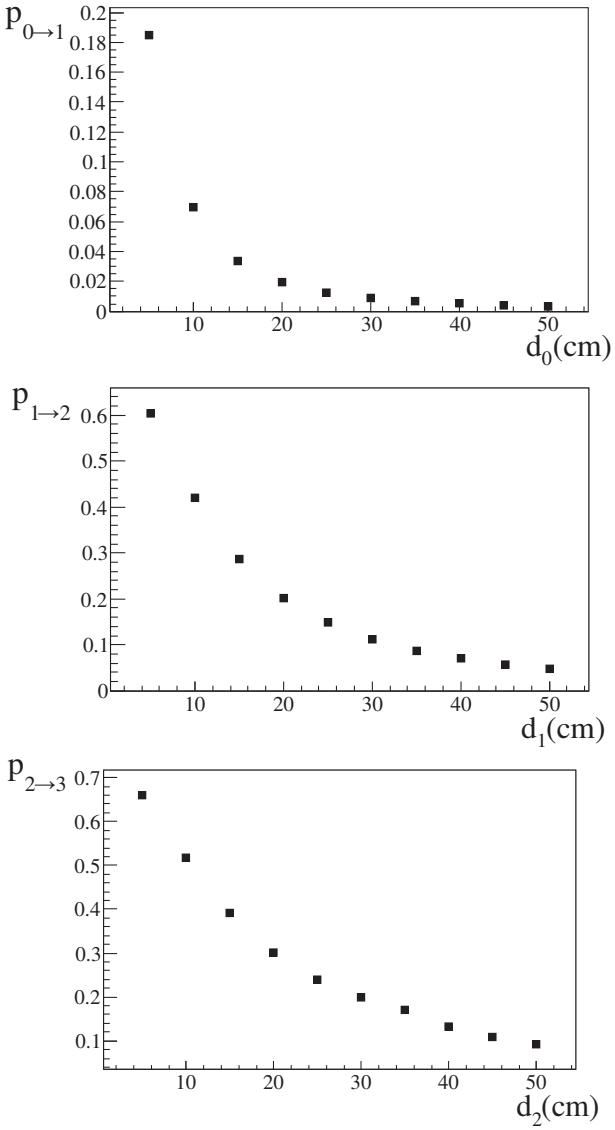

Figure 6: Influence of d_0 on $p_{0\to1}$, d_1 on $p_{1\to2}$ and d_2 on $p_{2\to3}$, the non-varying distances are d_0 = 10 cm, d_1 = 30 cm and d_2 = 30 cm.

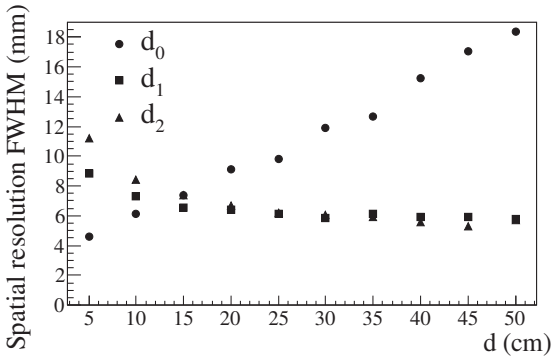

Figure 7: Influence of d_0, d_1 and d_2 on ε, the non-varying distances are d_0 = 10 cm, d_1 = 30 cm and d_2 = 30 cm.

with d_0. Indeed, for a given uncertainty on the reconstructed cone aperture angle, the projection of this uncertainty on the source plane varies linearly with d_0. Finally, it appears that ε decreases when increasing d_1 or d_2 because the uncertainty on the cone axis direction decreases. Again, the influence of d_0 is more pronounced.

3 Design Guidelines

From the previous results several design guidelines emerge for the Compton camera.

- First, it appears that d_0 is a sensitive parameter. Its choice will have a great influence on the efficiency and spatial resolution of the camera. It should be as small as possible in order to maximise the camera efficiency and to minimise its spatial resolution (for a source located at the centre of the camera field of view). Yet, a value of d_0 too small may damage the spatial resolution away from the centre of the camera field of view [1]. The choice of d_0 is also limited by the patient's comfort and by the tumour depth.
- Second, the choice of d_1 and d_2 is driven by a trade-off between a good spatial resolution and a high efficiency. Moreover, the use of time of flight measurements in order to discriminate the prompt γ-ray events from the background requires that $d_0 + d_1 + d_2 > 60$ cm.
- Third, the thicker the detectors, the higher p_1 and p_2 (thus the higher D_E). Increasing the detector thicknesses also leads to less energy escape in the detectors, but to a higher probability of multiple Compton interactions in the scatter detectors.
- Finally, it is important that the area of the second scatter detector is larger than that of the first one and that the absorber detector is larger than the second scatter detector so that the scattered photons do not escape out of the camera and be likely to be detected.

The preliminary set-up of the camera considered in this study was chosen following these guidelines.

[1] The influence of the position of the camera in the field of view on its performances was studied only in the case of the single scattering Compton camera, see next chapter.

CHAPTER I.3

Results - Single scattering Compton camera

This chapter presents the optimisation of the single scattering Compton camera presented on Fig. 4 of Chap. I.1. The goal of this chapter is to determine the performances that can be obtained with a single scattering Compton camera instead of a double scattering Compton camera in order to improve the detection efficiency. The main question concerns the validity of the hypothesis (necessary for the reconstruction): photons deposit all their energy in the absorber detector after one Compton scattering in the scatter detector. This is investigated in § 1 for a camera with a $30 \times 30 \times 2.5$ cm^3 LYSO absorber detector. In § 2, we study the influence of the camera geometry on its performances. In § 3, we focus on the influence of the geometry and material of this absorber detector. Then we chose a more appropriate geometry for the absorber detector (in the case of LYSO, $30 \times 30 \times 4$ cm^3) and we examine in § 4 the influence of its spatial and energy resolutions on the camera performances. Finally in § 5, design guidelines are provided.

Simulations presented in § 1 and § 2 were performed with Geant4 9.2 and the corresponding FWHM calculations were made using a Lorentzian fit. Simulations presented in § 3 and § 4 were performed with Geant4 9.4 and the corresponding FWHM calculations were made using a bin calculation. No significative difference was observed when upgrading Geant4.

1 Performances of the single scattering Compton camera in the case of a $30 \times 30 \times 2.5$ cm^3 LYSO absorber detector

1.1 Reconstructed events

In the case of the single scattering Compton camera, the events that can be correctly reconstructed by our algorithm correspond to one Compton scattering in one silicon detector without energy escape (when the Compton electron deposits all its energy in the silicon detector) and a full absorption of the scattered photon in the LYSO detector. However, other interaction sequences exist which will be reconstructed, albeit incorrectly. They correspond mostly to one interaction of the primary γ in a silicon detector followed by a partial absorption of the scattered photon in the LYSO detector or by interactions of secondary particle(s) such as electrons, positrons or secondary photons in the LYSO detector. In the proposed configuration (see chap. I.1) the true events (one Compton scattering without energy escape and at least one interaction of the scattered photon in the absorber detector) represent 77% of all the reconstructed events (events corresponding to an energy deposit in a single layer of the stack and in the absorber detector). Indeed, using a stack of several thin silicon detectors instead of one thick scatter detector makes it possible to reject most of the events with multiple interactions in the scatter detectors without using any energy threshold.

The simulations showed that 72% of the true events (one Compton scattering without energy escape and at least one interaction of the scattered photon in the absorber detector) correspond to a full absorption of the scattered photon. This means that 55 % of all events are correctly reconstructed. So, it seems reasonable to reconstruct the classical Compton events assuming a total absorption of the photon in the LYSO detector. Contrary to what we thought at first, it is not necessary to limit ourselves to the reconstruction of three-interaction events as done in the case of the double scattering Compton camera.

1.2 PSF and detection efficiency

Fig.1 illustrates the PSF of our Compton camera in the default configuration. Its FWHM is about 8.3 mm. In this configuration, the detection efficiency is 2.5×10^{-4} and the true efficiency 1.9×10^{-4}. In the case of the double scattering Compton camera we had a detection efficiency of 1.5×10^{-5} and a spatial resolution of 6 mm: we have increased the detection efficiency by a factor of 10, the corresponding deterioration of the spatial resolution is limited : only 2.3 mm.

1.3 Reconstruction of the events with Compton electron escape

Fig. 2 of Chap. I.2 compares the PSF for all reconstructed events and the PSF for the true events in the case of the double scattering Compton camera. On the left graph we can see that the bad events are far more numerous than the true events: approximately 20 times more numerous. Managing to reconstruct these

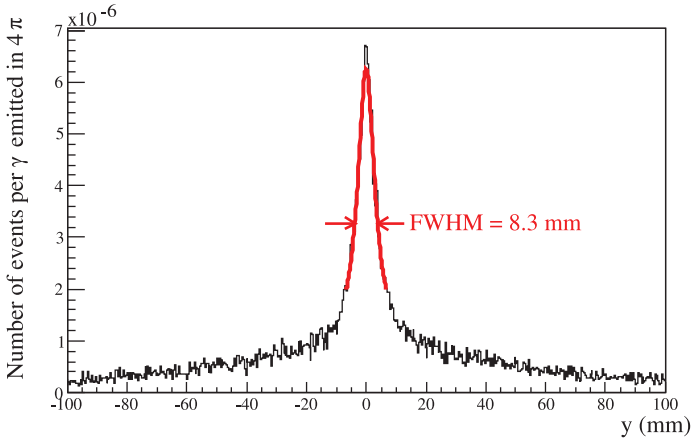

Figure 1: Reconstructed source position for a source at the centre of the camera field of view

events would makes it possible to improve significantly the detection efficiency. These events are mostly events with the interaction in the second scatter detector of a high energy electron originating from the first scatter detector.

In the case of a single scattering Compton camera with a stack of detectors as scatter detector, these events generate a specific pattern of interactions: energy deposit in several successive layers of the stack and eventually an interaction of the scattered photon in the absorber detector. So in the simulations, I selected the events with energy deposit in several consecutive silicon detectors and energy deposit in the LYSO detector. I reconstructed these events assuming the Compton interaction took place in the first silicon detector with energy deposit and that the energy of the Compton electron is the sum of energy deposited in all the silicon detectors. I also assume that the energy deposited in the LYSO detector correspond to the interaction of the Compton scattered photon.

If these events only are reconstructed, the detection efficiency of the camera is 1.8×10^{-4} (currently the detection efficiency of the single scattering Compton camera is 2.5×10^{-4}) and the spatial resolution 48 mm. So the potential gain in detection efficiency is limited to less than a factor of 2, for a corresponding major degradation of the spatial resolution. Indeed, in the case of the double scattering Compton camera, the ratio between the number of events with interactions of secondary electrons in the second Si detector and in the LYSO detector and the number of true events was much higher. But, this ratio includes two factors: the probability that the Compton electrons escape and the probability that the primary photon undergoes a second Compton scattering in the second Si detector.

$$\frac{n_{\text{events with inte. of 2nd e-}}}{n_{\text{true events}}} \approx \frac{p_1 \times p_{\text{escape}} \times p_3}{p_1 \times p_2 \times p_3} = \frac{p_{\text{escape}}}{p_2}. \tag{I.3.1}$$

In the case of the Compton camera with a stack, the ratio between the number of events with several interactions in the stack and the number of 2 hit events only comprises the probability that the Compton electrons escape. This explains the gain of only a factor 2.

Moreover, among the selected events, the events with a correct interaction pattern correspond only to $\approx$ 17 % of all of these events. First it is very likely that the scattered photons do not interact in the LYSO detector, either they interact in one of the Si detectors ($\approx$ 4 % of the events) or they escape the camera ($\approx$ 35 % of the events). Among the selected events there is also a significant amount of pair creation events ($\approx$ 35 % of the events). This explains the bad spatial resolution. For the events with a correct interaction pattern, the spatial resolution is 10.5 mm.

Even if it was possible to select only the events with a correct interaction pattern, we will only add a detection efficiency of $17\% \times 1.8 \times 10^{-4} = 3 \times 10^{-5}$ to the current detection efficiency of 2.5×10^{-4}. As a consequence we decided not to reconstruct these events.

1.4 Influence of the photon incident energy

Fig. 2 shows the evolution of the spatial resolution of the Compton camera when increasing the photon incident energy E_0 from 100 keV to 6 MeV. The spatial resolution decreases between 100 keV and 3 MeV, it reaches a minimum and then it increases between 3 and 6 MeV. Over 6 MeV (not represented on the graphs), the spatial resolution increases dramatically. The spatial resolution of the Compton camera is limited by Doppler broadening and by the detector energy and position resolutions. The influence of these contributions depends on E_0. To study this effect, the detector energy and position resolutions were alternately turned on and off in the simulations. Fig. 2 (bottom graphs) illustrates the evolution of the spatial resolution of the Compton camera for different detector set-up (perfect detectors, detectors with a perfect position resolution and detectors with a perfect energy resolution). In the case of perfect detectors, the only source of error is Doppler broadening. We observe that at low energies, the contribution of the detector energy resolution dominates. At high energies, the contribution of Doppler broadening is negligible.

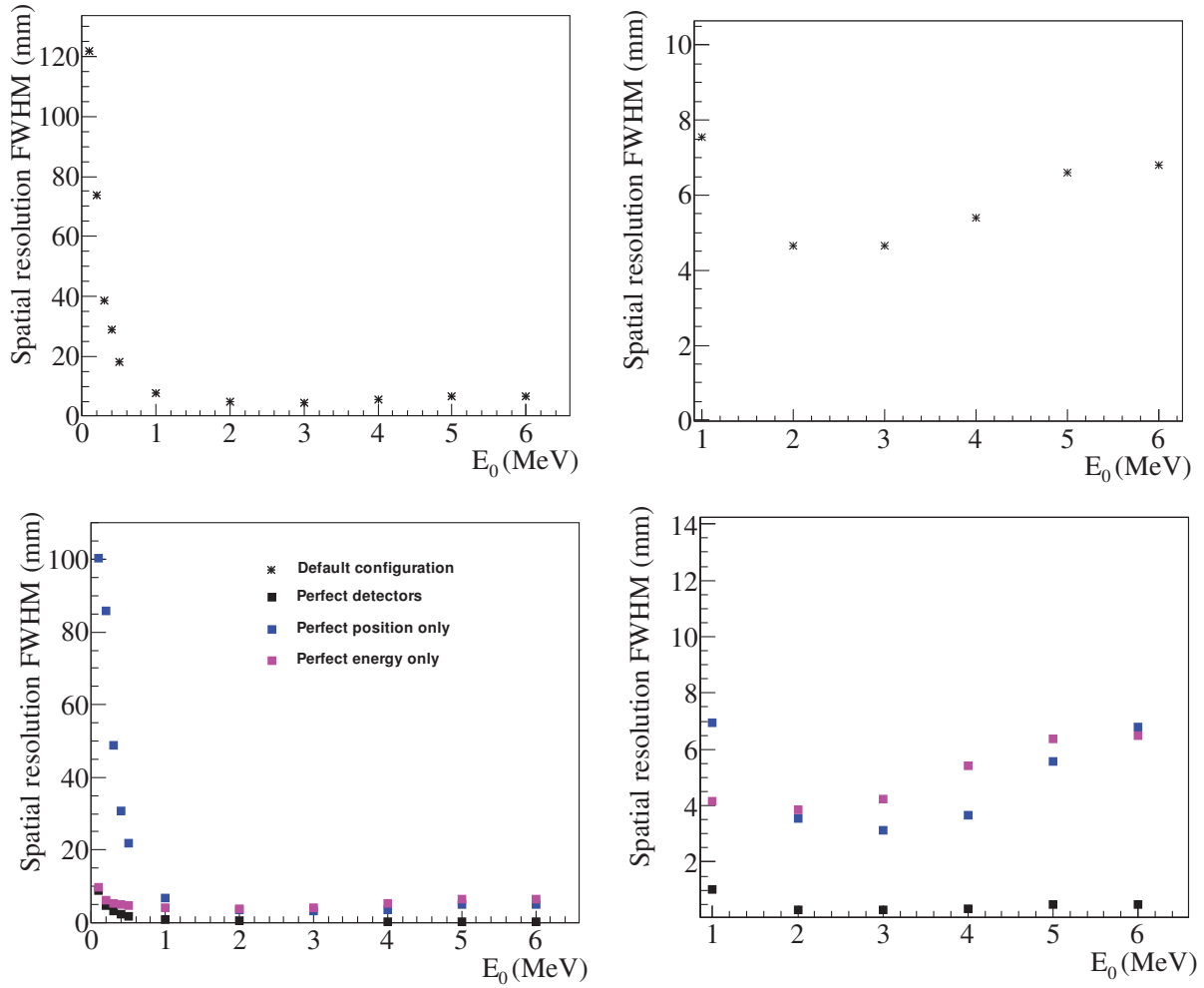

Figure 2: Influence of the photon incident energy on the spatial resolution, on the left from 100 keV to 6MeV, on the right from 1 to 6 MeV. On the top, the spatial resolution was calculated in the default configuration, on the bottom it was calculated for perfect detectors, for detectors with a perfect position resolution and for detectors with a perfect energy resolution.

The evolution of the spatial resolution with E_0 is very similar in the case of the double scattering Compton camera (see Chap. I.2 § 2.1). In the case of the double scattering Compton camera, we associated the increase of the spatial resolution at high energies with the decrease of the percentage of true events: 65 % at 1 MeV and 1 % at 6 MeV. Here, the percentage of true events decreases only from 95 % at 1 MeV to 45 % at 6 MeV. And for perfect detectors, the spatial resolution of the camera does not increase above 2 MeV. On the

other hand, we observe that the contribution of the detector resolutions increases at high energy. So, here, the decrease of the percentage of true events is not responsible for the degradation of the spatial resolution at high energy, the increase of the contribution of the detector resolution is. In the case of the double scattering Compton camera, as the percentage of true events is significantly lower, the effect of the decrease of the percentage of true events is more important, the increase of the detector resolution contribution is certainly present also, but it was not detected during our study of this camera.

2 Influence of the camera geometry on its performances in the case of a $30 \times 30 \times 2.5$ cm^3 LYSO absorber detector

2.1 Influence of the number of layers in the stack

The number n of detectors in the stack was varied without changing d_1: when increasing the number of detectors, the distance between two detectors was reduced so that the distance between the first and the last layer of the stack was kept to 9 cm. We tested configurations with 2 to 34 layers in the stack.

Fig. 3 shows the variations of the spatial resolution and of D_E when increasing n. Both improve when we add more detectors in the stack. The decrease of the spatial resolution can be explained by an increased probability for the events with energy escape or pair creation in the silicon detector to generate a hit in more than one layer in the stack and thus to be rejected. When increasing n from 2 to 34 the proportion of true events among the reconstructed events increases from 45% to 88% (77% for n=10). Above about 20 detectors, the improvement of the camera performances is less pronounced. So using more than 20 layers of silicon in the stack seems costly and useless. To begin with, and for economical reasons, we decided to use 10 silicon layers.

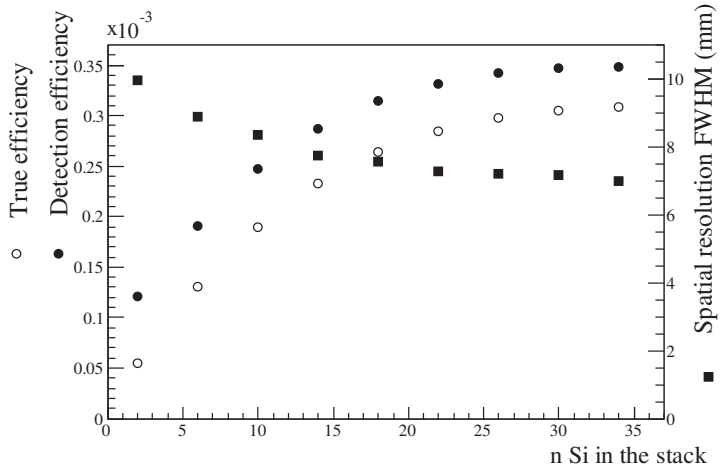

Figure 3: Influence of n on D_E and on the spatial resolution

2.2 Influence of the stack to absorber distance

Fig. 4 shows the variations of the spatial resolution and of the detection efficiency when increasing d_2 from 5 to 50 cm. As explained before, when increasing d_2 the detection efficiency decreases because the solid angle sustained by the absorber detector at each layer of the stack decreases. The spatial resolution improves because the distance between the two interactions of the primary photons increases. d_2 = 40 cm seems a good trade-off. It leads to a total camera length of 50 cm and a source-absorber distance of 60 cm which is enough to discriminate neutrons and photons with a TOF resolution of 1 ns.

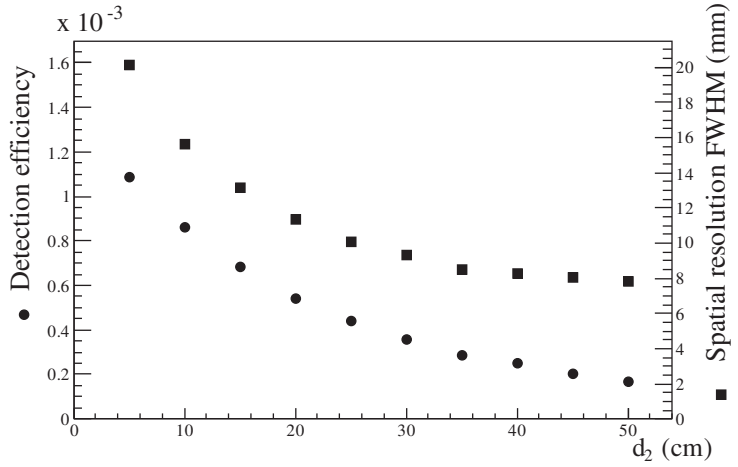

Figure 4: Influence of d_2 on D_E and on the spatial resolution

2.3 Influence of the position of the source in the field of view

Fig. 5 shows the variations of the spatial resolution and of the detection efficiency when the source is moved away from the centre of the field of view. As expected, as soon as the source is located out of the scatter detector limits, the spatial resolution and the detection efficiency are dramatically degraded. For d_0=10 cm, between the centre of the field of view and the scatter detector limit, the detection effiency decreases from 2.5×10^{-4} to 1.9×10^{-4} and the spatial resolution increases from 8.3 mm to 9 mm.

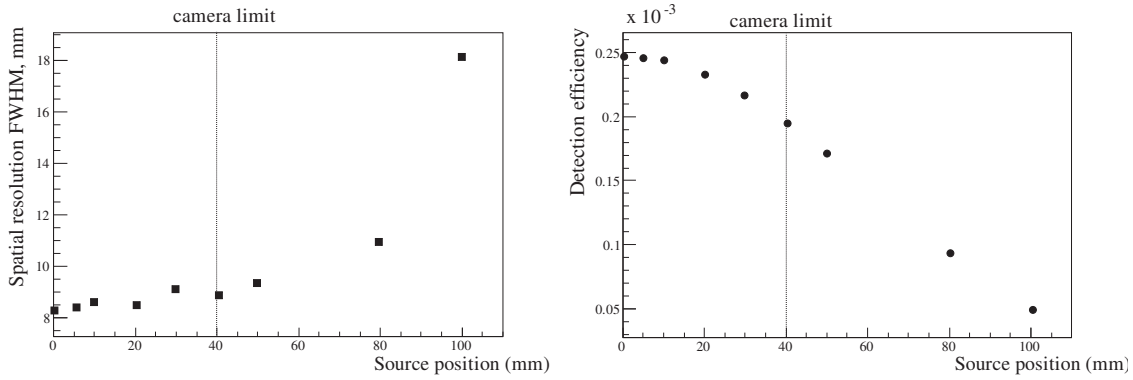

Figure 5: Influence of the position of the source in the field of view of the camera on D_E and on the spatial resolution

3 Design study of the absorber detector

3.1 Energy deposited in the absorber detector

In this section we consider a 4 cm thick LYSO detector as absorber detector. Fig. 6 represents, for all the reconstructed events, the distribution of (i) the energy of the photons incident on the scatter detector, (ii) the energy of the photons impinging on the absorber detector and (iii) the energy deposited in the absorber detector. The mean energy deposited in a 4 cm thick LYSO absorber is 1.7 MeV. As expected, above a few MeV, the number of photons which deposit all their energy in the absorber detector drops, and the spectra "energy of photons impinging on LYSO" and "energy deposited in LYSO" diverge.

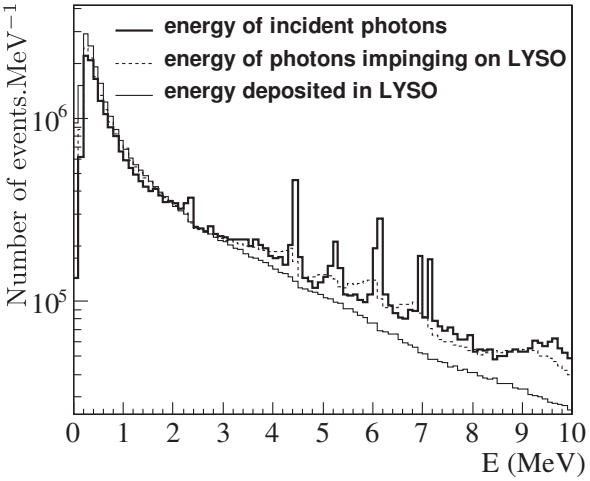

Figure 6: Energy spectra for all reconstructed events in the case of a 4 cm thick LYSO absorber detector for 5×10^8 incident photons in 4π sr.

3.2 Absorber thickness & width

Fig. 7 shows the influence of the absorber detector thickness t_D on the spatial resolution of the camera and on the detection efficiency for 30 cm wide LYSO, $LaBr_3$, BGO and NaI absorber detectors. As t_D is increased from 1.5 to 7.5 cm, the detection efficiency grows, as one would expect from the exponential attenuation law. The maximum gain in the detection efficiency is of a factor of 2. Concerning the spatial resolution of the camera, there is an optimal thickness. Indeed, when increasing t_D, we increase the number of photons fully absorbed ($N_{t.a.}$) which improves the resolution. However increasing t_D also increases the parallax error due to the fact that we have no information on the interaction depth. For a 30 cm wide detector the optimal thickness is around 4 cm for LYSO, 5 cm for $LaBr_3$, 4.5 cm for BGO and 6 cm for NaI.

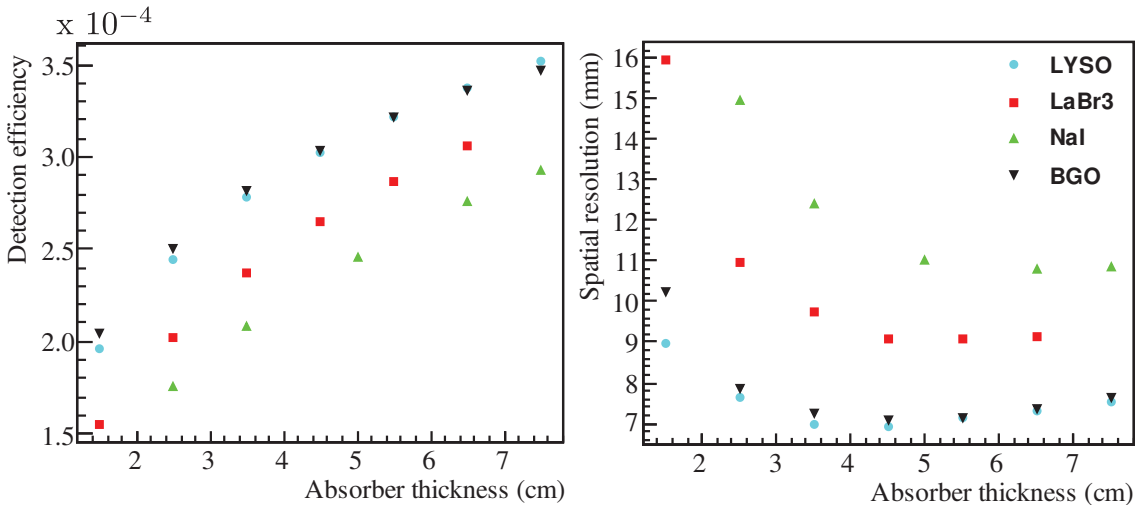

Figure 7: Influence of the absorber detector thickness on the detection efficiency and on the spatial resolution of the camera. As the absorber thickness increases, the detection efficiency increases; the spatial resolution first improves and then deteriorates.

Fig. 8 shows the influence of the absorber detector width w_D on the spatial resolution of the camera and on the detection efficiency for a 4 cm thick LYSO, a 5 cm thick $LaBr_3$, a 4.5 cm thick BGO and a 6 cm thick NaI absorber detector. Naturally, the detection efficiency increases with the detector width. The influence of the detector width on the detection efficiency is more pronounced than the influence of its thickness.

Between 10 and 30 cm, w_D does not influence the spatial resolution of the camera. For absorber detector

widths greater than 30 cm, the spatial resolution of the camera deteriorates. Indeed, we reconstruct Compton events for which the low energy (associated to a large ϑ angle) Compton photons impinge on a detector edge and the angular error for these events is higher due to a higher parallax error (as the depth of interaction is not measured in the absorber detector).

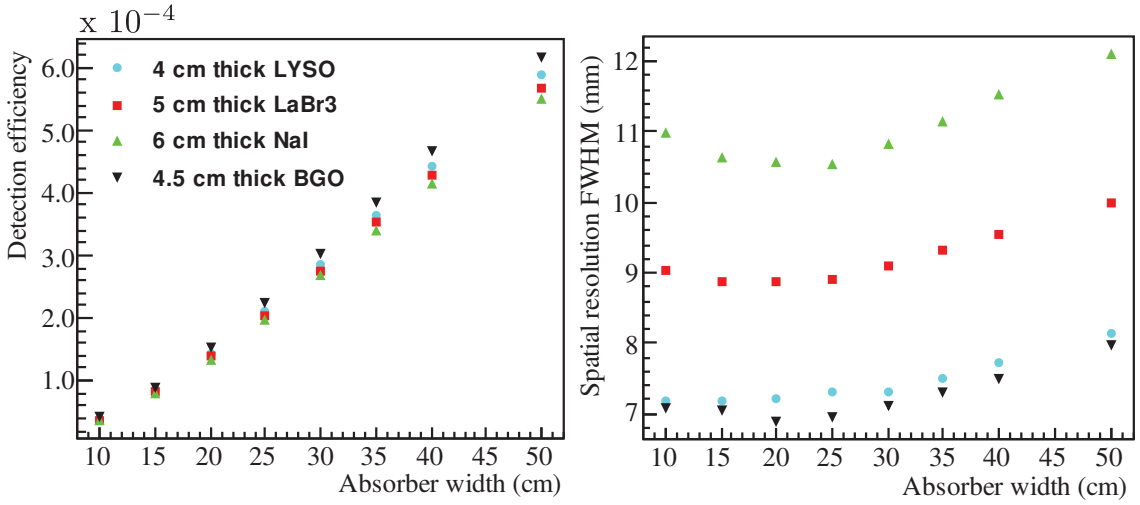

Figure 8: Influence of the absorber detector width on the detection efficiency and on the spatial resolution of the camera. As the absorber width increases, the detection efficiency increases. For absorber detector widths below 30 cm the spatial resolution is almost constant.

3.3 Absorber material

Table 1: Expected features of four scintillators

Material	LYSO	$LaBr_3$	BGO	NaI
Dimensions, cm ($30 \times 30 \times \cdots$)	4	5	4.5	6
Density	6.50	5.08	7.13	3.67
$\Delta E/E$ FWHM@ 1 MeV (%)	8	4.1	14	6.0
Intrinsic radioactivity (Bq/cm^3)	277	0.4	0	0
Efficiency ($\times 10^{-4}$)	3	2.8	3	2.7
$P_{t.a.}$, %	76	64	81	64
FWHM, mm	7.3	9	7	11

In Table 1 we compare the performances of LYSO, $LaBr_3$, BGO and NaI in a case corresponding to the optimal thickness for each material. This leads to very close values of the detection efficiency. The comparison of LYSO, $LaBr_3$ and BGO brings out the fact that the percentage of total absorption is the main parameter to optimise the spatial resolution of the camera. BGO is the material with the highest Z here. Thus the percentage of total absorption in BGO, which depends directly on the photo-electric cross-section, is higher than in the other materials. This explains why, despite a significantly lower energy resolution, the FWHM of a camera with a BGO absorber detector is the same as the FWHM of a camera with a LYSO absorber detector and better than the FWHM for $LaBr_3$ and NaI.

When several interactions occur in the absorber detector, the Compton cone should be ideally reconstructed from the position of the first interaction. Actually, it is reconstructed from an energy-weighted barycentre. If the photo-electric cross-section is higher, the fraction of photons undergoing only one photo-electric interaction in the absorber detector increases, i.e. the number of photons for which the barycentre position matches the position of the first interaction increases and the spatial resolution of the camera improves. For a 4 cm thick LYSO detector and a 4.5 cm thick BGO detector, the mean distance between the first interaction and the barycentre is 3.4 mm. It is 4.9 mm for a 5 cm thick $LaBr_3$ detector and 5.5 mm for a 6 cm thick NaI detector.

The spatial resolution of the camera is also determined to a lesser extent by the energy resolution of the scintillator (see $LaBr_3$ *vs* NaI).

4 Influence of the detector resolutions on the spatial resolution in the case of a $30 \times 30 \times 4$ cm^3 LYSO absorber detector

4.1 Comparison of the different contributions

We have seen (see § 1.4) that the effect of Doppler broadening and of the detector resolutions depends on the photon incident energy. Here we are comparing these contributions in the case of a typical prompt γ-ray spectrum (see Chap. I.1). As in § 1.4, simulations were performed in the case of realistic and/or perfect detectors, with and/or without Doppler broadening. Note that a perfect detector would measure the position of the first interaction. Hence, in the corresponding simulations the barycentre calculation was disabled. The resolutions used for the realistic detectors are precised in Chap. I.1 § 2.3. In a realistic configuration, the spatial resolution of our Compton camera is 7.3 mm.

Table 2 gives the spatial resolution in configurations for which only one degrading effect (i.e. Doppler broadening or one of the detector resolutions) was taken into account in the simulations. For instance, 0.6 mm is the spatial resolution of the Compton camera when only Doppler broadening is taken into account and when the energy and spatial resolutions are assumed perfect in the simulations.

Table 3 gives the spatial resolution in configurations for which all but one degrading effect were taken into account in the simulations. For instance, 6.5 mm is the spatial resolution of the Compton camera when only the detector energy and position resolutions are taken into account, and not Doppler broadening.

Table 2: Spatial resolution with only one degrading effect taken into account

contribution / configuration	Doppler	E_{Si}	$Position_{Si}$	E_{LYSO}	$Position_{LYSO}$
FWHM spatial resolution, mm	0.6	0.40	2.0	0.30	3.2

Table 3: Spatial resolution with all but one degrading effect taken into account

contribution / configuration	Doppler	E_{Si}	$Position_{Si}$	E_{LYSO}	$Position_{LYSO}$
FWHM spatial resolution, mm	6.5	6.8	6.4	6.5	4.7

The most important contribution to the spatial resolution of the camera is the position resolution of the absorber detector. With a perfect measurement of the interaction position in the LYSO detector, the spatial resolution of the Compton camera would drop by more than 2 mm. Then, the major room for improvement of the camera resolution comes from the position resolution in the LYSO detector and the position resolution in the silicon detectors. We also observe that the effect of Doppler broadening is not dramatic and comparable to the effect of the detector energy resolutions.

The square root of the quadratic sum of all contributions is 3.6 mm $\ll$ 7.3 mm. This suggests that the effects of the different contributions are correlated. This explains also why, for instance, the effects of Doppler broadening, of E_{Si} and of E_{LYSO} alone are the same, but when only one of these contributions is not taken into account, the corresponding drop in the spatial resolution of the camera is not the same.

4.2 Influence of the resolution values

Although the depth of interaction measurement in the detectors is not likely to be implemented in the prototype as it was assumed in above simulations, we propose here to study the influence of the energy and spatial resolutions of both the silicon detectors and the LYSO detector on the spatial resolution of the camera.

Fig. 9 shows the variability of the spatial resolution of the camera as a function of each resolution of the silicon detectors. We observe that the spatial resolution of the camera is not influenced significantly neither the depth resolution nor by the value of the equivalent noise charge (in the ranges considered here). The influence of the lateral resolution is more pronounced: when deteriorating $\Delta_{XY,Si}$, the FWHM lateral spatial resolution of the silicon detectors, by 1 mm, the resolution worsens by approximately 0.75 mm. This is explained easily by the fact that the apex of the reconstructed cone is directly the position interaction in the scatter detector.

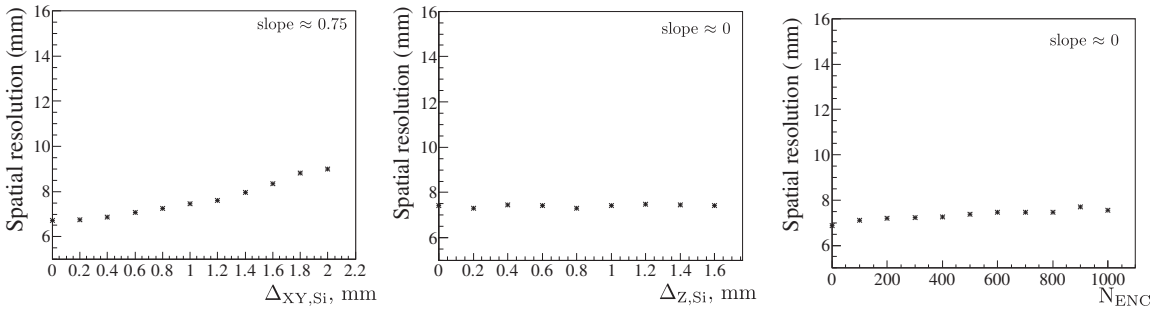

Figure 9: Influence of the scatter detector resolutions on the spatial resolution of the camera. $\Delta_{XY,Si}$, $\Delta_{Z,Si}$, and N_{ENC} are the FWHM lateral spatial resolution, in-depth spatial resolution, and the equivalent noise charge of the silicon detectors, respectively.

Fig. 10 shows the variability of the spatial resolution of the camera as a function of each resolution of the absorber detector. The most important point is that the spatial resolution of the camera is not influenced significantly by the depth resolution. This justifies our previous choice not to measure the depth of interaction in the absorber detector. The influence of the energy and lateral resolution are more pronounced: when deteriorating $\Delta_{XY,LYSO}$, the FWHM lateral spatial resolution of the LYSO detector, by 1 mm, the resolution worsens by approximately 0.4 mm. When deteriorating $\Delta_{E,LYSO}$, the FWHM energy resolution of the LYSO detector at 1 MeV, by 1% the spatial resolution worsens by approximately 0.13 mm.

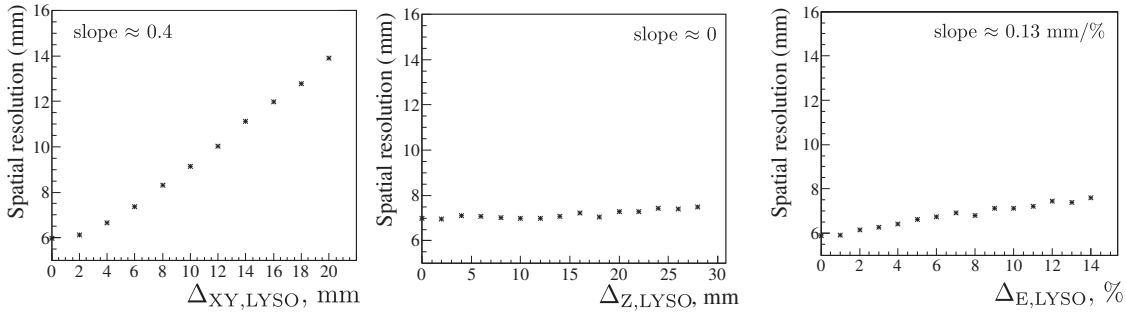

Figure 10: Influence of the absorber detector resolutions on the spatial resolution of the camera. $\Delta_{XY,LYSO}$, $\Delta_{Z,LYSO}$, and $\Delta_{E,LYSO}$ are the FWHM lateral spatial resolution, in-depth spatial resolution, and energy resolution of the LYSO detector, respectively.

5 Design Guidelines

From the results presented in this chapter, several new guidelines emerge:

- For an application in ion beam therapy, a double scattering camera is not necessary. Using a single scattering Compton camera assuming the scattered photons deposit all their energy in the absorber detector gives a correct spatial resolution: 7.3 mm instead of 6 mm. Moreover, by using a single scattering Compton camera instead of a double scattering one and by optimising the absorber detector, we increased the detection efficiency from 1.5×10^{-5} to 3×10^{-4}.
- Using a stack as scatter detector makes it possible to select mainly events which are likely to be correctly reconstructed (i.e. events corresponding actually to a Compton scattering in the scatter detector). In this new configuration, no energy thresholds are required. To improve the camera efficiency and resolution as many layers as possible should be used knowing that after 20 layers no important improvement is observed.
- For an application in ion beam therapy, and with the current performances of the detectors, it is not necessary to measure the depth-of-interaction. No improvement on the spatial resolution would be observed. Again, in this configuration, when varying between 200 and 1000, the equivalent noise charge of the silicon detectors does not influenced the spatial resolution of the camera.
- A high Z absorber material should be chosen in order to maximise the photo-electric cross-section. Aside from that, the energy resolution of the absorber detector should be as low as possible. LYSO and BGO provide similar spatial resolution and detection efficiency. Because of the lutetium intrinsic radioactivity (which was not taken into account in the simulations), LYSO may not be suitable here, both materials will be compared experimentally.

Discussion

1 Applicability to ion beam monitoring

At this point, we have demonstrated that with a single scattering Compton camera it is possible to reach a detection efficiency of 3×10^{-4} and a spatial resolution of 7 mm in the case of a photon point source with a typical prompt γ-ray energy spectrum. These simulations have to be validated experimentally with monoenergetic sources. This is the scope of tests of the future prototype (detectors have been ordered and have been delivered this 2012 spring).

These results are encouraging, but we have still to determine if it is good enough for a clinical application. The question is: With such performances which observable are we capable to measure during a treatment fraction and with what accuracy ? Ideally we would want to reconstruct a 3D emission map of prompt γ-rays. This map would be compared to a theoretical map obtained by means of simulations. This is what is done currently with the PET technique, yet only after each treatment fraction [Enghardt2004]. This comparison should occur as soon as possible during the irradiation of the patient. It is possible also to limit the reconstruction to 1D profiles and to focus on the position of the fall-off of these profiles. The available statistics is the main limiting factor here.

1.1 Carbon therapy

Let us take the example of an irradiation of 1 Gy to a 120 cm^3 tumour within 39 energy slices and approximately 10 000 raster positions [Kramer2000] (corresponding to about 7×10^8 incident ^{12}C ions). In this case, two Bragg peaks corresponding to two consecutive slices are separated by 3 mm. An emission rate of the order of 4×10^{-3} γ ray per mm and per incident ion for carbon ion beams with an energy of 300 MeV/u is expected before the Bragg peak [TestaMPhd2010] [1].

It is also reasonable to assume that the number of ions emitted during the irradiation of the distal energy slice represents about one tenth of the total number of incident ions [Park2009]. It follows that about 3×10^5 prompt γ-rays are emitted per mm for the distal energy slice. In the current set-up, with a detection efficiency of 3×10^{-4}, we obtain about 9×10^1 γ per mm for the distal energy slice of a 1 Gy treatment fraction.

In this example, the tumour is located between 6 and 11 cm in depth. For the proximal and distal raster position, this correspond respectively to an emission rate of 2.4×10^{-1} γ ray per incident ion and of 4.4×10^{-1} γ ray per incident ion. As mentioned before, the number of ions corresponding to the proximal and distal raster positions is not the same and thus it is difficult to estimate the 3D distribution of detected γ-rays. Yet, if we assume that the 7×10^8 incident ions are equally distributed over the 10 000 raster positions, we obtain a number of detected γ-rays between 5 and 9 per raster position which seems pretty low in any case.

1.2 Proton therapy

For a typical proton therapy treatment, approximately 10^3 γ rays are emitted per cGy delivered in voxels of approximately $1 \times 1 \times 2.5$ mm^3 [Moteabbed2011]. With a detection efficiency of 3×10^{-4}, we detect 3×10^1 γ-rays per Gy per voxels of $1 \times 1 \times 2.5$ mm^3.

[1] Recent investigations of collaborators have shown that it may be necessary to correct this number by a factor between 2 and 3. In any case, this does not modify the conclusions of this chapter.

If we consider only these results, it is difficult to conclude on the feasibility of prompt γ-ray imaging with a Compton camera in carbon or proton therapy. First we need to determine the statistics required to obtain, among other things, an accuracy on the Bragg peak position of the order of 1 mm. Yet, it appears that in the current configuration of the Compton camera 3D monitoring may only be possible for proton therapy. 1D monitoring seems possible for both proton therapy and carbon therapy.

A spatial resolution of 7 mm FWHM is very close to the spatial resolution of clinical PET devices ($\approx$ 5 mm [Jansen2007]). So provided there is enough statistics, we expect to get at least an information comparable to the one given currently by the PET technique (without being disturbed by washout). Moreover, in the case of 1D imaging, determining the fall-off position is an edge-finding problem for which the achievable precision is conditioned not only by the spatial resolution but also by the γ and background statistics.

The spatial resolution depends on the reconstruction algorithm. A more sophisticated iterative algorithm might provide a better spatial resolution at the cost eventually of higher calculation times. Such an algorithm is being developed by collaborators in the CREATIS laboratory.

Part II

Response of the camera in realistic conditions

Before going further in our investigation, we need to test and validate our simulation models. So far, the simulations were limited to a modelling of interactions of photons, electrons and positrons with matter. These interactions are well known and the corresponding interaction models well documented and validated. The main limits come from the models used to reproduce the position and energy recording in the detectors and the detector resolutions. Our simulations with a photon point source will be checked against measurements with radioactive sources as soon as the detectors are available (delivery this spring 2012 for the silicon detectors and at the end of the year for the LYSO and BGO detector).

In the following, we simulate the irradiation of a PMMA phantom by an ion beam and the response of the camera. In the first chapter of this part we present the count rates and energy spectra that a Compton camera is likely to get. This study consists in a comparison of measurements and Monte Carlo simulations. As no detector of the Compton camera is available yet, we performed this validation with a test silicon detector and with a monocrystal $LaBr_3$ detector. The final goal of this study is to extrapolate the measured counting rates to what can be expected in a clinical situation with a full size camera and to discuss the amount of pile-up in the detectors.

In the second chapter we study the response of the full size camera to the irradiation of a PMMA phantom by a proton beam. Four important aspects are detailed: neutron interactions in the detectors, random coicidences, the limits of our reconstruction algorithm and the achievable precision on the Bragg peak position.

CHAPTER II.1

Experimental validation of the simulations

1 Introduction

The measurements were performed in the Heidelberg Ion Therapy Centre (HIT), which started clinical operation in November 2009. It is a synchrotron-based facility equipped with three treatment rooms, two with a horizontal beam line and one with a carbon ion and proton gantry. The ion gantry is the first worldwide as the existing gantries are designed for protons only. The centre also comprises an area dedicated to quality assurance and research, where our experiment took place. Fig. 1 illustrates the layout of the accelerator and treatment level.

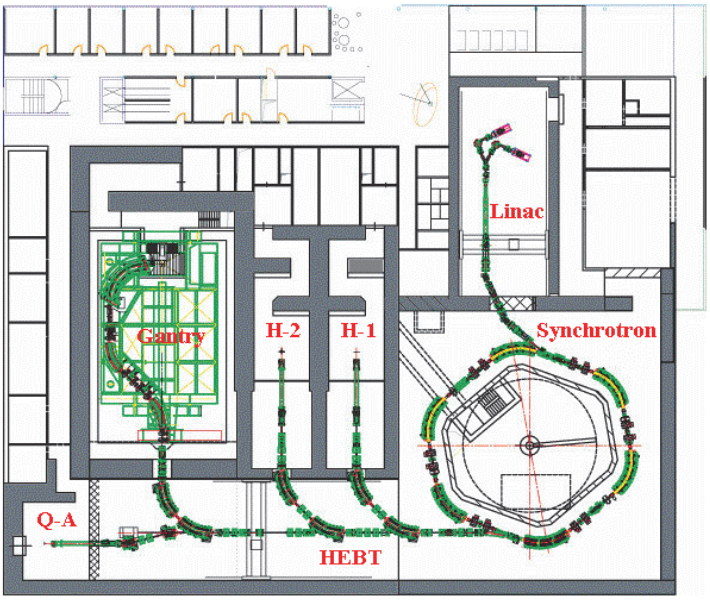

Figure 1: Layout of the first underground floor of the Heidelberg Ion Therapy Centre, housing the accelerator complex [Eickhoff2003]. Q-A stands for quality assurance, H for horizontal beam line, HEBT for high energy beam transport.

2 Method

2.1 Experiment

Both irradiation with a proton beam and a carbon ion beam were performed. The beam parameters are reminded in Table. 1. The beam energy was adjusted to obtain a range of approximately 15 cm in the target.

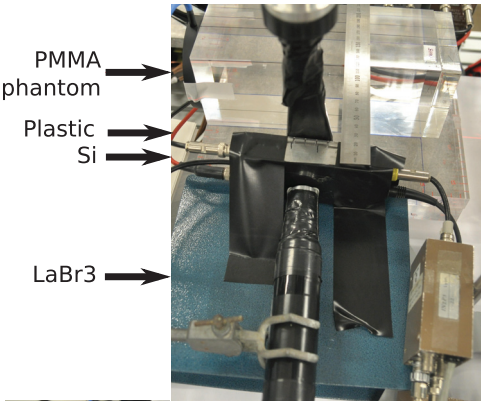

Figure 2: Picture of the experimental set-up.

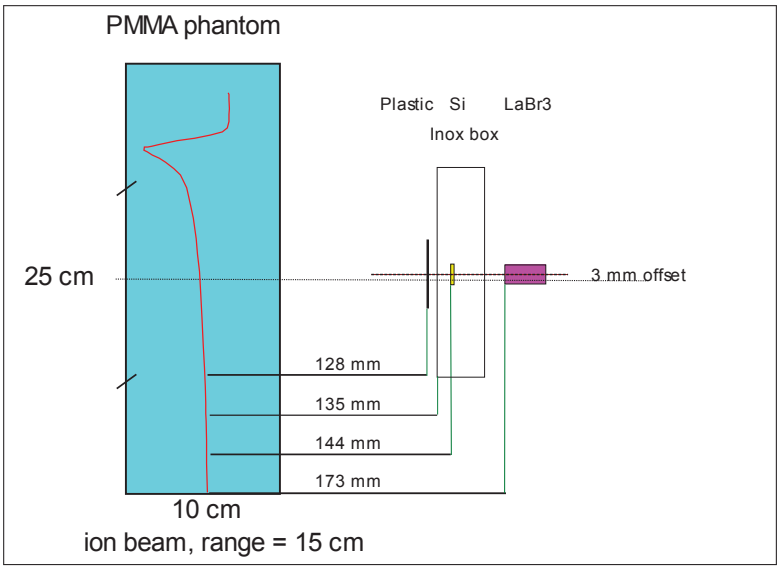

Figure 3: Experimental set-up.

We chose to work with beam currents low enough so that there was no pile up in the detectors. During the irradiation, the number of ions was measured with an ion chamber positioned in the beam.

Table 1: Beam parameters. The corresonding ion range is about 15 cm.

Particle	Energy, MeV/u	Width (FWHM), mm	current, ion.s^{-1}
proton	162.54	10.4 mm	4.4×10^5
carbon ion	310.58	3.6 mm	7.6×10^4

The experimental set-up is represented on Fig. 3. We used a $10 \times 10 \times 25$ cm^3 parallelepiped PMMA target. Our prototype consists of a small test silicon detector of $1.2 \times 1.2 \times 0.2$ cm^3 and a cylindrical $LaBr_3$ detector with a radius of 1.27 cm and a length of 5.08 cm. The silicon detector was held in a 0.8 mm thick inox box measuring $2.8 \times 12.2 \times 6.8$ cm^3.

The silicon detector includes 8 strips on each side. The pitch of the strips is 1.41 mm and their width 1.31 mm. All strips of the p side of the silicon detector were connected together and the resulting signal was used to measure the energy deposited in the detector. The positions of the interactions occurring in the detector were not measured. Similarly, we used the output signal of a photomultiplier connected to the $LaBr_3$ detector to measure the energy deposited in this detector.

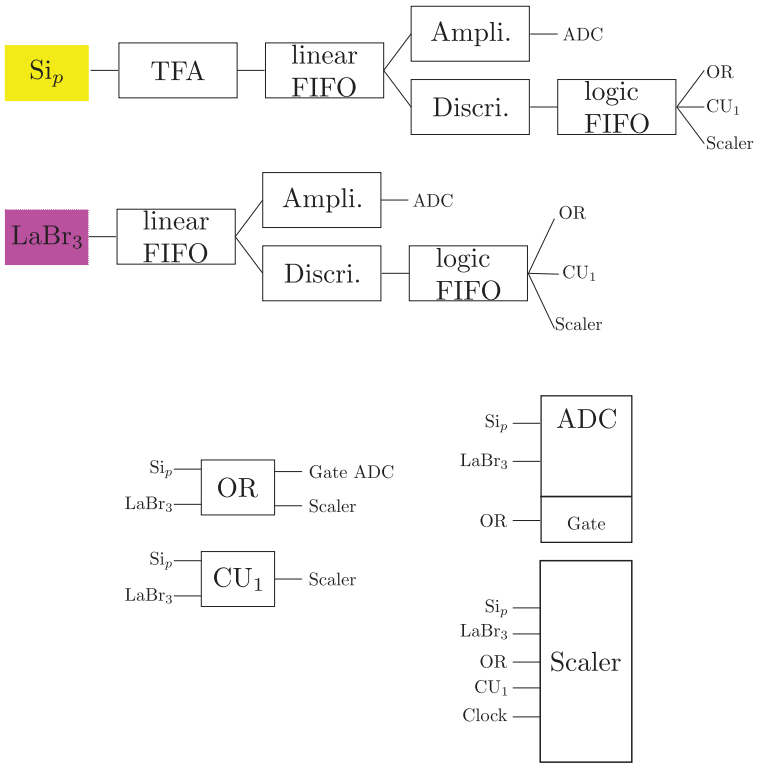

Figure 4: Acquisition set-up: TFA stands for timing filter amplifier, FIFO for fan-in fan-out, Ampli. for amplifier, Discri. for Discriminator and CU for coincidence unit.

The acquisition system is illustrated on Fig. 4. Note that the strips of the p side were connected together and then sent to a preamplifier, the corresponding signal was amplified by a fast amplifier (TFA) and then by a spectroscopic amplifier. After amplification and shaping, we used an ADC triggered by the OR of the signals from the Si and $LaBr_3$ detectors. Energy calibration was performed afterwards with a ^{22}Na source. To account for the acquisition dead time, the count rates were also recorded with a scaler. The thresholds of the discriminator used to convert the analog signals into logical ones correspond to 350 keV for the Si detector and 180 keV for the $LaBr_3$ detector. The maximum amplitude of the signals that was recorded is 10 MeV for the Si detector and 26 MeV for the $LaBr_3$ detector. Finally, with a coincidence unit we recorded the number of coincidences between the Si and $LaBr_3$ detectors within a time window of approximately 100 ns. The energy deposited in the detectors in coincidence was obtained by software sorting.

Dead time was taken into account by weighting the number of incident ions (obtained with the ionisation chamber) delivered in the target by the ratio between the number of events acquired by the ADC unit and the counts, on the scaler, of the output of the OR unit. All experimental data was then normalised by this effective number of incident ions. The noise due to the radioactivity induced in the target by the prior irradiation was removed by subtracting, for each signal of interest, the corresponding signal acquired just after the irradiation.

2.2 Simulations

All simulations have been carried out with Geant4 9.4. The models used for the different processes for the hadrons are detailed in Table. 2.

The electromagnetic interactions were simulated using the “standard electromagnetic option 3“ physics list of Geant4. For all charged particles, it describes ionisation, bremsstrahlung and multiple Coulomb scattering. For positrons, it describes also annihilation. It includes also photon interactions: the photoelectric

Table 2: Models used for the hadrons

Process	protons	ions	neutrons
Electromagnetic	$\text{standard}_{\text{option3}}$		
Inelastic	G4BinaryCascade	G4QMDReaction (G4IonsShenCrossSection)	G4BinaryCascade + G4NeutronHPInelastic (<19 MeV)
Elastic	G4LElastic + G4NeutronHPElastic (<19 MeV - for neutrons only) or G4HadronElastic		
Fission	/	/	G4LFission + G4NeutronHPFission(<19 MeV)
Capture	/	/	G4LCapture + G4NeutronHPCapture (<19 MeV)
Radioactive decay	/	G4Radioactivedecay	/

effect, Compton scattering including Doppler broadening, pair creation and Rayleigh scattering. For the photoelectric effect and Compton scattering, fluorescence and Auger electron production were included. In Geant4, some electromagnetic processes require a threshold, below which no secondary particle is generated. This threshold should be defined as a distance, or range cut-off, which is internally converted to an energy for individual materials. It was set to 0.1 mm in the target and in the detectors and to 1 mm elsewhere.

To describe the inelastic interactions of hadrons, we used the QMD model. Elastic scattering was also included in the physics list with either the G4LElastic model or the G4HadronElastic model. For neutrons, the fission and capture processes were included. Note also that for all neutron processes, the high precision models were systematically used for energies below 19 MeV. Finally G4RadioactiveDecay was used to model the radioactive decay of ions.

The simulations were performed in two steps. In a first set of simulations, all information concerning the particles coming out of the phantom towards the detectors was recorded in a .root file. The beam spatial distribution was modelled by a Gaussian distribution, the proton beam FWHM is 10.4 mm and the carbon-ion beam FWHM is 3.6 mm. No time structure or energy distribution was applied.

Then, in a second set of simulations, all particles previously recorded were emitted towards the camera and information concerning the interactions in the detectors was recorded in a .root file. The geometry included the three detectors and the inox box containing the silicon detector. The origin of the coordinate system is the centre of the phantom. The energy resolution of the detectors was not taken into account in the simulations.

3 Results

3.1 Proton beam

Figure 5 compares the measured and simulated spectra for the Si and $LaBr_3$ detectors in the case of the irradiation of the target by the proton beam. These simulations used the G4LElastic model. Up to 3 MeV and after 6 MeV, the difference between the simulated and measured spectra for the Si detector is lower than the measurement uncertainty. Yet, between 3 and 6 MeV, there is a huge discrepancy between the two spectra. Figure 6 illustrates the contribution to the simulated spectra of γ rays, neutrons, all protons, primary protons and electrons. We observe that this discrepancy can be attributed to interactions of protons, and mostly primary protons. These primary protons interact in the detectors after an elastic scattering in the target. The distribution of the incident energy of all the primary protons interacting in the silicon detectors and of the position of their origin in the target, obtained from the simulations, are represented on Fig. 7. They have an energy between 20 and 120 MeV and come from the first half of the beam path. The 20 MeV protons impinge on the silicon detector with an angle around 90 degrees and deposit approximately 9 MeV. The 120 MeV protons impinge on the silicon detector with an angle around 40 degrees and deposit approximately 3 MeV. Fig. 8 (top) shows the same comparison for simulations that use a different model describing hadron elastic scattering: G4HadronElastic. We observe indeed a significant reduction of the number of events

between 3 and 6 MeV, and the agreement between the simulated and the measured spectrum is much better. This means that the model G4LElastic is not adapted for the simulations of ion beam therapy applications, and that the model G4HadronElastic should be used instead.

For the $LaBr_3$ detector, the shape of the measured spectrum is well reproduced by the simulations over all the energy range (with both the G4LElastic and the G4HadronElastic models). Yet, the simulations overestimate the number of events between 1 and 4 MeV. In this energy domain, mostly gamma rays interact in the detector. This suggests that the production of prompt γ-rays by the simulation can be improved, in this case the binary cascade model is at stake. After 15 MeV, we observe that the simulations underestimate the number of events. The most likely explanation is that the simulations do not include the environment, and thus do not take into account the production of high energy radiationin this environment (in particular in the beam nozzle). No significant discrepancy corresponding to interactions of primary protons was observed with the G4LElastic model, because most of these protons deposit more than 26 MeV in this detector.

Figure 9 compares the measured and simulated spectra (with the G4HadronElastic model) for the Si and $LaBr_3$ detectors in coincidence in the case of the irradiation of the target by the proton beam. For the Si detector, the measured spectrum in coincidence with the $LaBr_3$ detector is pretty well reproduced by simulations except below 1 MeV where the simulations overestimate the measurements by a factor of 5. For the $LaBr_3$ detector, as events are distributed over a large energy range, statistics is low and it is not easy to conclude on the agreement between simulations and measurements. Yet, it seems that the simulations overestimate the measurements over the entire energy range.

Table 3 summarises the comparison of the measured and simulated yields of interaction in both detectors for the simulations using the G4HadronElastic model. For each detector, we selected two energy ranges: one corresponding to the complete range of the acquisition system for that detector and the other corresponding to the energy domain where take place most of the γ-ray interactions. For the Si detector, this last domain corresponds to [0.35-3 MeV], and for the $LaBr_3$ detector to [0.18-15 MeV] (see Fig. 6). For the single events, the results are pretty satisfactory, the simulations manage to reproduce the yields of interaction with an accuracy better than 17 %. For the coincidence events, huge discrepancies between simulations and measurements, that are not explained today, remain.

Table 3: Detected yields, counts.incident ion^{-1} - proton beam

Si			
Energy range	Simulation (G4HadronElastic)	Experiment	Difference(G4HadronElastic)
[0.35-10 MeV]	5.60×10^{-06}	6.67×10^{-06}	-16.7%
[0.35-3 MeV]	2.83×10^{-06}	2.90×10^{-06}	-2.4 %
$LaBr_3$			
Energy range	Simulation (G4HadronElastic)	Experiment	Difference (G4HadronElastic)
[0.18-26 MeV]	2.09×10^{-04}	2.05×10^{-04}	1.9 %
[0.18-15 MeV]	2.06×10^{-04}	1.97×10^{-04}	4.5 %
Coincidence			
Energy range	Simulation (G4HadronElastic)	Experiment	Difference (G4HadronElastic)
Si [0.35-10 MeV] $LaBr_3$ [0.18-26 MeV]	4.3×10^{-07}	1.92×10^{-07}	124%
Si [0.35-3 MeV] $LaBr_3$ [0.18-15 MeV]	2.43×10^{-07}	1.35×10^{-07}	40 %

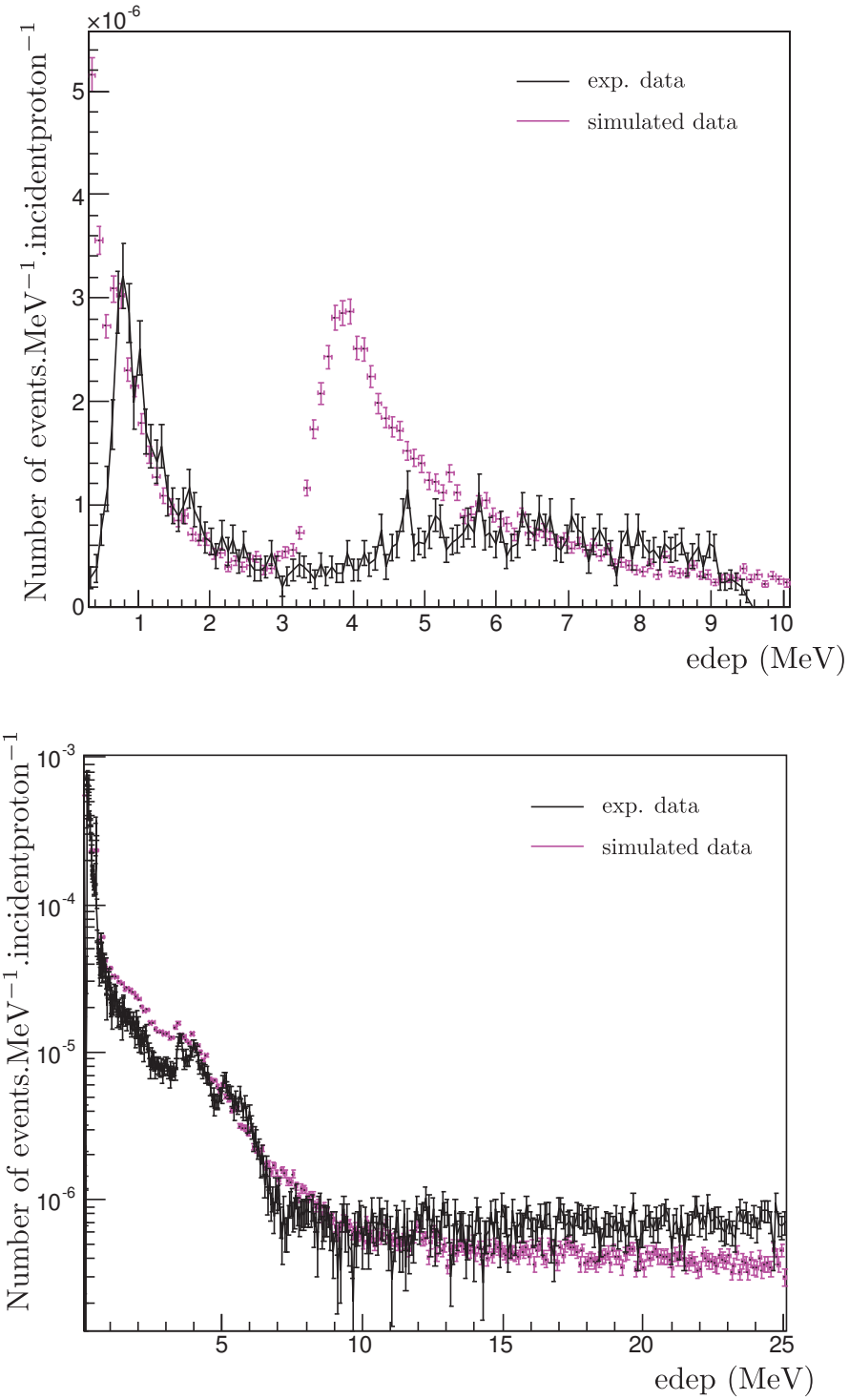

Figure 5: Comparison of the measured and simulated spectra for the single events for the Si (top) and $LaBr_3$ (bottom) detectors in the case of the irradiation of the target by the proton beam of 163 MeV. These simulations used the G4LElastic model.

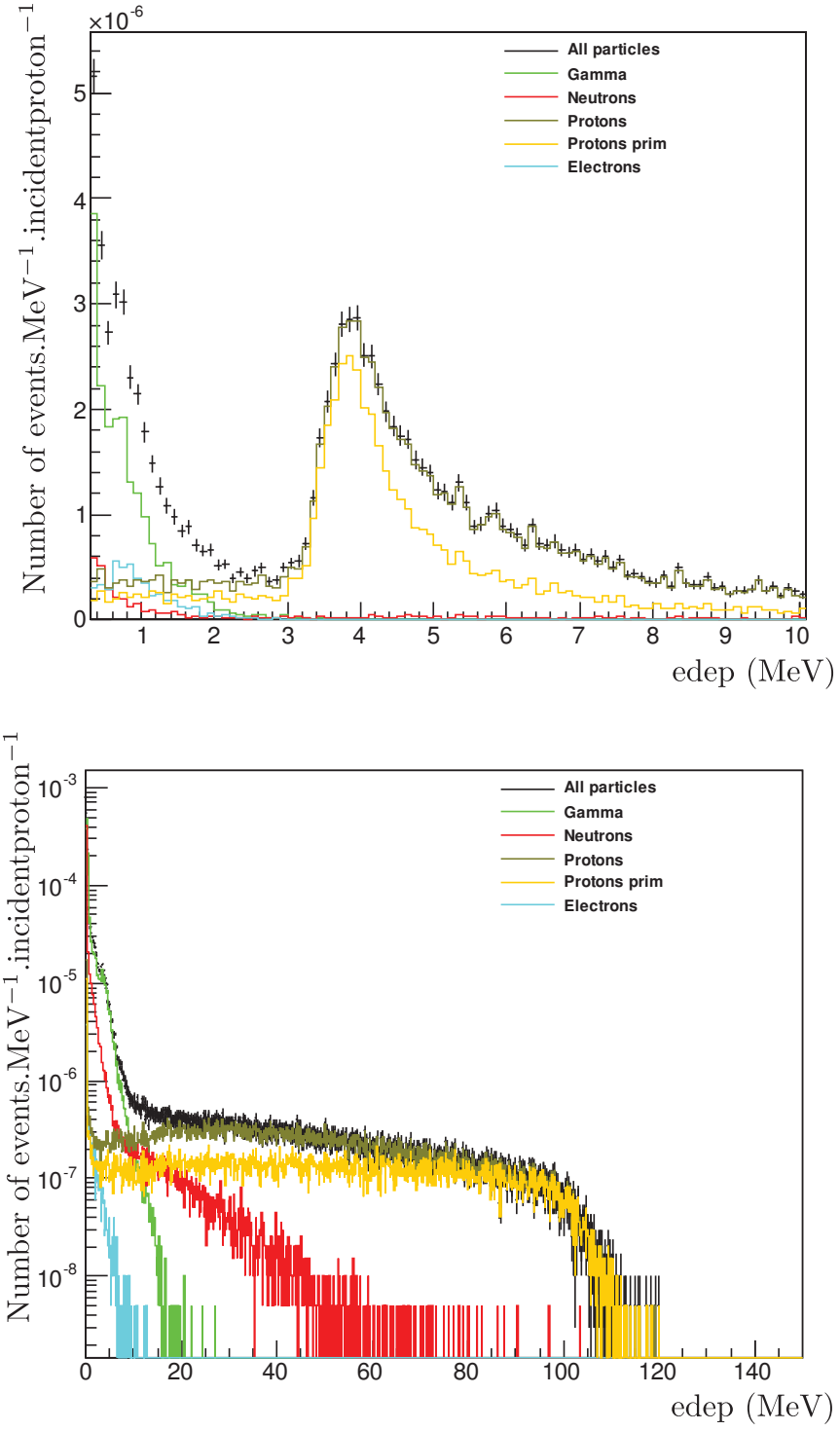

Figure 6: Contribution to the simulated spectra of γ rays, neutrons, all protons, primary protons and electrons for the single events for the Si (top) and $LaBr_3$ (bottom) detectors in the case of the irradiation of the target by the proton beam of 163 MeV. These simulations used the G4LElastic model.

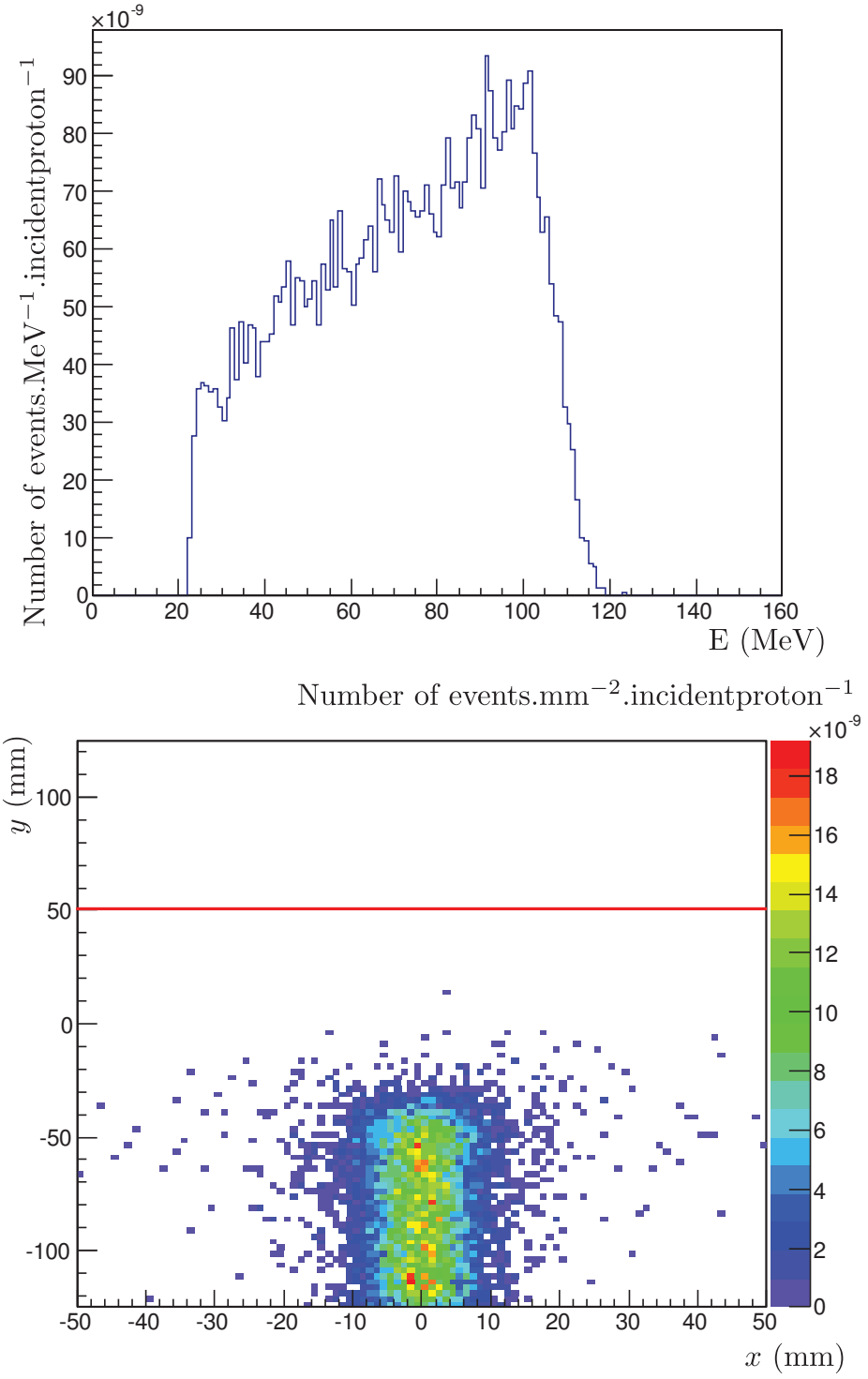

Figure 7: Distribution of the energy which exit of the target of the primary protons which interact in the Si detector (top) and of the position of their origin in the target (bottom). The red line indicates the Bragg peak position. These simulations used the G4LElastic model.

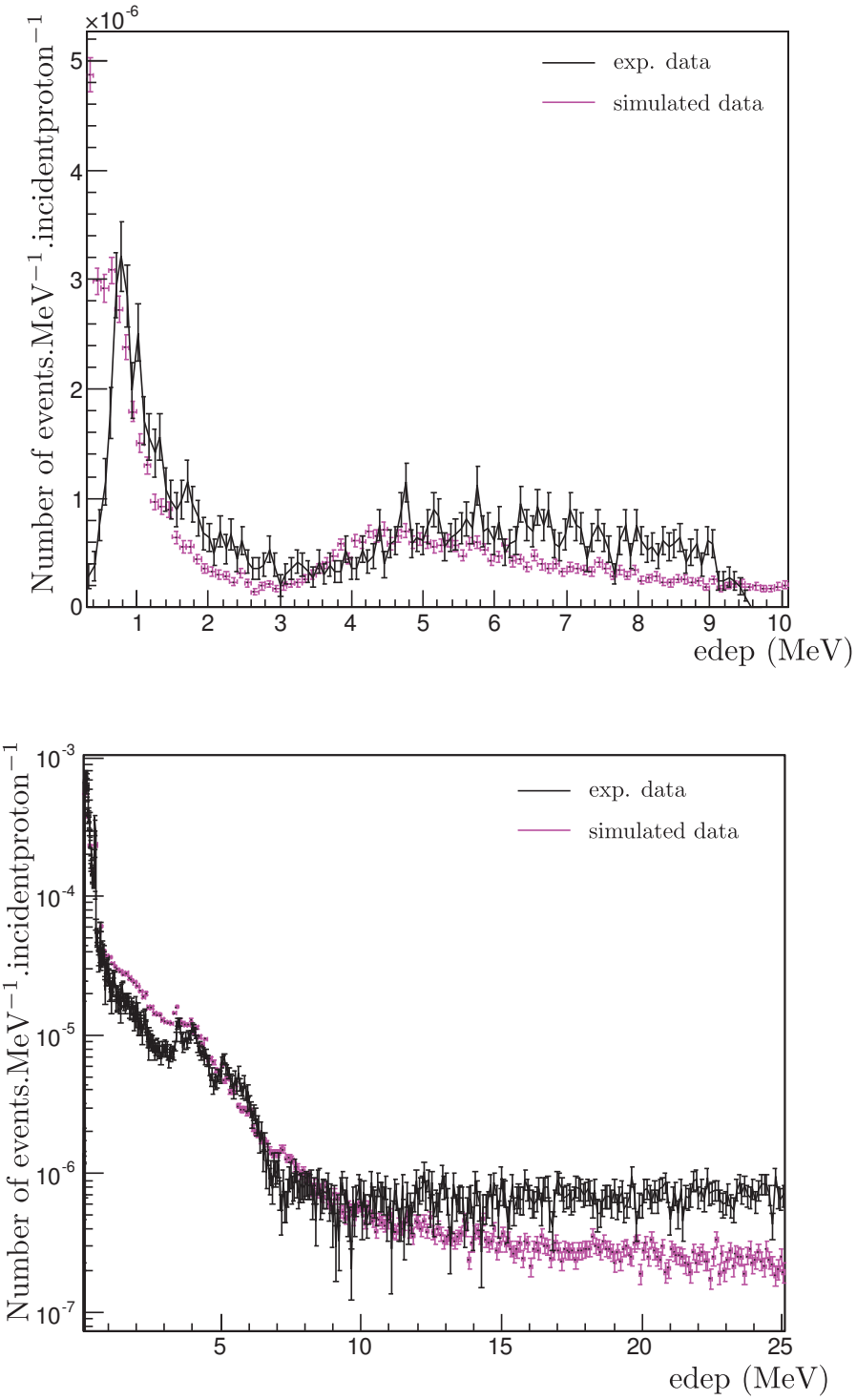

Figure 8: Comparison of the measured and simulated spectra for the single events for the Si (top) and $LaBr_3$ (bottom) detectors in the case of the irradiation of the target by the proton beam of 163 MeV. These simulations used the G4HadronElastic model.

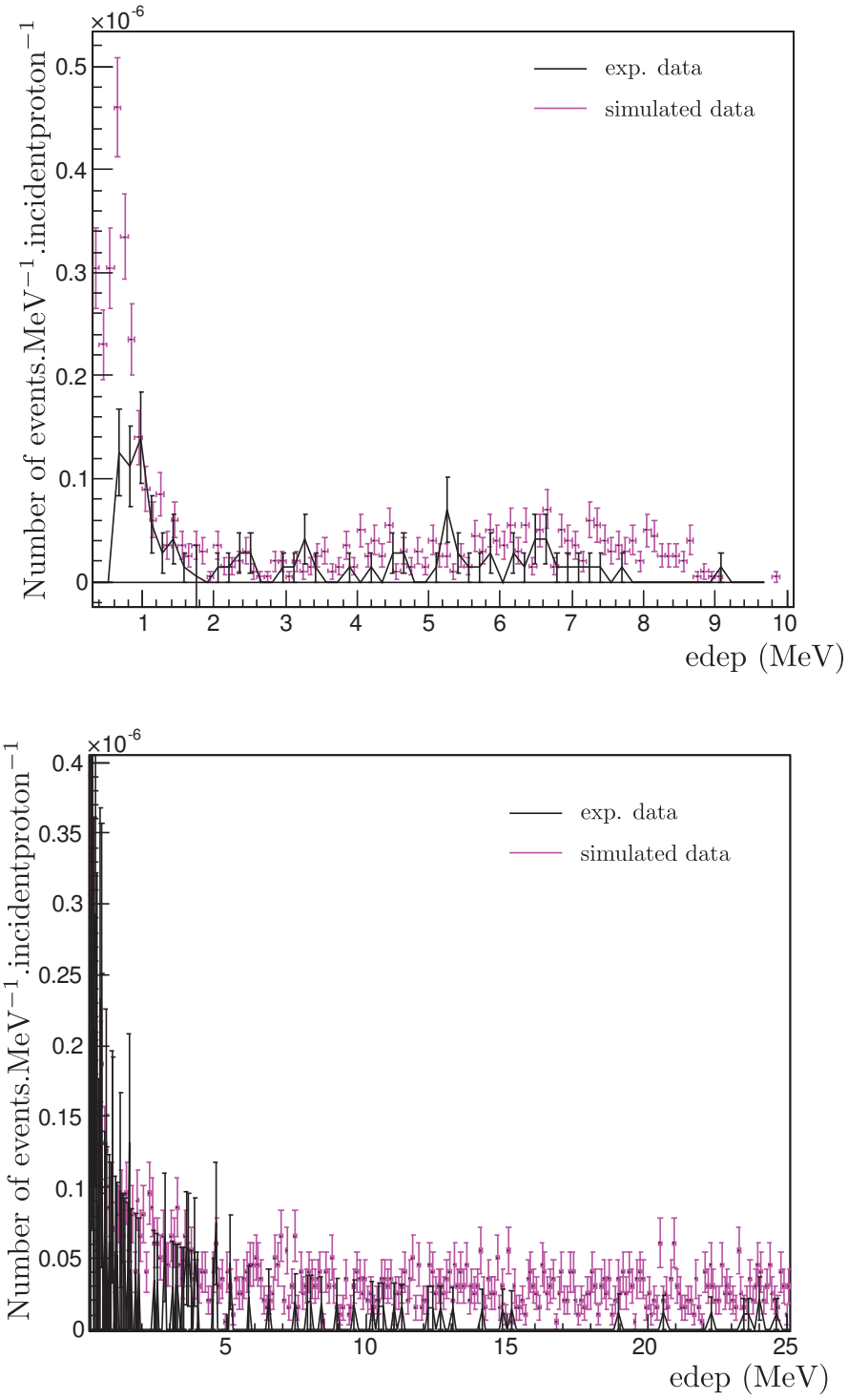

Figure 9: Comparison of the measured and simulated spectra in coincidence for the Si (top) and $LaBr_3$ (bottom) detectors in the case of the irradiation of the target by the proton beam of 163 MeV. These simulations used the G4HadronElastic model.

3.2 Carbon beam

Figure 10 compares the measured and simulated spectra for the Si and $LaBr_3$ detectors in the case of the irradiation of the target by the Carbon ion beam. These simulations used the G4HadronElastic model. In this case, the shape of both spectra is well reproduced by the simulations. For the Si detector, the simulation underestimates the number of events between 800 keV and 2 MeV. For the $LaBr_3$ detector, the observations (and thus the corresponding explanations) are similar to the proton beam case: the simulations overestimate the number of events between 1 and 4 MeV because of problems with prompt γ-ray production in the simulations and the simulations underestimate the number of events after 15 MeV because they do not take into account the noise generated by the radiation produced in the environment.

Figure 11 illustrates the contribution to the simulated spectra of γ rays, neutrons, protons and electrons. The main difference with the case of proton therapy is the high number of secondary protons produced during the irradiation. Note that in this case the secondary protons are produced by nuclear reactions. This why, here, no significative difference was observed between the simulations using the G4LElastic or the G4HadronElastic model (graphs not shown).

Figure 12 compares the measured and simulated spectra (with the G4HadronElastic model) for the Si and $LaBr_3$ detectors in coincidence in the case of the irradiation of the target by the carbon beam. For the Si detector, the measured spectra in coincidence with the $LaBr_3$ detector is pretty well reproduced by simulations. Yet, a slight shift remains between 5 and 9 MeV. Again for the $LaBr_3$ detector, as events are distributed over a large energy range, statistics is low and it is not easy to conclude on the agreement between simulations and measurements.

Table 4 summarises the comparison of yields of interaction in both detectors for simulation and measures. In the case of carbon therapy, simulations are able to reproduce the measurements with an agreement better than 14 %, even for coincidence events.

Table 4: Detected yields, counts.incident ion^{-1} - carbon beam

Si			
Energy range	Simulation (G4HadronElastic)	Experiment	Difference (G4HadronElastic)
[0.35-10 MeV]	1.81×10^{-04}	1.99×10^{-04}	-9.0 %
[0.35-3 MeV]	7.94×10^{-05}	9.18×10^{-05}	-13.5 %
$LaBr_3$			
Energy range	Simulation (G4HadronElastic)	Experiment	Difference (G4HadronElastic)
[0.18-26 MeV]	1.96×10^{-03}	2.25×10^{-03}	-12.8 %
[0.18-15 MeV]	1.87×10^{-03}	2.07×10^{-03}	-9.6 %
Coincidence			
Energy range	Simulation (G4HadronElastic)	Experiment	Difference (G4HadronElastic)
Si [0.35-10 MeV] $LaBr_3$ [0.18-26 MeV]	1.71×10^{-05}	1.65×10^{-05}	3.6 %
Si [0.35-3 MeV] $LaBr_3$ [0.18-15 MeV]	6.09×10^{-06}	6.70×10^{-06}	-6.5 %

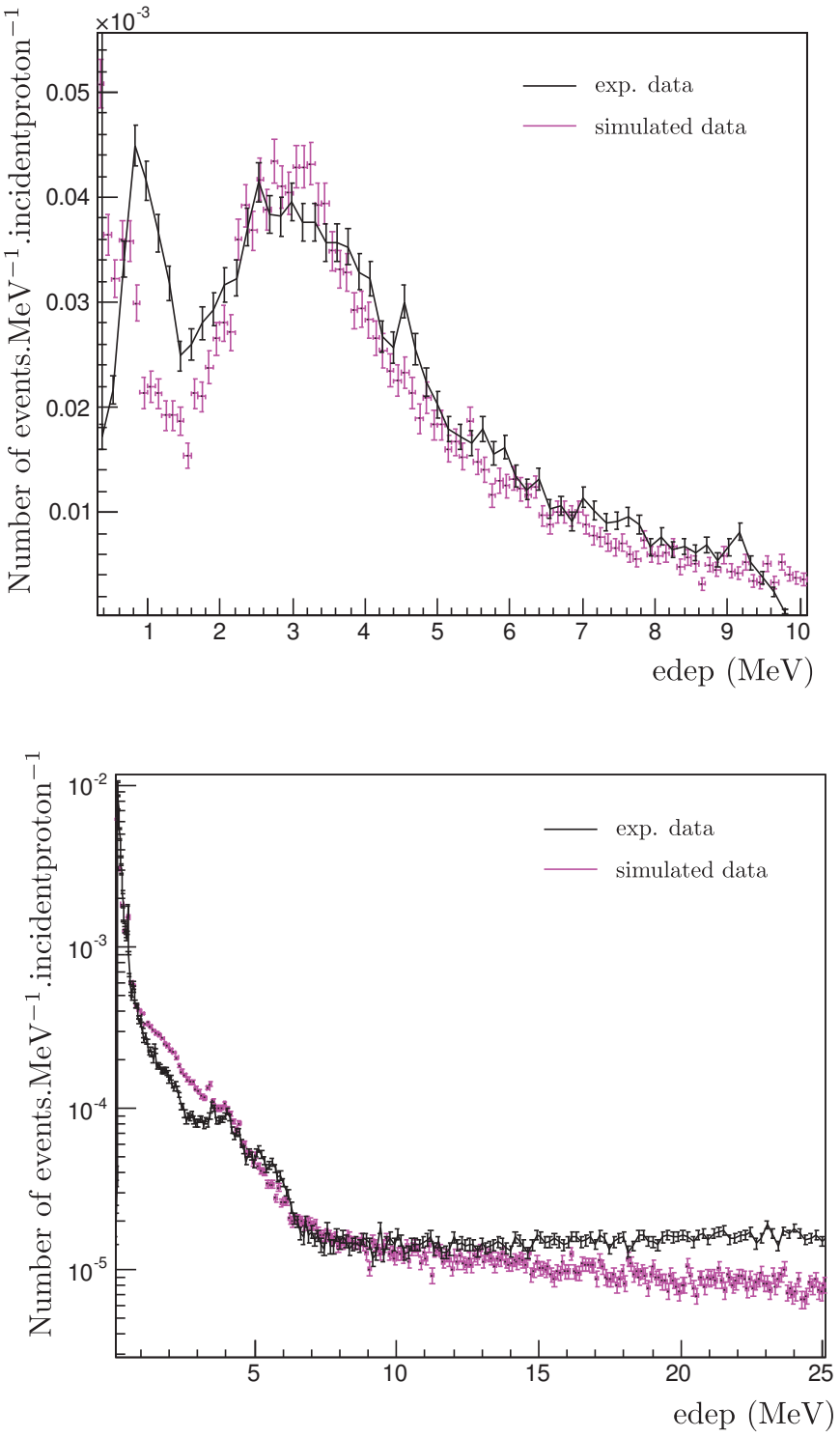

Figure 10: Comparison of the measured and simulated spectra for the single events for the Si (top) and $LaBr_3$ detectors in the case of the irradiation of the target by the carbon beam of 311 MeV/u. These simulations used the G4HadronElastic model.

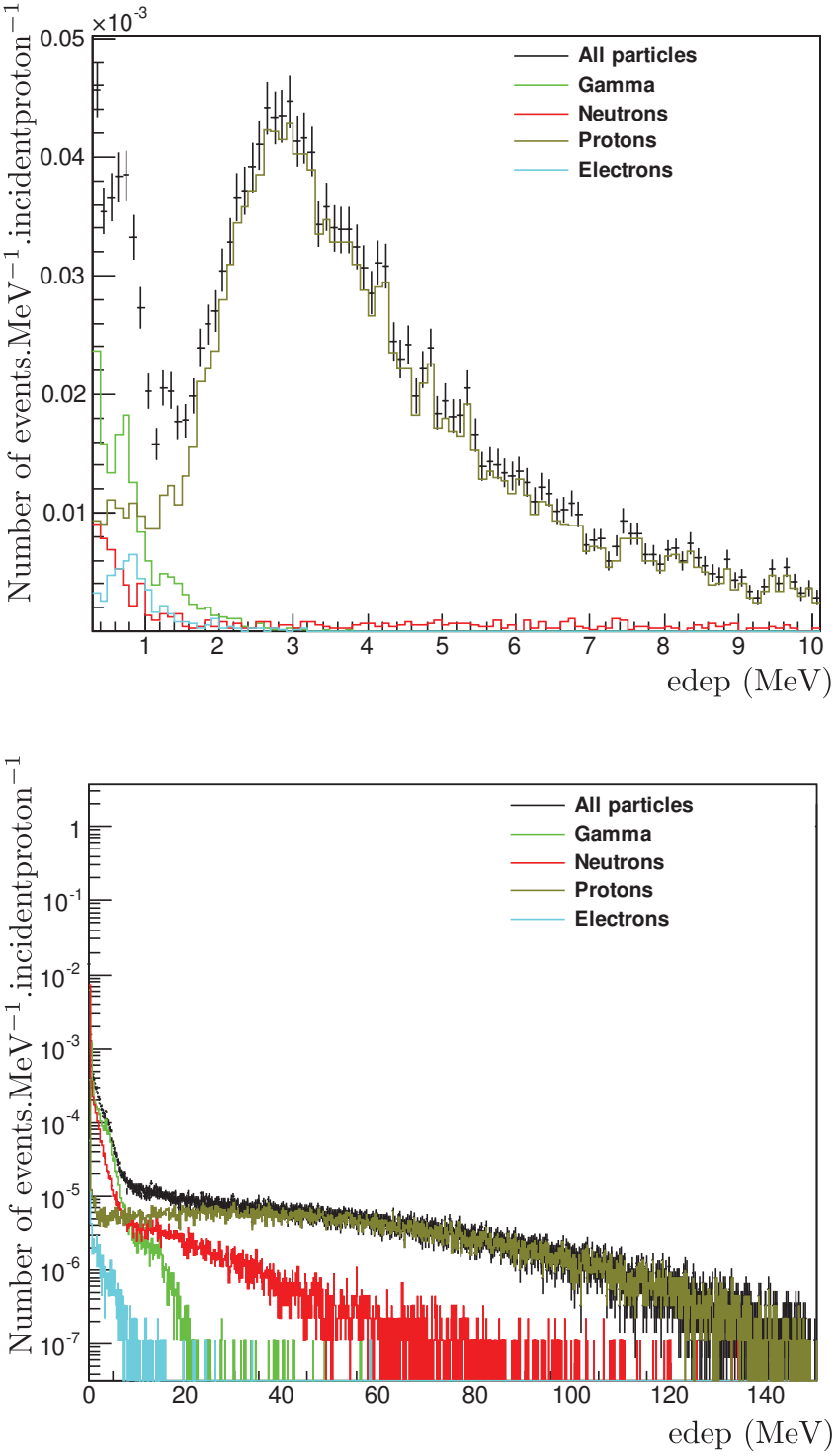

Figure 11: Contribution to the simulated spectra of γ rays, neutrons, all protons, primary protons and electrons for the single events for the Si (top) and $LaBr_3$ detectors in the case of the irradiation of the target by the carbon beam of 311 MeV/u. These simulations used the G4HadronElastic model.

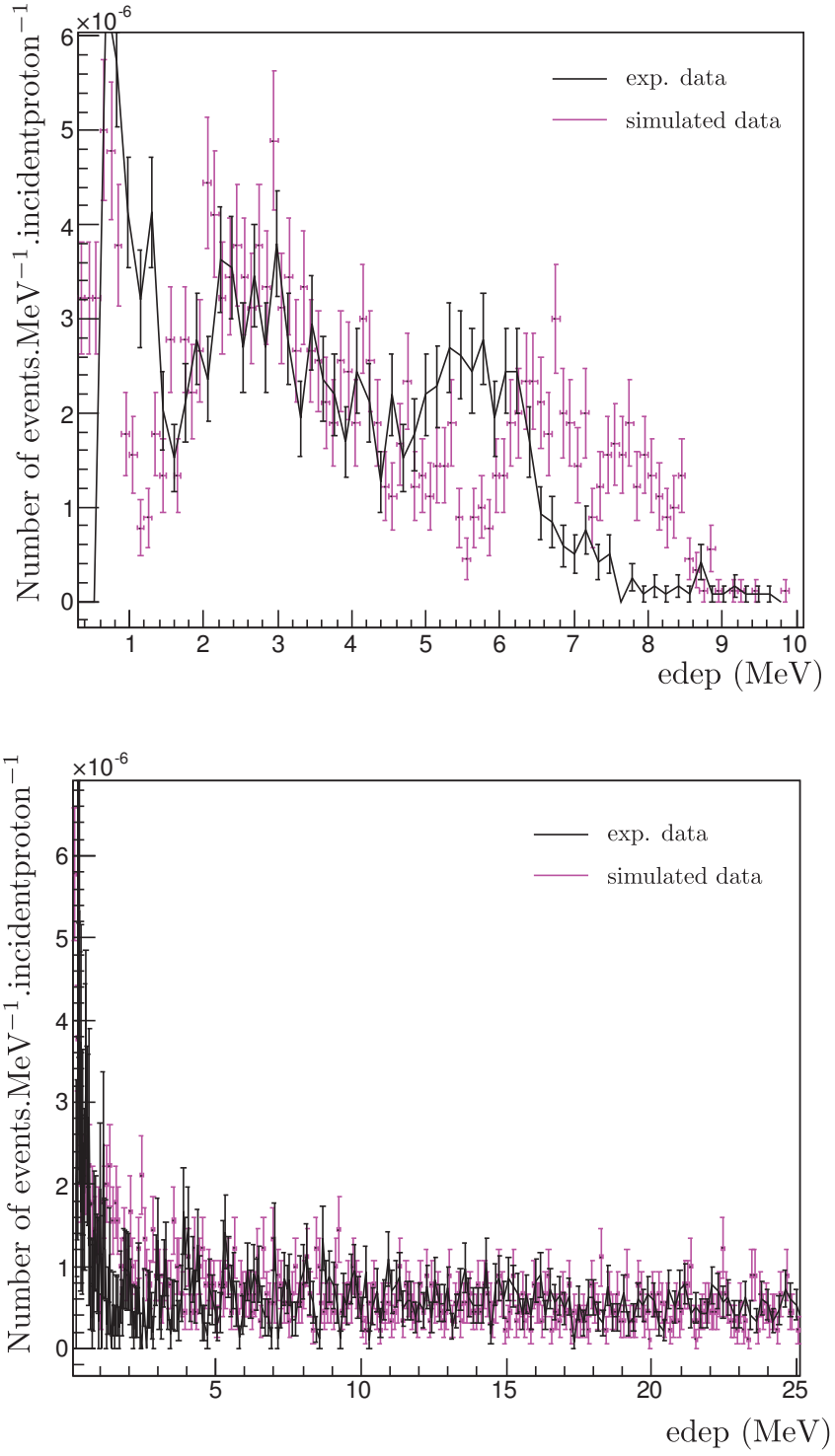

Figure 12: Comparison of the measured and simulated spectra in coincidence for the Si (top) and $LaBr_3$ detectors in the case of the irradiation of the target by the carbon beam of 311 MeV/u. These simulations used the G4HadronElastic model.

4 Discussion

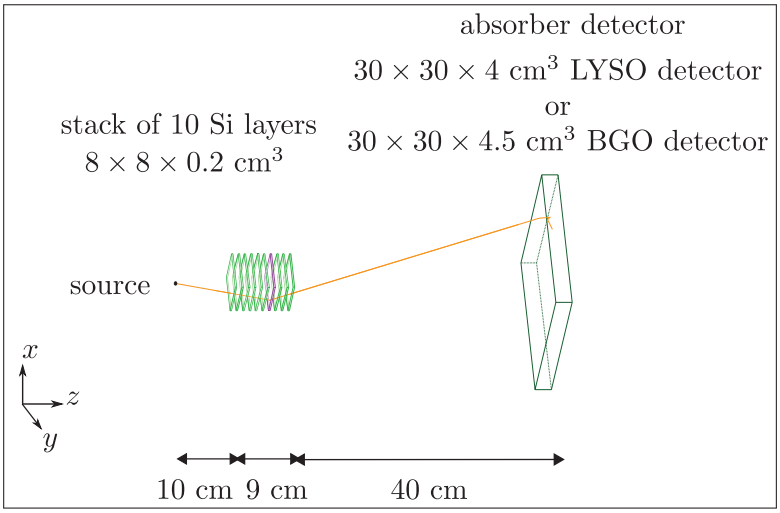

Figure 13: Final configuration of the single scattering Compton camera

The second goal of this experiment is to deduce the count rates expected with full size detectors r_e, from the measured count rates r_m and thus evaluate pile-up. First, I evaluated the solid angle covered by each detector in the two setups: the small size prototype used in the Heidelberg experiment, and the full size detectors that we plan to use in our future prototype. The geometry of the last set-up is represented in Fig. 13. In the simulations, the cameras were irradiated by a photon line source of 15 cm long corresponding to the range of a 160 MeV proton beam or a 310 MeV/u carbon ion beam in water. The emission probability was constant along the 15 cm and the photon energy distribution corresponds to the prompt γ-ray energy spectrum used previously (see Fig. 5 of chap. I.1). The solid angle covered by each detector $\Omega/4\pi$ was calculated as the ratio between the number of events where a particle reaches this detector and the number of incident particles. Then I calculated the count rates in the full size detectors as follow:

$$r_e = r_m \times \frac{\Omega_{\text{fullsize}}/4\pi}{\Omega_{\text{smallsize}}/4\pi} \tag{II.1.1}$$

To obtain the number of counts expected in the LYSO detector, the number of counts measured in the $LaBr_3$ detector should be also multiplied by the ratio of the probability of interactions $\frac{P_{\text{LYSO}}}{P_{\text{LaBr}_3}}$ in both detectors:

$$\frac{P_{\text{LYSO}}}{P_{\text{LaBr}_3}} = \frac{1 - e^{-\sigma_{\text{LYSO}} \times \rho_{\text{LYSO}} \times t_{\text{LYSO}}}}{1 - e^{-\sigma_{\text{LaBr}_3} \times \rho_{\text{LaBr}_3} \times t_{\text{LaBr}_3}}}, \tag{II.1.2}$$

where σ_{LYSO} is the mass energy absorpion coefficient in $\text{cm}^2.\ \text{g}^{-1}$, ρ_{LYSO} the mass density in g.cm^{-3} and t_{LYSO} the thickness of the detector in cm. In the energy range considered ($\approx$ [0.1-10 MeV]) and for the chosen geometry, this ratio varies between 1 @ 0.1 MeV (in scintillator detectors of a few centimetres, all 0.1 MeV photons interact) and $\approx$ 1.2 @ 10 MeV for LYSO and BGO. The values used in this calculation are reminded in Table 5, the attenuation coefficients were obtained from the XCOM database. All following calculations were made using a ratio of 1.2 for LYSO and BGO. A ratio of 1 was used for the silicon detectors, as they have the same thickness in both setups.

Table 6 gives the yields per incident ion measured with the small size detectors and the corresponding solid angles obtained with Geant4. Table 7 gives the solid angles covered by the full size detectors obtained with Geant4 and the corresponding count rates deduced from Eq. II.1.1 and Eq. II.1.2. The number of counts per second was calculated using an incident rate of 10^{10} incident proton.s^{-1} and 10^8 incident carbon ion.s^{-1}. These numbers correspond to the maximum values that are used in clinical routine and thus to a worst case scenario.

Table 5: Characteristics of the detectors

	σ @ 0.1 MeV, cm^2.g^{-1}	σ @ 10 MeV, cm^2.g^{-1}	ρ, g.cm^{-3}	t, cm
$LaBr_3$	1.28	3.60×10^{-02}	5.08	5.08
LYSO	2.96	4.00×10^{-02}	7.13	4
BGO	3.97	4.26×10^{-02}	6.5	4.5

Table 6: HIT set-up, number of events per incident ion

	Measured yield - proton case	Measured yield - carbon case	$\Omega/4\pi$
Si	6.67×10^{-06}	1.99×10^{-04}	4.07×10^{-04}
$LaBr_3$	2.05×10^{-04}	2.25×10^{-03}	1.56×10^{-03}

The arrival of counts in the detectors is a random process characterised by a constant probability of occurrence per unit time[1]. Such a serie follows a Poisson probability law. Here we want to determine the probability, assuming that an event occurred at t=0, that the next event takes place after a time higher than τ. This is the probability that no event occurs over an interval of length τ for which the average number of events should be $r\tau$, where r is the probability of occurrence per unit time. The probability that x interactions happen before t=τ, can be expressed as follow:

$$P(x) = \frac{(r\tau)^x e^{-r\tau}}{x!}. \tag{II.1.3}$$

And thus, the probability that no interaction happens before t=τ is $P(0) = e^{-r\tau}$. Experimentally τ corresponds to the length of the detected signal. For the Si detector it is of the order of 1 µs. For a scintillator detector, it is fixed by the decay time of the material. It is of the order of five decay times. This corresponds to 200 ns for the LYSO detector and 1.5 µs for the BGO detector. If we want $P(0)$ >90 %, this requests $r < 1\times10^5$ count.s^{-1} for the Si detectors, $r < 5\times10^5$ count. s^{-1} for the LYSO detector and $r < 7\times10^4$ count.s^{-1} for the BGO detector.

This condition is not verified by the detectors. To minimise pile-up effects, the yield of interactions needs to be reduced by a factor of 50 in the Si detectors, a factor of 100 in the LYSO detector and a factor of 1000 in the BGO detector, in the case of proton therapy. In carbon therapy, the situation is less critical, the yield of interactions should be reduced by a factor of 10 in the Si detectors, a factor of 5 for the LYSO detector and a factor of 30 in the BGO detector. Moving the camera away from the target or decreasing the size of the absorber detector is a first possibility, yet it will not be sufficient. For the Si detectors, the condition $P(0)$ >90 % is verified for each of the 64 strips. It means that in the case where two particles interact during the same 1 µs in one Si detector, it is most likely that they interact on different strips. So, the signal read out by each strip is not affected by pile up, yet it may be difficult to associate the X and Y strips together. For the absorber detector, it is also possible to segment the detector. Finally we should keep in mind that all the calculations were made for the highest beam current used in clinical routine. In any case, the situation remains challenging.

[1] all the arguments used in this § were adapted from [Knoll2012].

Table 7: Full size detectors, number of events per incident ion and number of events per second

		proton beam		carbon beam	
	$\Omega/4\pi$	count.incident ion^{-1}	count.s^{-1}	count.incident ion^{-1}	count.s^{-1}
Si 1	2.69×10^{-02}	4.42×10^{-04}	4.42×10^{06}	1.31×10^{-02}	1.31×10^{06}
Si 2	2.38×10^{-02}	3.90×10^{-04}	3.90×10^{06}	1.16×10^{-02}	1.16×10^{06}
Si 3	2.11×10^{-02}	3.46×10^{-04}	3.46×10^{06}	1.03×10^{-02}	1.03×10^{06}
Si 4	1.81×10^{-02}	2.97×10^{-04}	2.97×10^{06}	8.85×10^{-03}	8.85×10^{05}
Si 5	1.72×10^{-02}	2.82×10^{-04}	2.82×10^{06}	8.41×10^{-03}	8.41×10^{05}
Si 6	1.47×10^{-02}	2.41×10^{-04}	2.41×10^{06}	7.19×10^{-03}	7.19×10^{05}
Si 7	1.35×10^{-02}	2.21×10^{-04}	2.21×10^{06}	6.60×10^{-03}	6.60×10^{05}
Si 8	1.21×10^{-02}	1.98×10^{-04}	1.98×10^{06}	5.92×10^{-03}	5.92×10^{05}
Si 9	1.10×10^{-02}	1.80×10^{-04}	1.80×10^{06}	5.38×10^{-03}	5.38×10^{05}
Si 10	1.01×10^{-02}	1.66×10^{-04}	1.66×10^{06}	4.94×10^{-03}	4.94×10^{05}
LYSO/BGO	1.91×10^{-02}	2.51×10^{-03}	2.51×10^{07}	2.75×10^{-02}	2.75×10^{06}

CHAPTER II.2

Response of the camera in the case of the irradiation of a PMMA target by a 160 MeV proton beam

1 Method

In this chapter, the answer of the single scattering Compton camera optimised in the first part is studied in the case of the irradiation of a PMMA phantom by a monoenergetic proton beam. We want to reconstruct the position of the emission points of the prompt γ-rays. Here, reconstruction is limited to 1D reconstruction, i.e. we reconstruct the position of the emission points along the beam path given by the hodoscope. To reconstruct this 1D profile, specific interaction schemes are to be selected: one interaction in a single layer of the scatter detector and one interaction in the absorber detector. Ideally these interactions correspond to a Compton scattering, without energy escape, of a γ ray in the scatter detector and a full absorption of this γ ray in the absorber detector. Experimentally, these events will be selected by means of logical operations between the signals of the scatter detector layers and of coincidence units. We can sort out these events into two categories:

- real coincidences, which correspond to the interactions of the same particle in the scatter detector and the absorber detector;
- random coincidences, which correspond to interactions of two different particles coming out of the phantom in the scatter and the absorber detector.

The first goal of this study is to determine the consequences of the interactions in the detectors of particles other than γ rays on the reconstruction of the γ-ray profile. The first point is to determine whether time-of-flight measurements are required to suppress the neutron background or not. Then, we evaluate the amount of random coincidences expected with a realistic beam time-structure. Finally, we propose a method to quantify the achievable accuracy on the position of the dose fall-off. Note that, even if we just saw that in a clinical situation counting rates will be high, pile-up was not taken into account in the following simulations.

1.1 Geant4 simulations

The set-up used in the simulations is represented on Fig. 1. The phantom is a cylinder of PMMA with a 15 cm diameter and a 20 cm length. The Compton camera consists of ten silicon detectors and one LYSO absorber detector. This corresponds to one of the two setups adopted at the end of our study with a photon point source.

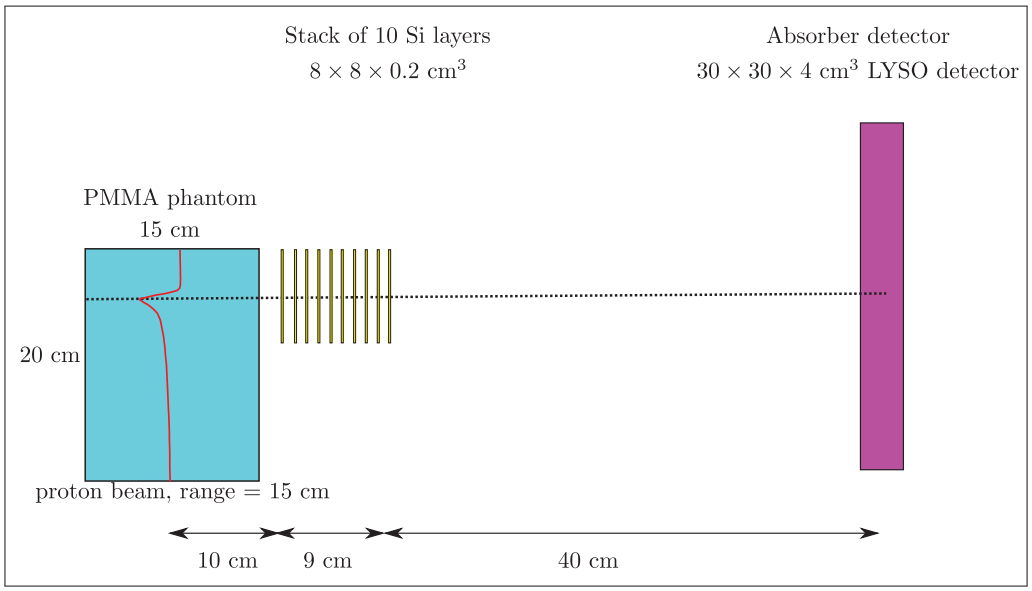

Figure 1: Set-up of the simulations

All simulations were carried out with Geant4 9.4. The physics list is the same than the one described in last chapter (including the G4Lelastic scattering model). Again, simulations were performed in two steps: a step including the interactions of the proton beam in the phantom and a step including the interactions of the secondary particles emitted during the irradiation in the Compton camera. Each time a particle coming out of the phantom interacts in one of the detectors, all information concerning this interaction (position of interaction, energy deposited, time of interaction, particle type, incident energy, ion number) is recorded. In the Geant 4 simulations, all ions are shot at $t = 0$. the time structure of the proton beam was applied afterwards. The energy and position resolutions were taken into account with Gaussian models. The value of the resolutions used are those given in Chap. I.1.

1.2 Data post-treatment

We used two different time structures for the proton beam:

- a time structure corresponding to a low current: 1 ion every 1 µs;
- a time structure corresponding to the IBA Proteus 235 cyclotron with a current of $\approx$ 1 nA, 20 ions in 3.2 ns bunches every 9.37 ns.

The time resolution of the detectors was taken into account using a Gaussian model. We considered a time resolution of 15 ns FWHM for the silicon detector and of 3 ns FWHM for the LYSO detector.

Then the idea is to reproduce the output of a realistic acquisition system. We want to obtain a list of coincidence events corresponding to one interaction in a single silicon detector and one interaction in the LYSO detector. So, for each interaction in the LYSO detector, we look for interactions in the silicon detectors that fall in a given time window. No energy window are used here. The time window is adjusted for each silicon detector (see next §). Then we select coincidence events with an interaction in only one silicon detector. Real coincidences and random coincidences are sorted out by comparing all information concerning the particle impinging on the camera that originated the interactions in the silicon and in the LYSO detector. Note that an event, where a γ ray would undergo an interaction (pair creation for instance) in one silicon detector and a secondary γ-ray (511 keV photon for instance) produced subsequently to the interaction in the silicon detector, would interact in the absorber detector, is considered as a real coincidence as, indirectly, both interactions are related to the same particle which goes out of the phantom.

In the case of ideal detectors (detectors with a perfect time measurement), the coincidence window is delimited by the minimal d_{min} and maximal d_{max} distance that can cross a photon which interacts in two detectors. d_{min} and d_{max} are given by:

$$d_{min} = d - \frac{t_1}{2} - \frac{t_2}{2}, \tag{II.2.1}$$

$$d_{max} = \sqrt{2 \times \left(\frac{w_1 + w_2}{2}\right)^2 + \left(\frac{t_1 + t_2}{2} + d\right)^2}, \tag{II.2.2}$$

where t_1 and t_2 are the thicknesses of the two detectors at stake, w_1 and w_2 their widths and d the distance between the centres of these two detectors. Two interactions in the detectors 1 and 2 are in coincidence, if the difference between the interaction times is higher than $t_{min} = \frac{d_{min}}{c}$ and lower than $t_{max} = \frac{d_{max}}{c}$, where c is the speed of light. When the time resolution of the detectors is taken into account in the simulations, t_{min} and t_{max} are adjusted. If the FWHM time resolutions of detector 1 and 2 are $\Delta_{t,1}$ and $\Delta_{t,2}$, the value of t_{min} is decreased by $0.5 \times (\Delta_{t,1} + \Delta_{t,2})$ and the value of t_{max} is increased by $0.5 \times (\Delta_{t,1} + \Delta_{t,2})$. The value of t_{min} and t_{max} is computed for each silicon detector in the case of detectors with a perfect time resolution in Table 1.

Table 1: Width of the coincidence window for each silicon detector in the case of perfect detectors.

Detector	Si 1	Si 2	Si 3	Si 4	Si 5	Si 6	Si 7	Si 8	Si 9	Si 10
t_{min}, ns	1.56	1.53	1.49	1.46	1.43	1.39	1.36	1.33	1.29	1.26
t_{max}, ns	1.92	1.89	1.86	1.83	1.80	1.77	1.75	1.72	1.69	1.66

2 Results

2.1 Proton interactions in the phantom and production of secondary particles

The dominant interaction of the incident protons is electromagnetic interaction: inelastic collisions with the atomic electrons which lead to ionisation and dose deposition, and elastic collisions with the atomic nuclei which lead to lateral deflection of the beam. The incident protons undergo also inelastic reactions with the atomic nuclei (about 20 % at 160 MeV) . Fig 2 illustrates the number of particles produced in the target per incident ion subsequently to these reactions for each particle type.

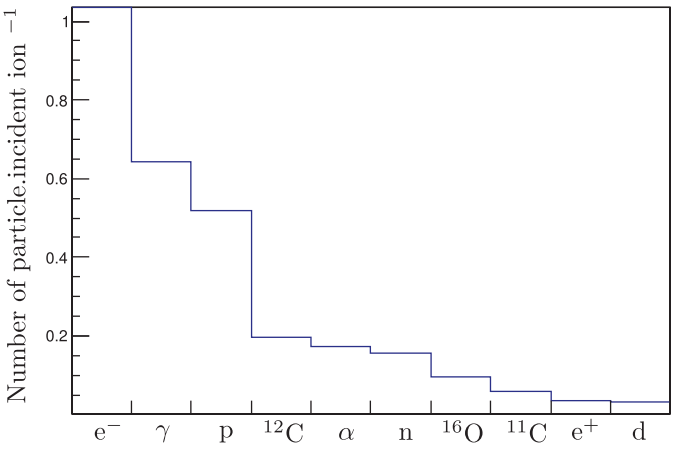

Figure 2: Particle type at emission.

As expected, mainly secondary electrons are emitted ($\approx$ 36 electrons emitted per incident proton). These electrons have an energy lower than 0.4 MeV and most of them are absorbed inside the phantom. The other particles emitted are mainly gamma rays, secondary protons, neutrons, alpha particles, deuterons, carbon and oxygen ions. Most of the charged particles are absorbed in the phantom. The particles impinging on the camera are mainly γ rays, neutrons and protons. Note that most of the secondary protons emitted during the irradiation have an energy lower than 10 MeV and thus most of them are absorbed in the phantom. The protons that exit the phantom are primary protons that undergo one elastic scattering. We saw in the previous chapter that there might be a problem with this model of interaction, so the value of the number of protons interacting in the detectors is biased and would need to be corrected by simulations with an improved model describing elastic scattering.

Mainly γ-rays and neutrons interact in the camera. The energy spectrum of these neutrons and γ rays is represented on fig. 3. Neutrons have a broad spectrum up to 140 MeV. Most of the γ-ray energy spectrum stretches over 10 MeV. The different peaks of the γ-ray energy spectrum correspond to specific nuclear de-excitations (see [Kozlovsky2002] for an identification of these peaks). Table 2 gives the number of γ-ray and neutron interactions in each detector. The neutron interactions represent about one tenth of all interactions. This means that the influence of the neutron background may be limited, in the case of proton therapy and that, here, for the Compton camera a time-of-flight selection may not be required.

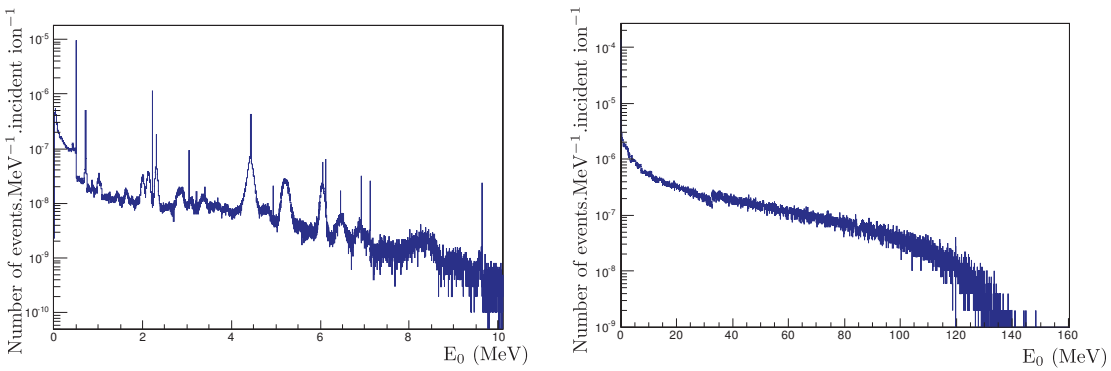

Figure 3: Energy spectrum of secondary γ rays and neutrons produced during the irradiation of the PMMA phantom defined above by a 160 MeV proton beam.

Table 2: Number of interactions per incident protons in each detector for a 160 MeV proton beam.

Detector	Total	γ ray	Neutron
Si 1	3.70×10^{-04}	3.16×10^{-04}	4.06×10^{-05}
Si 2	7.84×10^{-04}	4.58×10^{-04}	6.70×10^{-05}
Si 3	6.00×10^{-04}	3.76×10^{-04}	5.89×10^{-05}
Si 4	4.86×10^{-04}	3.17×10^{-04}	5.05×10^{-05}
Si 5	4.04×10^{-04}	2.70×10^{-04}	4.46×10^{-05}
Si 6	3.41×10^{-04}	2.31×10^{-04}	3.99×10^{-05}
Si 7	2.92×10^{-04}	2.01×10^{-04}	3.46×10^{-05}
Si 8	2.50×10^{-04}	1.75×10^{-04}	2.97×10^{-05}
Si 9	2.17×10^{-04}	1.52×10^{-04}	2.74×10^{-05}
Si 10	1.88×10^{-04}	1.33×10^{-04}	2.30×10^{-05}
LYSO	5.06×10^{-03}	4.13×10^{-03}	8.44×10^{-04}

Reconstructable events

Tables 3, 4 and 5 give the number of real coincidences and of random coincidences in several configurations. In the case of a low beam current and of perfect detectors (see Table 3), there are only 9.5 % of random coincidences. 82.4 % of the real coincidences correspond to γ-ray interactions and, 70.8 % to true events (i.e γ rays undergoing one Compton interaction in a silicon detector without energy escape and at least an interaction in the LYSO detector). This last number is consistent with the simulations with a photon point source of Chap. I.3.

In the case of perfect detectors, the influence of the beam current on the proportion of random coincidences is limited: it is 15.6 % for a beam current of 1 nA (see Table 4). Yet, when the time resolution of the detectors is taken into account, it becomes difficult to associate together the interactions in the detectors, and random coincidences become predominant (see Table 5). Indeed when taking into account the time resolutions of the detectors, the width of the coincidence window goes from approximately 0.4 ns to 20 ns. The consequences of these random coincidences on the reconstructed profile are illustrated in the next §.

Fig. 4 shows the 2D distribution of the energy deposited in the scatter detector and in the absorber detector for all events, for real coincidences and for random coincidences. Fundamentally, all these events correspond to the same interactions in the detectors. In the case of too slow detectors, or of too high counting rates, it becomes more and more difficult to associate correctly the interactions in the absorber detector with the one in the scatter detector. That is why the 2D energy distribution corresponding to random coincidences

is very similar to the one corresponding to real coincidences. So it is not possible to distinguish these events by using appropriate energy thresholds.

Table 3: Reconstructable events (1 ion/µs, perfect detectors).

Real coincidences			Random coincidences
γ		other particles	all particles
true events	other sequences		
70.8 %	11.6 %	8.1 %	9.5 %
6.55×10^{-05}	1.07×10^{-05}	7.49×10^{-06}	8.79×10^{-06}

Table 4: Reconstructable events (IBA time structure, perfect detectors).

Real coincidences			Random coincidences
γ		other particles	all particles
true events	other sequences		
66.3 %	11.4 %	6.7 %	15.6 %
6.8×10^{-05}	1.2×10^{-05}	6.9×10^{-06}	1.6×10^{-05}

Table 5: Reconstructable events (IBA time structure, realistic detectors).

Real coincidences			Random coincidences
γ		other particles	all particles
true events	other sequences		
12.3 %	4.3 %	4.1 %	79.3 %
3.1×10^{-05}	1.1×10^{-05}	1.0×10^{-05}	1.9×10^{-04}

2.2 Reconstruction of the γ-ray profile

Fig. 5 shows the emission profile (i.e. the distribution of the longitudinal coordinates of the emission point inside the target) in the case of a beam with the IBA time structure and of detectors with realistic energy, position and time resolutions. The blue profile represents the reconstruction of all the coincidence events, the green profile the reconstruction of real coincidences and the red profile the reconstruction of random coincidences. In the case of random coincidences, the emission position of the particle interacting in the scatter detector is plotted. The dose profile is also plotted to indicate the Bragg peak position. As expected, we observe a sharp fall-off at the Bragg peak position. Fig. 6 shows the reconstructed profiles. The profile were reconstructed by intersecting, for each event, the Compton cone with the ion trajectory (here the y axis) with the algorithm described in Chap. I.1. The total profile exhibits a fall-off at the expected Bragg peak position, yet the contrast is very low compared to the contrast at the fall off of the emission profile. Because the contrast at the fall-off for the real-coincidence profile is also poor, the predominance of random coincidences over real coincidences cannot alone explain this low contrast.

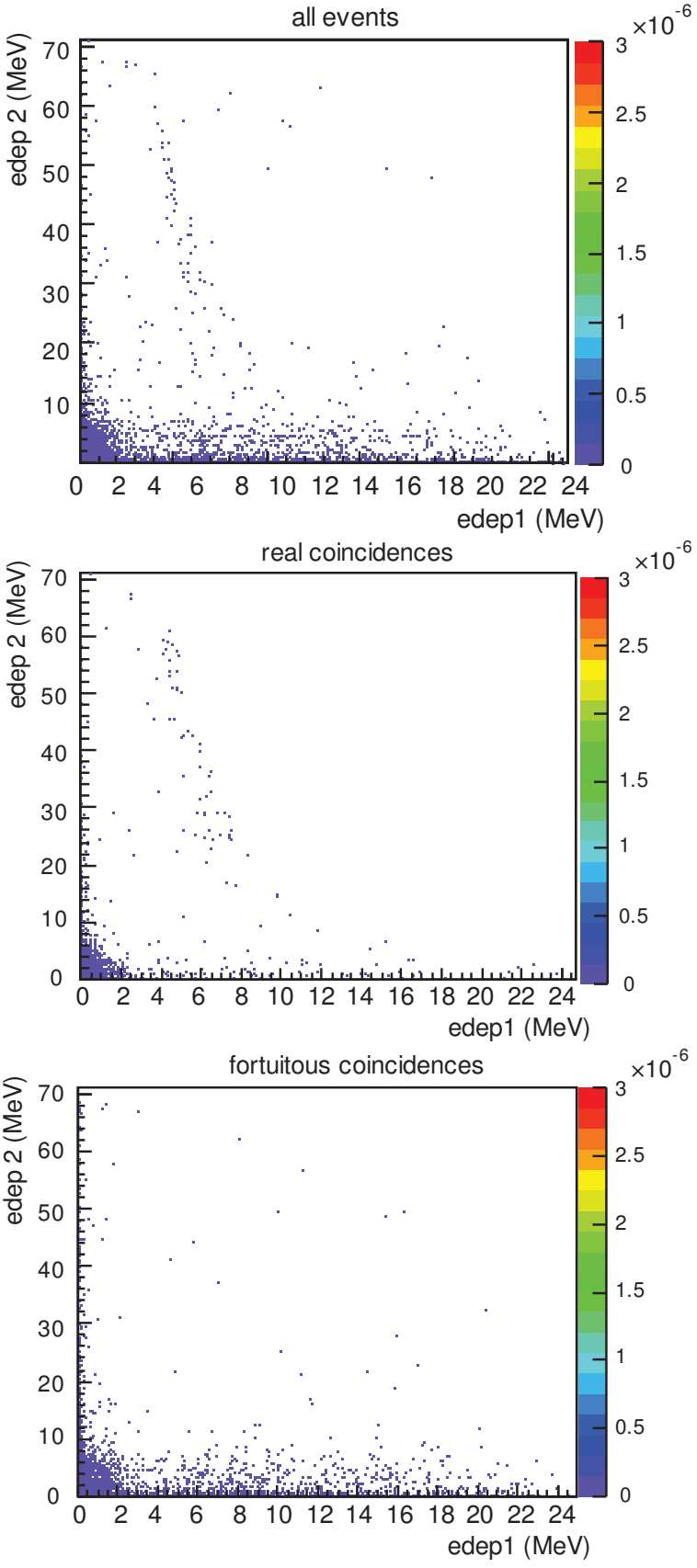

Figure 4: Energy deposited in the detectors for the coincidence events (IBA time structure, realistic detectors). edep1 is the energy deposited in the silicon detector and edep2 the energy deposited in the absorber detector.

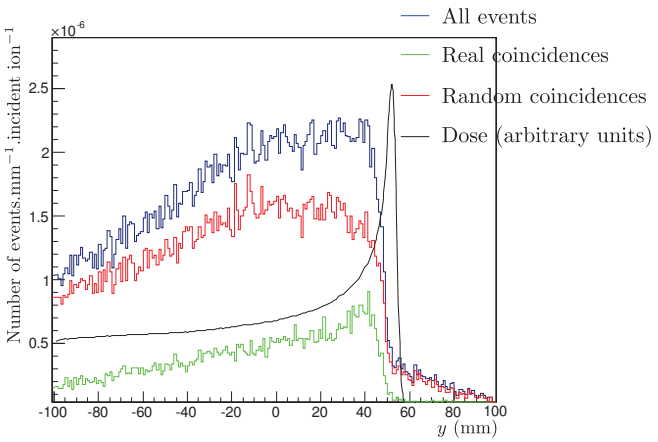

Figure 5: Emission profile for the irradiation of the PMMA target by 2×10^8 incident protons of 160 MeV.

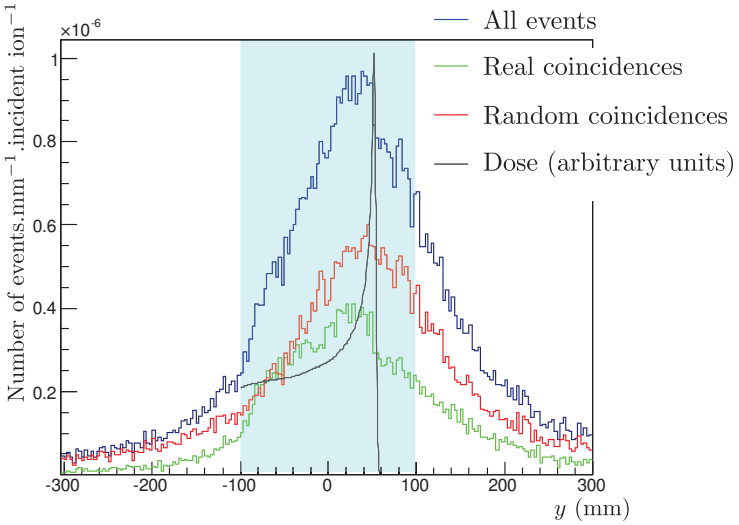

Figure 6: Reconstructed profile in the case of a beam with the IBA time structure and of detectors with realistic energy, position and time resolution. 2×10^8 incident protons at 160 MeV were shot. The position of the target is indicated by a light blue background.

In fact, the reconstruction algorithm is at stake here. For each event, reconstruction consists in a line-cone intersection. In most of the cases, such an intersection gives two solutions: one is more or less close to the real solution depending on the detector resolutions and an other adds noise on the reconstructed image. Fig. 7 compares the profile reconstructed with all the intersection solutions and the reconstructed profile, when artificially keeping only the solution which is the closest to the real emission point. The contrast is greatly improved, even if mainly random coincidence events are reconstructed. Of course this selection is not feasible experimentally, but this points out the limits of our reconstruction algorithm. The profile could also be improved by defining an appropriate energy threshold in order to eliminate all the Compton scattered γ rays, and by time-of-flight selection, but in any case, the limiting factor is the reconstruction algorithm. To circumvent this problem, a more advanced algorithm, MLEM-like, is thus requested.

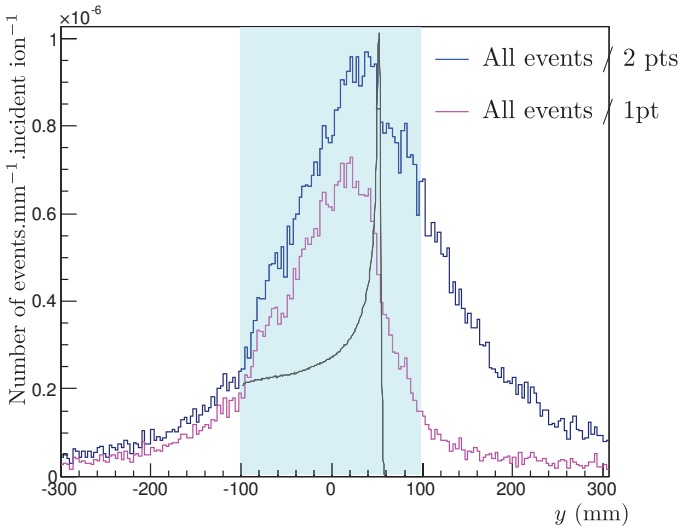

Figure 7: Comparison of the reconstructed profile with all the solutions of the line-cone intersection (dark blue) and with the closest solution to the real emission point (magenta). 2×10^8 incident protons were shot. The position of the target is indicated by a light blue background.

2.3 Precision of the Bragg peak position

The next step of this study is to evaluate the ability of the camera to detect shifts of the proton beam range in the target. This would need a set of simulations with shifts of the target position or deviations in the beam incident energy. Here we propose a method requiring less computing time which consists in applying directly a shift on the reconstructed data. The two methods will give similar results provided the shift is applied on data corrected by the detection efficiency and provided the shift is small compared with the detector dimensions.

Fig. 8 shows the variations of the detection efficiency, when a photon point source is moved away from the centre of the field of view along the incident proton path. The red curve represents a Gaussian fit of this graph. To correct data by the detection efficiency, before filling the histogram containing the reconstructed profile, each event was weighted by the inverse of the detection efficiency value at this position instead of being weighted by 1. Note that the camera was positioned in front of the Bragg peak, at y = 50 mm. The reconstructed profile (without any shift) corrected by the detection efficiency for 10^{10} incident protons is represented on Fig. 9. In this paragraph, for each event, all solutions of the line-cone intersection are kept. This profile can be fitted by three straight lines. The same function was used to fit similar profiles, with or without shifts, corresponding to 2×10^8 incident protons. This number of incident protons was chosen because it is typically the number of ions used in a pencil beam of a clinical treatment plan (see [Smeets2012] for an example of treatment plan). During this fit, the only degree of freedom was a possible horizontal shift, all the coefficients of the three straight lines were fixed by the fit on the high statistics profile. This operation was carried out on a set of 50 different simulations. Fig. 10 shows one of these 50 profiles.

Fig. 11 shows the distribution of the shift retrieved from the fit for 50 reconstructed profiles corresponding to 2×10^8 incident protons. The mean of this distribution is expected to be the value of the applied shift and the standard deviations indicates the accuracy of the determination of the Bragg peak position. Table 6 gives the mean and standard deviations of the distributions of the retrieved shifts, corresponding to actual shifts of 0 mm, 0.9 mm, 1.9 mm and 2.9 mm. Each time, the mean is very close to the applied shift, the difference is lower than 0.3 mm. This method appears to be really robust and even with profiles with poor statistics. The standard deviation is of the order of 2.5 mm. This means that in 95 % of the cases, this method is capable to detect a shift of 5 mm. Such a value seems too high for a clinical application, but we expect to improve it significantly with an iterative reconstruction algorithm. Systematic simulations with an

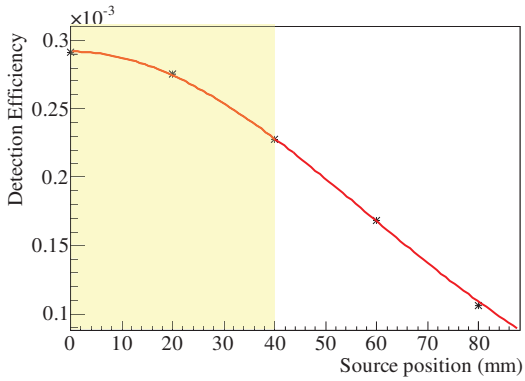

Figure 8: Influence of the position of the source in the field of view of the camera on the detection efficiency. The position of the camera is indicated by a yellow background. The distance between the source and the camera is 10 cm.

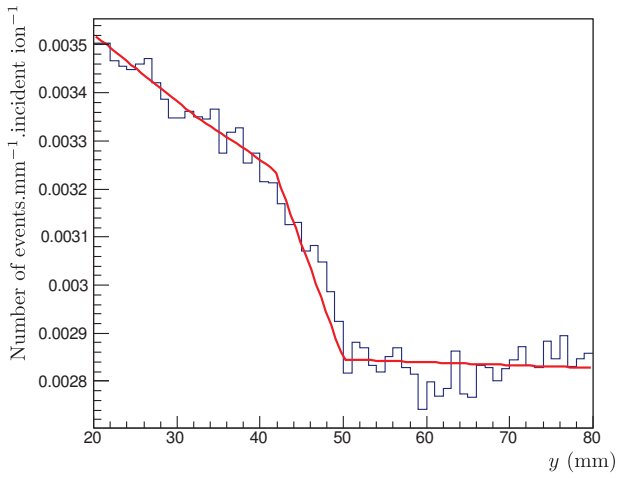

Figure 9: Zoom on the reconstructed profile around the Bragg peak position corrected by the detection efficiency. The profile corresponds to 10^{10} incident 160 MeV protons. The red curve represents the fit function.

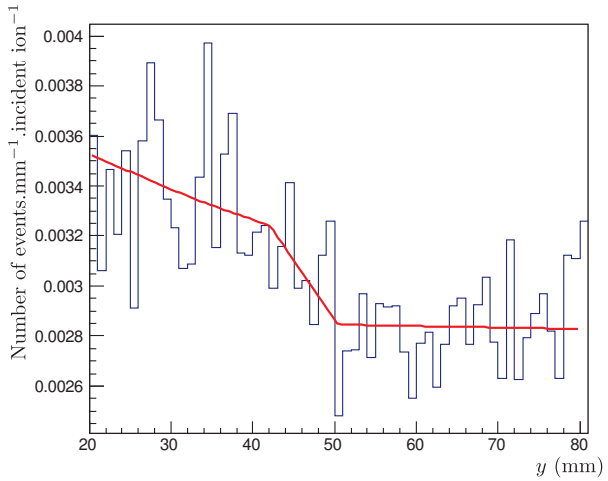

Figure 10: Zoom on the reconstructed profile around the Bragg peak position corrected by the detection efficiency. The profile corresponds to 2×10^8 incident protons. The red curve represents the fit function.

actual shift of the target are needed to confirm this point.

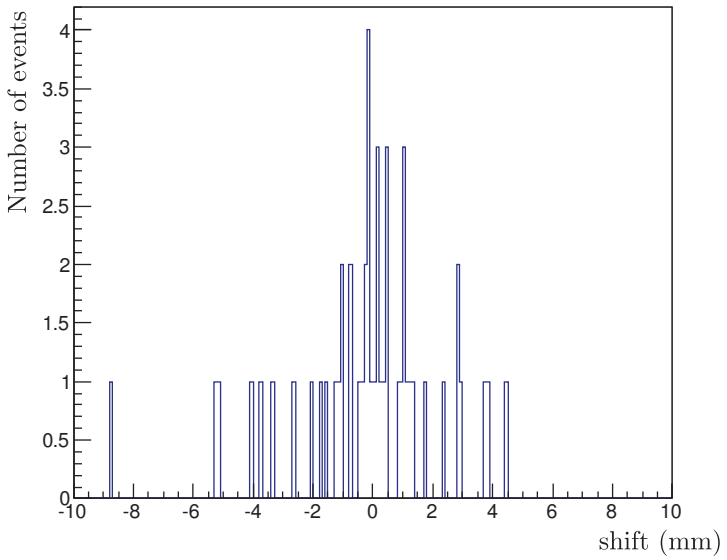

Figure 11: Distribution of the shifts retrieved from the fit on 50 profiles, each one corresponding to 2×10^8 incident protons. The mean of this distribution is -0.19 mm and the standard deviation 2.39 mm. In this case no shift was actually applied on the reconstructed profiles.

Table 6: Mean and standard distribution of the distributions of the shifts retrieved from the fit of 50 profiles.

Applied shift, mm	0.0	0.9	1.9	2.9
Mean, mm	-0.19	0.7	1.6	2.6
Standard deviation, mm	2.39	2.2	2.5	2.1

Conclusion and perspectives

A detection system combining a beam hodoscope and a Compton camera is a possible solution for in beam monitoring during ion beam therapy. The Compton camera is used to reconstruct the distribution of the emission position of the prompt γ rays emitted subsequently to the nuclear reactions. Indeed this distribution is highly correlated to the dose distribution. The beam hodoscope is used to tag the incident ions both temporally and spatially. The time information provided by the hodoscope can be used to perform a time-of-flight selection among the interactions occurring in the absorber detector of the camera. This is particularly important in carbon therapy where an important neutron background is present. The position information provided by the hodoscope can be used to simplify the reconstruction of the Compton camera. Indeed if we assume that ion lateral straggling is negligible, that the fragmentations occur along the ion trajectory and that the hodoscope is infinitely precise, it is possible to reconstruct each event independently by reducing the reconstruction problem to the intersection between a straight line given by the hodoscope and a cone, whereas with a classical Compton camera several cones are needed to reconstruct the source positions. Any deviation from these assumptions would translate into a parallax error. As the γ-rays enter the camera at small angles with respect to the transverse plane it seems reasonable not to consider this error.

The goal of my thesis was to perform a preliminary study of such a detection system with a particular focus on the Compton camera. For this purpose, I developed a tool relying on Monte Carlo simulations (carried out with Geant4). It makes it possible to study the response of a Compton camera in several cases: in the case of a photon point source and in the case of the irradiation of an homogeneous phantom by an ion beam.

In the first part, the double scattering Compton camera and single scattering Compton camera have been studied in details by means of Geant4 simulations. We demonstrated that the use of a multiple scattering Compton camera is not mandatory and that even if the incident energy of the γ rays that we want to image is pretty high (approximately up to 10 MeV), most of them are fully absorbed within a few centimetres of detector. As a consequence, the use of a single scattering camera is preferable in order to get a detection efficiency as high as possible.

Our criteria when choosing the detector materials were the probability of interaction and the energy, position and time resolutions. For the scatter detector, low Doppler broadening and a high percentage of Compton interactions were also required. A silicon scatter detector meets all these requirements. For the absorber detector, we demonstrated that a high photoelectric cross-section is needed to maximise the percentage of fully absorbed γ rays. A LYSO or a BGO absorber detector are two possible solutions. Yet the intrinsic radioactivity of lutetium and the bad timing properties of BGO may be problematic. That's why we will use both absorber detectors for the tests of our prototype.

The geometry of the camera was fixed after a study of the influence of the different parameters on the performances of the camera. We chose to use a stack of thin detectors instead of a thick detector as scatter detector in order to facilitate the identification of events which correspond to undesired interaction sequences (for instance events corresponding to interactions in the absorber detector of the Compton electrons). $8 \times 8 \times 0.2$ cm^3 is a standard size of silicon strip detector provided by the supplier we chose. As many silicon layers as possible should be used to improve the camera efficiency and resolution knowing that after twenty layers no important improvement is observed. To begin with we decided to use ten layers.

A pyramid shaped camera is necessary to maximise the detection efficiency and a width of 30 cm for the absorber detector was selected. Yet for the test of our prototype, 10×10 cm^2 detectors will be bought, mainly to limit the cost of this prototype. The thickness of the absorber detector should be high enough to provide a high probability of full absorption for the scattered photons but not too high in order to limit the parallax error due to the fact that no depth-of-interaction measurement is planned. Indeed, we showed that for absorber detector with a thickness of a few centimetres, no improvement of the spatial resolution are to be observed if the depth-of-interaction measurement is implemented.

The final architecture is presented on Fig. 1. This setup provides a detection efficiency of 3×10^{-4} reconstructable events per incident photon emitted in 4 π and and a spatial resolution of 7 mm FWHM.

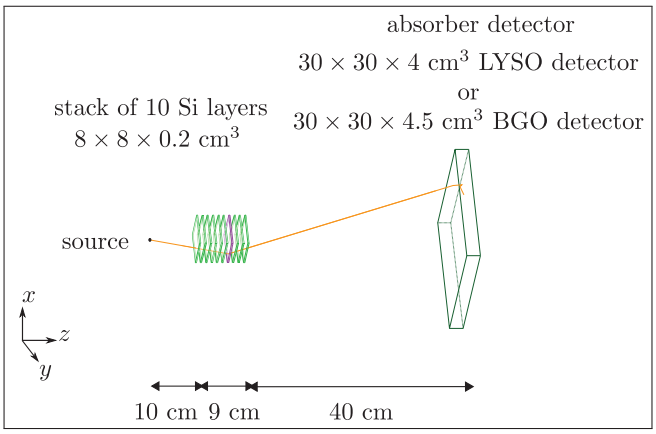

Figure 1: Final configuration of the Compton camera

In the second part, we studied the response of the camera to the irradiation of a PMMA phantom by an ion beam. In beam tests were carried out at the Heidelberg Ion Therapy Centre with small size detectors. It made it possible to measure the count rates expected in a clinical situation for the full size camera. Especially in the case of proton therapy, these count rates will be pretty high. Such high count rates will cause pile-up effects in the detectors, this may degrade dramatically the quality of the reconstructed images. The predominance of random coincidences over real coincidences is also related to these high count rates. As a consequence, suitable solutions needs to be developed to overcome these problems. A possibility would be to reduce the solid angle by increasing the source to camera distance and/or by decreasing the size of the detectors. Several small cameras could be used also instead of a single large camera.

The experimental results were reproduced by means of Geant4 simulations. On the whole, the agreement between simulations and measurements is satisfactory. The limits of the G4LElastic model, which describes hadron elastic scattering, were underlined. Some discrepancy that was attributed to prompt γ-ray production was also observed. This means that the current studies on the improvement of the hadronic models implemented in Geant4 and more generally in Monte Carlo simulation softwares need to be continued.

We also underlined a limit of the line-cone intersection reconstruction algorithm: the poor contrast when reconstructing the distribution of an extended source. Indeed, the source position is reconstructed independently for each events by intersection the Compton cone and the hodoscope line. Such intersections may return two solutions. And as it is not possible to determine which one is the correct solution, both are kept and the second solution generates noise in the reconstructed image. With a standard MLEM reconstruction algorithm, the source distribution is reconstructed by intersecting all the Compton cones together. Some of the cone intersections do not correspond to an actual source position. These points are eliminated by the iteration process. A MLEM algorithm taking into account the information provided by the beam hodoscope is necessary. This algorithm should be as fast as possible in order to be compatible with real time monitoring.

In the last chapter, we evaluated the achievable precision on the Bragg peak position in the case of a 160 MeV proton beam in a PMMA target. In the current configuration, a deviation higher than 5 mm in the beam range is detectable with the Compton camera. This value is expected to be improved, among other things by using a more appropriate reconstruction algorithm. In any cases, a complete simulation study, including the simulation of realistic treatment plans with CT scans as targets, is necessary to assess precisely which deviation a Compton camera is likely to detect during a treatment. Tools similar to the γ index, which is currently used for quality control in intensity modulated radiotherapy, need to be implemented.

In the first part we tried to maximise the detection efficiency to increase as much as possible the number of reconstructable events per incident ion. Even with a detection efficiency of 3×10^{-4} reconstructable events per photon emitted in 4π, reconstructing the prompt γ-ray distribution after the irradiation of each raster position seems challenging, especially in the case of carbon therapy. Yet, if the detection efficiency is too high, the high counting rates in the detectors cause pile-up and random coincidences. A trade-off has to be found.

As already mentioned, a Compton camera prototype is currently built in IPNL. This work made it

possible to choose the dimensions and materials of the detectors of the camera. The silicon detectors were delivered this spring and are currently under bonding and mounting. In parallel with this study, ASIC chips were designed and constructed in the electronics department in order to read-out the silicon detectors. Two scintillator detectors have been ordered and are expected to be delivered this winter. Two hodoscope prototypes made of scintillating fibres of 1×1 mm^2 have been developed and are currently tested. They consist of 2x32 and 2x128 fibres. One of the prototypes is read-out by PMs and the other by MCP-PMTs. The first step will be to characterise our detectors in terms of efficiency, and of position, energy and time resolution, and then to study their response to both photon and ion sources. Finally in beam tests with the entire detection system (Compton camera and beam hodscope) are planned.

All this work is part of a more global work of our group concerning the study of modalities for in beam monitoring in ion beam therapy. Several prototypes are under construction in IPNL: the already mentioned Compton camera prototype, a prototype of a multi-slit collimated detector and a prototype for interaction vertex imaging. All three prototypes will be used in combination with the beam hodoscope. The final goal of these developments is to determine the assets and the drawbacks of each detection system, to compare them and finally to propose a system suitable for a clinical application. With that in view, the Compton camera performances and the technological choices we made will also be compared with those of the other Compton camera that are developed for ion beam therapy, and in particular within the ENVISION project.

The applicability of the developed Compton camera to nuclear medicine was also envisaged. The simulated performances (detection efficiency and angular resolution) are comparable to the performances of the state-of-the-art gamma-cameras, such an application is worth investigating further. As in this case the incident energy of the photons is unique and known, the Compton camera design needs to be re-optimised.

APPENDIX

Applicability to nuclear medicine

1 Introduction

Compton cameras are also developed for applications in nuclear medicine for either clinical or preclinical (i.e. small animal) imaging [Uche2012] [Rossi2011] [Yamaguchi2011]. Table 1 gives the specification of state-of-the-art SPECT imagers [Jansen2007]. To be competitive with the current SPECT technology, a spatial resolution better than 1 mm and a detection efficiency of the order of 0.1 % for preclinical applications and a spatial resolution better than 1 cm and a detection efficiency of the order of 10^{-5} for clinical applications must be achieved. Since the first proposal of [Todd1974], there has been lots of research to use Compton cameras in the field of nuclear medicine, but detectors available at that time prevented the construction of a Compton camera which could compete with traditional systems. With the recent development of detectors with much improved spatial and energy resolutions, there has been a renewal of interest with several groups actively working on various aspects of this mode of imaging.

Table 1: State-of-the-art SPECT specifications

	Clinical SPECT	Preclinical SPECT
Sensitivity	0.01 % - 0.03 %	0.3 %
Resolution	10 mm	1.2 mm (even $<$ mm)
FOV	50 cm	8 cm

The radio-isotopes currently used in nuclear medicine emit γ rays with an energy of the order of a few hundreds of keV. This implies that the incident energy of the detected photons is known. Thus the reconstruction can be limited to the events depositing a total energy in the camera that falls in an energy window around the theoretical value, the length of the window being fixed by the detector energy resolutions. Moreover, as the energies at stake are significantly lower than the energies of the prompt γ-rays, the current design of the camera might not be optimum here. The inter-detector distances and the detector sizes would need to be optimised in these conditions. This was not the scope of my thesis. The idea of this study is just to compare the performances of our Compton camera with the state-of-the-art imagers to assess wether or not it is worth investigating further an application of our camera in the field of nuclear medicine.

2 Methods

2.1 Simulations

We adapted the simulations used to study the applicability of Compton cameras to prompt γ-ray imaging: the geometry of the camera was the same but the distance between the source and the camera was set to 5 cm instead of 10 cm to fit with a preclinical application (see Fig. 1). Because the optimisation of the absorber detector is highly dependent on the photon incident energy, it is no more valid for an application in nuclear medicine. That is why the geometry of the Compton camera correspond to the geometry before the optimisation of the absorber detector.

The simulations were performed with Geant4 9.2. We followed the exact same methodology as the one described in Chap. I.1 § 2. The detector resolutions are reminded in Table. 2. I simulated monoenergetic photon point sources of 300 keV, 511 keV and 1 MeV to cover the energy range of the radio-isotopes currently used in nuclear medicine and of potential high energy isotopes.

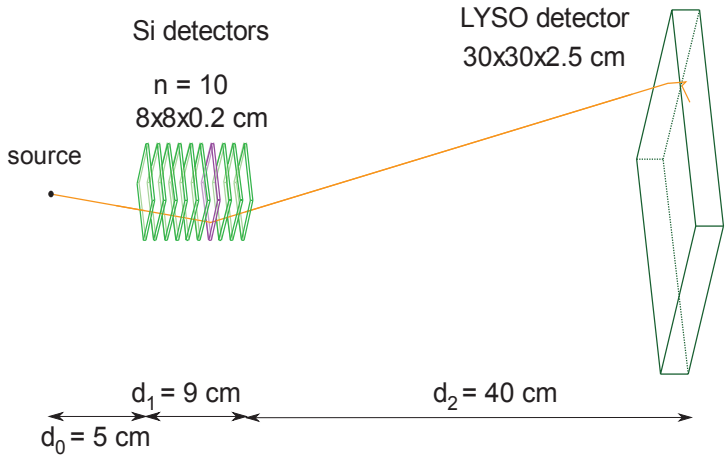

Figure 1: Simulated set-up.

Table 2: Detector resolutions

	Lateral FWHM	In-depth FWHM	Energy FWHM
Si	1 mm	no information	2 keV
LYSO	5 mm	no information	8.3 % @ 1 MeV

2.2 Reconstruction

In the simulations, I select events corresponding to energy deposit in only one detector of the stack and energy deposit in the LYSO detector. Only events which correspond to a total energy deposit in the camera equal to the photon incident energy $\pm$ 10% are reconstructed. Each cone is reconstructed as before: its apex is the interaction position in the scatter detector, its axis is the direction between the two interaction positions and its aperture angle ϑ is defined by the Compton equation:

$$\cos\vartheta = 1 - 0.511\left(\frac{1}{E_0 - edep_1} - \frac{1}{E_0}\right) \tag{3}$$

where E_0 is known exactly and $edep_1$ is the energy deposited in the silicon detector. As the incident energy of the photons is known, the value of the energy deposited in the absorber detector does not intervene in the calculation of the cone aperture angle. This value is only needed to select events corresponding to a full absorption in the absorber detector and improve the spatial resolution of the camera.

Here, as we have no prior information about the source position, our previous reconstruction algorithm (line-cone interaction) cannot be used. The source position must be reconstructed by intersecting the different cones corresponding to the photons that have interacted in the camera. In this study we did not reconstructed the source position. We only evaluated the angular precision of the camera by defining for each reconstructed event $\vartheta_{\text{diff}} = \vartheta_{\text{true}} - \vartheta_{\text{reconstructed}}$, where ϑ_{true} is the exact value of the Compton angle and $\vartheta_{\text{reconstructed}}$ the value calculated from Eq. 3.

3 Results

Table. 3 gives the detection efficiency of the camera for photon incident energies between 300 keV and 1 MeV. Figure 2 represents the distribution of ϑ_{diff} at 300 keV, 511 keV and 1 MeV. The FWHM of each

distribution is given above the figure. In the energy range considered, the detection efficiency is around 0.1 % and does not vary much with the photon incident energy. The angular resolution decreases from 3.2 degree @ 300 keV to 0.6 degree @ 1 MeV mainly because at high energy Doppler broadening is less important. Compared to the value given in Table. 1 and the values found in literature, where values of angular resolutions of the order of a few degrees are reported (see for instance [Uche2012], [Seo2010] or [Kurosawa2010]), our results seems very promising.

Table 3: Influence of the photon incident energy on the detection efficiency

E_0	300 keV	511 keV	1 MeV
Detection efficiency	0.05 %	0.1 %	0.09 %

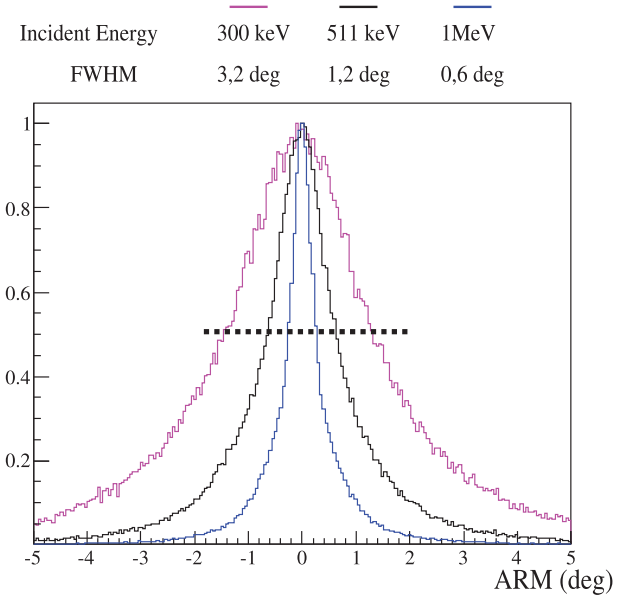

Figure 2: Influence of the photon incident energy on the angular resolution

4 Perspectives

The detection efficiency and angular resolution can be further improved by optimising the geometry of the camera for this particular application. Moreover the achievable spatial resolution need to be assessed by using a reconstruction algorithm similar to the one developed by our collaborators in CREATIS. This is the subject of future studies involving a PhD thesis at IPNL.

Design Study of the Absorber Detector of a Compton Camera for On-line Control in Ion Beam Therapy

M.-H. Richard, M. Dahoumane, D. Dauvergne, M. De Rydt, G. Dedes, N. Freud, J. Krimmer, J.M. Létang, X. Lojacono, V. Maxim, G. Montarou, C. Ray, F. Roellinghoff, E. Testa, A.H. Walenta

***Abstract*—The goal of this study is to tune the design of the absorber detector of a Compton camera for prompt γ-ray imaging during ion beam therapy. The response of the Compton camera to a photon point source with a realistic energy spectrum (corresponding to the prompt γ-ray spectrum emitted during the carbon irradiation of a water phantom) is studied by means of Geant4 simulations. Our Compton camera consists of a stack of 2 mm thick silicon strip detectors as a scatter detector and of a scintillator plate as an absorber detector. Four scintillators are considered: LYSO, NaI, $LaBr_3$ and BGO. LYSO and BGO appear as the most suitable materials, due to their high photo-electric cross-sections, which leads to a high percentage of fully absorbed photons. Depth-of-interaction measurements are shown to have limited influence on the spatial resolution of the camera. In our case, the thickness which gives the best compromise between a high percentage of photons that are fully absorbed and a low parallax error is about 4 cm for the LYSO detector and 4.5 cm for the BGO detector. The influence of the width of the absorber detector on the spatial resolution is not very pronounced as long as it is lower than 30 cm.**

***Index Terms*—Compton camera, hadrontherapy, ion beam therapy, prompt gamma ray, Geant4, $LaBr_3$, NaI, LYSO, BGO**

I. Introduction

In ion beam therapy, the finite range of the particles makes the irradiation more sensitive than a photon irradiation to any deviation of parameters such as patient positioning, patient and tumour morphology and treatment planning errors. In particular, the calibration between the computed tomography (CT) scanner images and the ion energy loss rates during the elaboration of the treatment plan can lead to an uncertainty of up to 3% on the ion ranges [1]. Real time monitoring seems necessary to detect such deviations as soon as possible during the irradiation.

We investigate here a monitoring technique based on the detection of the prompt γ-rays emitted almost instantaneously (within time well below the ns range) subsequently to nuclear fragmentation. The correlation between the prompt γ-ray profile and the dose distribution has been verified experimentally for both proton and carbon ion beams ([2], [3], [4]) with a collimated set-up. In a clinical situation, the number of prompt γ-rays is limited by the dose delivered during each fraction of the treatment. Thus it is critical to have a camera with a detection efficiency as high as possible. A Compton camera which uses electronic collimation and not mechanical collimation is likely to provide a significantly higher detection efficiency. This solution is being investigated by several teams ([5], [6], [7], [8]).

Our detection system combines a beam hodoscope with a Compton camera. The role of the hodoscope is double. First, it tags the lateral position of the ions, which reduces the reconstruction of the prompt γ-ray emission points to a simple line-cone intersection problem (see II for more details). Second, time-of-flight measurements between the hodoscope and the absorber detector of the Compton camera are used to discriminate the prompt γ-rays from the neutrons (also produced during nuclear reactions) which interact in the detector. We have already discussed the feasibility of ion beam monitoring with such a system ([9], [10]): the Compton camera response was studied there in simple conditions (a photon point source in air, and a typical prompt γ-ray spectrum) by means of Geant4 simulations, and a first optimisation of the geometry was carried out.

The aim of this paper is to optimise further the performances of the prototype under development both in terms of spatial resolution and detection efficiency. The main issue here is to tune the design of the absorber detector. Previous studies were oriented toward the optimisation of the overall camera geometry with a particular focus on the scatter detector concept (single or double scattering, use of a stack instead of thick detectors). An important aspect that has not been investigated so far concerns the influence of the design parameters of the absorber detector on both the efficiency and the spatial resolution of the Compton camera. This issue is not at all trivial in the context of prompt-γ monitoring of ion beam therapy, because the energy spectrum of the γ-rays is very broad (typically 1–10 MeV), and thus efficient γ detection requires very large absorption lengths. This paper gives an insight into this issue by means of Monte Carlo simulations in a point source configuration.

LYSO, $LaBr_3$, BGO and NaI are considered as potential absorber materials for our prototype. LYSO is considered

Preprint.

M.-H. Richard, M. Dahoumane, D. Dauvergne, M. De Rydt, G. Dedes, J. Krimmer, C. Ray, E. Testa, A.H. Walenta are with Université de Lyon, F-69622 Lyon, France; Université Lyon 1 ; CNRS/IN2P3, UMR 5822, IPNL, F-69622 Villeurbanne, France (corresponding author, e-mail: m-h.richard@ipnl.in2p3.fr)

N. Freud, J.M. Létang, X. Lojacono, V. Maxim, M.-H. Richard, F. Roellinghoff are with Université de Lyon, CREATIS; CNRS UMR 5220; INSERM U1044; INSA-Lyon; Université Lyon1; Centre Léon Bérard, France

G. Montarou is with Université de Clermont-Ferrand and CNRS/IN2P3, UMR 6533, LPC Clermont, F-63177 Aubière Cedex, France

M. De Rydt is with Instituut voor Kern-en Stralingsfysica, K.U.Leuven, Celestijnenlaan 200D, B-3001 Leuven

because of its high absorption efficiency and its timing properties below 1 ns which are good enough for time-of-flight measurements. $LaBr_3$ provides very good timing and energy resolutions. As for BGO, it offers a high photo-electric cross section and thus a high rate of total photon energy absorption and no intrinsic radioactivity unlike LYSO. Finally NaI is envisaged as a cheap alternative to the other scintillators. First the absorber detector dimensions are optimised for each material. Then we compare the four material performances. Finally the impact of the absorber's energy and spatial resolution is studied.

II. The detection system

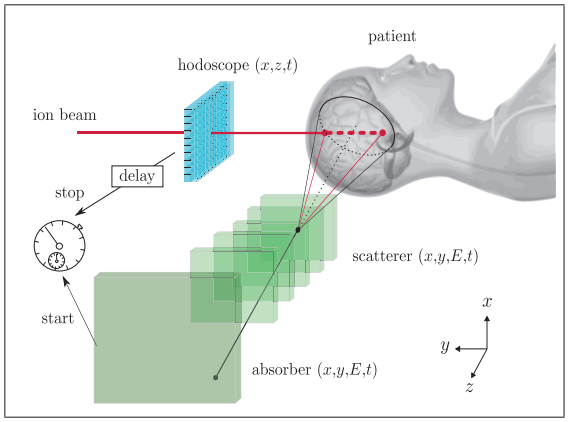

Fig. 1. Configuration of the monitoring system: the prompt γ-ray emission points are reconstructed by intersecting the ion trajectory and the Compton cone. The ion trajectory is obtained with the hodoscope and the Compton cone is reconstructed with the camera. Time-of-flight measurements between the absorber detector and the beam hodoscope (with an appropriate delay) are performed. Adapted from [10].

Fig. 1 illustrates the principle of our monitoring system including a beam hodoscope and a Compton camera. The hodoscope tags the incident ions and the Compton camera detects the prompt γ-rays emitted subsequently to the nuclear fragmentations resulting from the ion interactions in the patient. The prompt γ-ray emission points are reconstructed by intersecting the ion trajectory, given by the hodoscope and the Compton cone, reconstructed with the camera. The precision of the reconstruction is limited by the detector resolutions, Doppler broadening and by ion lateral straggling.

Our Compton camera consists of a stack of silicon chips and a thick scintillator. All detectors measure both position and energy. Ideally, the incident photon of energy E_0 scatters in one layer of the stack, the Compton electron deposits all its energy in the same layer and then the scattered photon of energy E_1 is fully absorbed in the scintillator. The scattering angle ϑ is calculated from the Compton equation.

$$\cos(\vartheta) = 1 - m_e c^2 \left(1/E_1 - 1/E_0\right) \qquad (1)$$

This makes it possible to reconstruct a cone containing the trajectory of the incident photon. The aperture half angle of the cone is ϑ, its apex is the interaction location in the silicon layer in which the photon interacted and its axis is the direction between the two interaction points. E_0 and E_1 are deduced from the deposited energies, assuming that the scattered photon has deposited all its energy in the absorber detector. The validity of this hypothesis was investigated in [10], where it was shown that for a 2.5 cm thick LYSO absorber detector the probability of total absorption is 72%.

It can happen with a probability of approximately 45% in the configuration presented in Fig. 2 that the Compton electron does not deposit all its energy in one silicon layer. Pair creation may also occur in silicon. In both cases, secondary charged particles often interact in the neighbouring silicon layers and in the absorber detector. For this reason, it is necessary to reconstruct only events in which energy is deposited in one layer of the stack.

III. The simulated set-up

We study here the camera response to a polyenergetic photon point source in air by means of Monte Carlo simulations performed with Geant4 [11]. Fig. 2 illustrates the geometrical configuration adopted after our previous studies. We use a simulated prompt γ-ray spectrum obtained when a water phantom is irradiated by carbon ions at 310 MeV/u [9].

In all simulations, the coordinates of the source in the transverse plane ($\boldsymbol{(x, z)}$ on Fig. 2) were supposed to be known exactly. In a realistic set-up with an ion beam, this would be equivalent to assuming that ion lateral straggling is negligible, that the fragmentations occur along the ion trajectory and that the hodoscope is infinitely precise. Any deviation from these assumptions would translate into a parallax error. As the γ-rays enter the camera at small angles with respect to the transverse plane it seems reasonable to neglect this error.

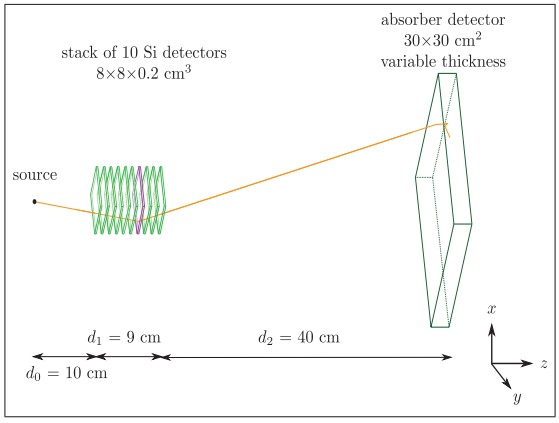

Fig. 2. Simulated set-up: the response of the camera to a photon point source in air is studied. The source is located at the centre of the camera field of view at a distance d_0 from the camera, d_1 and d_2 are the inter-detector distances. Adapted from [10].

A. The physics list

All simulations were carried out using Geant4 9.4. The G4LivermorePolarizedComptonModel process was used in order to model Compton scattering accurately, i.e. taking into account Doppler broadening and polarisation. For the other interaction processes, the standard electromagnetic processes of Geant4 were used. The implementation of these processes

has been validated by several studies and good agreement with external reference libraries was found (see for instance [12]).

B. The detectors

The scatter detector will consist of a stack of ten $8\times8\times0.2$ cm^3 double-sided strip silicon detectors. We intend to measure the lateral interaction location with a full width at half maximum (FWHM) resolution of approximately 1 mm in the strip silicon detectors. No measurement of the depth of interaction is planned. The expected equivalent noise charge (i.e. the rms fluctuation of the read out noise expressed in number of electrons) is 600 and the energy resolution of the silicon detectors is calculated with the Fano formula:

$$\Delta E_{FWHM} = 2.355w\sqrt{N_{\mathrm{ENC}}^2 + \frac{FE}{w}} \qquad (2)$$

where w=3.65 eV is the pair creation energy in silicon, N_{ENC} the equivalent noise charge, F=0.115 the Fano factor and E the energy deposited in silicon.

The scintillator detector will be read out by photomultiplier tubes using Anger logic, and the lateral position resolution is expected to be of the order of 5 mm [13]. Again no measurement of the depth of interaction is planned. This choice is discussed in IV-D. According to [14], [7], [15] and [16] the FWHM energy resolutions, for 1 MeV deposited respectively in LYSO, $LaBr_3$, BGO and NaI absorber detectors are expected to be as good as 8.3 %, 4.1 %, 14 % and 6 %.

C. Evaluation of the camera performances

After selecting only the events with energy deposited in one layer of the stack and in the absorber detector, the source position is reconstructed by intersecting the Compton cone with the y axis that would stand in a realistic set-up for the beam direction. If several interactions occur in one detector, we use the energy-weighted average position of the interaction points (barycentre). Thus we obtain the 1D point spread function (PSF) of the camera. The spatial resolution of the camera is defined as the FWHM of the PSF.

The detection efficiency D_E is defined as:

$$D_E = \frac{N_r}{N_i}, \text{ where} \qquad (3)$$

- N_r is the number of reconstructed Compton events, i.e. corresponding to an energy deposit in only one layer of the stack and in the absorber detector.
- N_i the number of photons emitted isotropically in 4π sr.

The percentage of total absorption among true events, $P_{t.a}$, is defined as:

$$P_{t.a.} = 100 \times \frac{N_{t.a}}{N_t}, \text{ where} \qquad (4)$$

- N_t the number of true events, i.e. corresponding to one Compton interaction in a single layer of silicon without energy escape and at least one interaction of the scattered photon in the absorber detector.
- $N_{t.a}$ the number of true events corresponding to the total absorption of the scattered photon in the absorber detector.

IV. Results

A. Energy deposited in the absorber detector

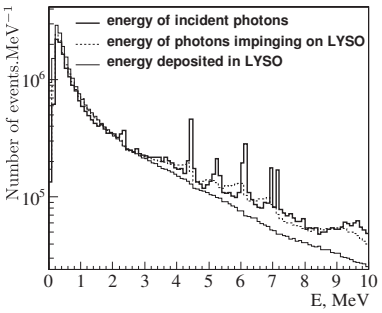

Fig. 3. Energy spectra for all reconstructed events in the case of a 4 cm thick LYSO absorber detector for 5×10^8 incident photons in 4π sr. The incident spectrum corresponds to prompt γ-rays generated in water by a 310 MeV/u ^{12}C ion beam.

In this section we consider a 4 cm thick LYSO detector as absorber detector. Fig. 3 represents, for all the reconstructed events, the distribution of (i) the energy of the photons incident on the scatter detector, (ii) the energy of the photons impinging on the absorber detector and (iii) the energy deposited in the absorber detector. The mean energy deposited in a 4 cm thick LYSO absorber is 1.7 MeV. As expected, above a few MeV, the number of photons which deposit all their energy in the absorber detector drops, and the spectra for "energy of photons impinging on LYSO" and "energy deposited in LYSO" diverge.

B. Absorber thickness & width

Fig. 4 shows the influence of the absorber detector thickness t_D on the spatial resolution of the camera and on the detection efficiency for 30 cm wide LYSO, $LaBr_3$, BGO and NaI absorber detectors. As t_D is increased from 1.5 to 7.5 cm, the detection efficiency grows, as one would expect from the exponential attenuation law. The maximum gain in the detection efficiency is a factor of 2. Concerning the spatial resolution of the camera, there is an optimal thickness. Indeed, when increasing t_D, we increase the number of photons fully absorbed ($N_{t.a.}$) which improves the resolution. However increasing t_D also increases the parallax error due to the fact that we have no information on the interaction depth. For a 30 cm wide detector the optimal thickness is around 4 cm for LYSO, 5 cm for $LaBr_3$, 4.5 cm for BGO and 6 cm for NaI.

Fig. 5 shows the influence of the absorber detector width w_D on the spatial resolution of the camera and on the detection efficiency for a 4 cm thick LYSO, a 5 cm thick $LaBr_3$, a 4.5 cm thick BGO and a 6 cm thick NaI absorber detector. Naturally, the detection efficiency increases with the detector width. The influence of the detector width on the detection efficiency is more pronounced than that of its thickness.

Between 10 and 30 cm, w_D has little influence on the spatial resolution of the camera. For absorber detector widths greater than 30 cm, the spatial resolution of the camera deteriorates. One explanation for this behavior is that we reconstruct

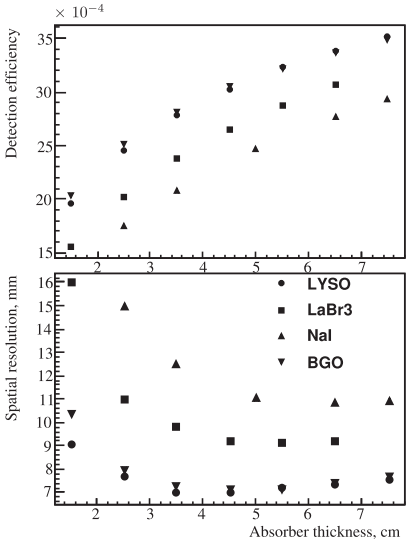

Fig. 4. Influence of the absorber detector thickness on the detection efficiency and on the spatial resolution of the camera. In these simulations, the width of the absorber detector is 30 cm. As the absorber thickness increases, the detection efficiency increases; the spatial resolution first improves and then deteriorates.

Compton events for which the low energy (associated to a large ϑ angle) Compton photons impinge on a detector edge and the angular error for these events is higher due to a higher parallax error (no depth of interaction measured in the absorber detector).

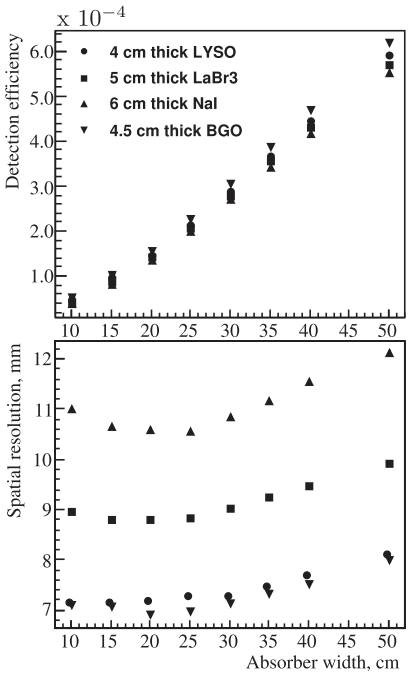

Fig. 5. Influence of the absorber detector width on the detection efficiency and on the spatial resolution of the camera. As the absorber width increases, the detection efficiency increases. For absorber detector widths below 30 cm the spatial resolution is almost constant.

TABLE I
EXPECTED FEATURES OF THREE SCINTILLATORS

Material	LYSO	$LaBr_3$	BGO	NaI
Dimensions, cm ($30 \times 30 \times \cdots$)	4	5	4.5	6
Density	6.50	5.08	7.13	3.67
$\Delta E/E$ FWHM@ 1 MeV (%)	8	4.1	14	6.0
Radioactivity (Bq/cm^3)	277	0.4	0	0
Efficiency ($\times 10^{-4}$)	3	2.8	3	2.7
$P_{t.a.}$, %	76	64	81	64
FWHM, mm	7	9	7	11

C. Absorber material

In Table I we compare the performances of LYSO, $LaBr_3$, BGO and NaI in a case corresponding to the optimal thickness for each material. This leads to very close values of the detection efficiency. The comparison of LYSO, $LaBr_3$ and BGO brings out the fact that the percentage of total absorption is the main parameter to optimise the spatial resolution of the camera. BGO is the material with the highest Z here. Thus the percentage of total absorption in BGO which depends directly on the photo-electric cross-section is higher than in the other materials. This explains why, despite a significantly lower energy resolution, the FWHM of a camera with a BGO absorber detector is the same as the FWHM of a camera with a LYSO absorber detector and better than the FWHM for $LaBr_3$ and NaI.

When several interactions occur in the absorber detector, the Compton cone should be ideally reconstructed from the position of the first interaction. Actually, it is reconstructed from an energy-weighted barycentre. If the photo-electric cross-section is higher, the fraction of photons undergoing only one photo-electric interaction in the absorber detector increases, i.e. the number of photons for which the barycentre position matches the position of the first interaction increases and the spatial resolution of the camera improves. For a 4 cm thick LYSO detector and a 4.5 cm thick BGO detector the mean distance between the first interaction and the barycentre is 3.4 mm. It is 4.9 mm for a 5 cm thick $LaBr_3$ detector and 5.5 mm for a 6 cm thick NaI detector.

The spatial resolution of the camera is also determined to a lesser extent by the energy resolution of the scintillator (see $LaBr_3$ vs NaI).

D. Absorber resolutions

Although the depth of interaction measurement in the absorber detector is not likely to be implemented in the prototype as it was assumed in above simulations, we propose here, in the case of a $30 \times 30 \times 4$ cm^3 LYSO absorber detector, to study the influence of the energy and spatial resolutions of this detector on the spatial resolution of the camera. Fig. 6 shows the variability of the spatial resolution of the camera as a function of each resolution of the absorber detector. The most important point is that the spatial resolution of the camera is not influenced significantly by the depth resolution. This justifies our previous choice not to measure the depth of interaction in the absorber detector.

The influence of the energy and lateral resolution are more pronounced: when deteriorating $\Delta_{XY,LYSO}$, the FWHM

lateral spatial resolution of the LYSO detector, by 1 mm, the camera resolution worsens by approximately 0.4 mm. When deteriorating $\Delta_{E,LYSO}$, the FWHM energy resolution of the LYSO detector at 1 MeV, by 1% the camera's spatial resolution worsens by approximately 0.13 mm.

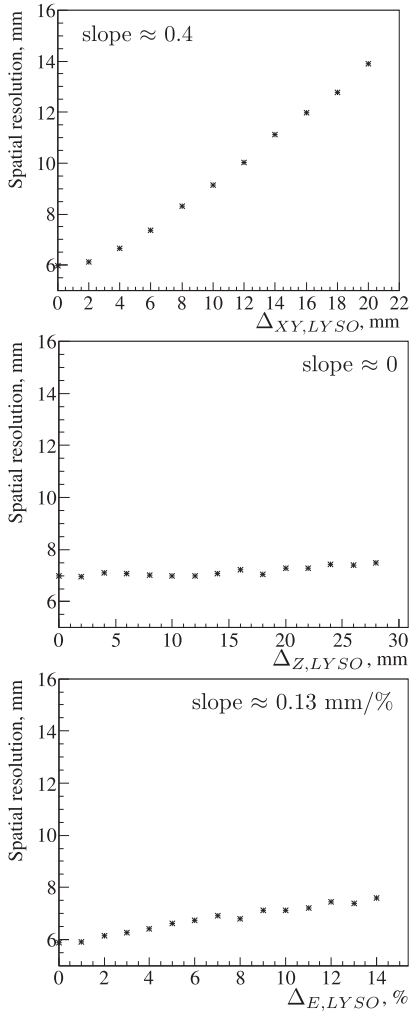

Fig. 6. Influence of the absorber detector resolutions on the spatial resolution of the camera. $\Delta_{XY,LYSO}$, $\Delta_{Z,LYSO}$, and $\Delta_{E,LYSO}$ are the FWHM lateral spatial resolution, in-depth spatial resolution, and energy resolution of the LYSO detector, respectively.

V. Conclusion

In this paper, we have studied the influence of the material, dimensions and resolutions of the absorber detector on the spatial resolution of a Compton camera for ion beam therapy. Even in an optimal geometry, the spatial resolution of a Compton camera with a NaI absorber detector remains the poorest. $LaBr_3$ shows good performances due to its quite good energy resolution but is still limited by a low percentage of total absorption. LYSO and BGO provide the best results in terms of spatial resolution and detection efficiency. However, the impact of the LYSO internal radioactivity on the signal to noise ratio in clinical conditions has to be quantified. Another important issue is the consequence of the relatively poor time resolution achievable with a BGO detector on the discrimination between prompt γ-rays and neutrons. To go further, experimental data would be required, which is foreseen in the near future.

In our case, the thickness which gives the best compromise between a high percentage of photons that are fully absorbed and a low parallax error is about 4 cm for the LYSO detector and 4.5 cm for the BGO detector. Finally, we found that for a detector with a thickness of a few centimetres, measuring the depth of interaction is not necessary.

Further simulations in more realistic conditions (ion beam irradiation, patient phantom, time structure of the beam) are needed to confirm the applicability of our method. We will focus on counting rates in the detectors, on noise induced by other secondary particles emitted during the irradiation, on pile-up and on fortuitous coincidences.

In parallel, we intend to validate these simulations with a small size prototype. The scatter detector will consist of ten $8\times8\times0.2$ cm^3 silicon strip detectors. Two absorber detectors will be compared : one $10\times10\times4$ cm^3 LYSO detector and one $10\times10\times4.5$ cm^3 BGO detector. The first step is to characterise our detectors in terms of efficiency, and of position, energy and time resolution, and then to study their response to both photon and ion sources.

Acknowledgment

These studies are supported by the Rhône-Alpes Research Program for Hadrontherapy, the ENVISION FP7 project (grant agreement 241851) and Gamhadron ANR project. Monte Carlo simulations have been run at the IN2P3 Computing Centre (CC-IN2P3) in Lyon, France

References

[1] A. R. Smith, "Vision 20/20: Proton therapy," *Med. Phys.*, vol. 36, no. 2, pp. 556–568, 2009.

[2] C. H. Min, C. H. Kim, M. Youn, and J. W. Kim, "Prompt-gamma measurements for locating the dose falloff region in the proton therapy," *Appl. Phys. Lett.*, vol. 89, no. 18, p. 183517, 2006.

[3] E. Testa, M. Bajard, M. Chevallier, D. Dauvergne, F. Le Foulher, N. Freud *et al.*, "Dose profile monitoring with carbon ions by means of prompt-gamma measurements," *Nucl. Instr. Meth. Phys. Res., Sect. B*, vol. 267, no. 6, pp. 993 – 996, 2009.

[4] E. Testa, M. Bajard, M. Chevallier, D. Dauvergne, F. Le Foulher, N. Freud *et al.*, "Monitoring the Bragg peak location of 73 MeV/u carbon ions by means of prompt-γ ray measurements," *Appl. Phys. Lett.*, vol. 93, no. 9, p. 093506, 2008.

[5] T. Kormoll, F. Fiedler, S. Söchne, J. Wüstemann, K. Zuber, and W. Enghardt, "A Compton imager for in-vivo dosimetry of proton beams: A design study," *Nucl. Instr. Meth. Phys. Res., Sect. A*, vol. 626-627, no. 0, pp. 114 – 119, 2011.

[6] S. Kurosawa, H. Kubo, K. Ueno, S. Kabuki, S. Iwaki, M. Takahashi *et al.*, "Prompt gamma detection for range verification in proton therapy," *Current Applied Physics*, vol. 12, no. 2, pp. 364 – 368, 2012.

[7] G. Llosá, J. Barrio, J. Cabello, A. Crespo, C. Lacasta, M. Rafecas *et al.*, "Detector characterization and first coincidence tests of a Compton telescope based on $LaBr_3$ crystals and SiPMs," *Nucl. Instr. Meth. Phys. Res., Sect. A*, 2011, In Press.

[8] D. Robertson, J. Polf, S. W. Peterson, M. Gillin, and S. Beddar, "Material efficiency studies for a Compton camera designed to measure characteristic prompt gamma rays emitted during proton beam radiotherapy," *Phys. Med. Biol.*, vol. 56, no. 10, p. 3047, 2011.

[9] M.-H. Richard, M. Chevallier, D. Dauvergne, N. Freud, P. Henriquet, F. Le Foulher *et al.*, "Design guidelines for a double scattering Compton camera for prompt-γ imaging during ion beam therapy: A Monte Carlo simulation study," *IEEE Trans. Nucl. Sci.*, vol. 58, no. 1, pp. 87 – 94, 2011.

[10] F. Roellinghoff, M.-H. Richard, M. Chevallier, J. Constanzo, D. Dauvergne, N. Freud *et al.*, "Design of a Compton camera for 3D prompt-γ imaging during ion beam therapy," *Nucl. Instr. Meth. Phys. Res., Sect. A*, vol. 648, no. Supp. 1, p. S20–S23, 2011.

[11] S. Agostinelli, J. Allison, K. Amako, J. Apostolakis, H. Araujo, P. Arce *et al.*, "Geant4–a simulation toolkit," *Nucl. Instr. Meth. Phys. Res., Sect. A*, vol. 506, no. 3, pp. 250 – 303, 2003.

[12] G. Cirrone, G. Cuttone, F. D. Rosa, L. Pandola, F. Romano, and Q. Zhang, "Validation of the Geant4 electromagnetic photon cross-sections for elements and compounds," *Nucl. Instr. Meth. Phys. Res., Sect. A*, vol. 618, no. 1-3, pp. 315 – 322, 2010.

[13] G. L. Zeng, J. R. Galt, M. N. Wernick, R. A. Mintzer, and J. N. Aarsvold, "Chapter 7 - single-photon emission computed tomography," in *Emission Tomography*, ser. The Fundamentals of Pet and Spect, M. N. Wernick and J. N. Aarsvold, Eds. San Diego: Elsevier Academic Press, 2004, pp. 127 – 152.

[14] J. Kataoka, M. Koizumi, S. Tanaka, H. Ishibashi, T. Nakamori, N. Kawai *et al.*, "Development of large-area, reverse-type APD-arrays for high-resolution medical imaging," *Nucl. Instr. Meth. Phys. Res., Sect. A*, vol. 604, no. 1-2, pp. 323 – 326, 2009, PSD8 - Proceedings of the 8th International Conference on Position Sensitive Detectors.

[15] C. W. E. van Eijk, "Inorganic scintillators in medical imaging," *Phys. Med. Biol.*, vol. 47, no. 8, pp. R85 – R106, 2002.

[16] K. Hattori, S. Kabuki, H. Kubo, S. Kurosawa, K. Miuchi, T. Nagayoshi *et al.*, "Gamma-ray imaging with a large micro-TPC and a scintillation camera," *Nucl. Instr. Meth. Phys. Res., Sect. A*, vol. 581, no. 1-2, pp. 517 – 521, 2007, VCI 2007 - Proceedings of the 11^{th} International Vienna Conference on Instrumentation.

Bibliography

[Achenbach2008] P. Achenbach, C. Ayerbe Gayoso, J.C. Bernauer, and R. B˙ In-beam tests of scintillating fibre detectors at MAMI and at GSI. *Nuclear Instruments and Methods in Physics Research Section A: Accelerators, Spectrometers, Detectors and Associated Equipment*, 593(3):353 – 360, 2008.

[Agostinelli2003] S. Agostinelli, J. Allison, K. Amako, J. Apostolakis, H. Araujo, P. Arce, et al. Geant4–a simulation toolkit. *Nuclear Instruments and Methods in Physics Research Section A: Accelerators, Spectrometers, Detectors and Associated Equipment*, 506(3):250 – 303, 2003.

[Amaldi2010] U. Amaldi, W. Hajdas, S. Iliescu, N. Malakhov, J. Samarati, F. Sauli, and D. Watts. Advanced Quality Assurance for CNAO. *Nuclear Instruments and Methods in Physics Research Section A: Accelerators, Spectrometers, Detectors and Associated Equipment*, 617(13):248 – 249, 2010. 11th Pisa Meeting on Advanced Detectors, proceedings of the 11th Pisa Meeting on Advanced Detectors.

[Amaldi2011] U. Amaldi and S. Braccini. Present challenges in hadrontherapy techniques. *The European Physical Journal Plus*, 126:1–15, 2011.

[Andritschke2005] R. Andritschke, A. Zoglauer, G. Kanbach, P. Bloser, and F. Schopper. The Compton and pair creation telescope MEGA. *Experimental Astronomy*, 20:395–403, 2005.

[Ballarini2007] F. Ballarini, G. Battistoni, M. Brugger, M. Campanella, M. Carboni, F. Cerutti, et al. The physics of the FLUKA code: Recent developments. *Advances in Space Research*, 40(9):1339 – 1349, 2007.

[Baro1995] J. Baró, J. Sempau, J.M. Fernández-Varea, and F. Salvat. PENELOPE: An algorithm for Monte Carlo simulation of the penetration and energy loss of electrons and positrons in matter. *Nuclear Instruments and Methods in Physics Research Section B: Beam Interactions with Materials and Atoms*, 100(1):31 – 46, 1995.

[Basko1998] R. Basko, G. L. Zeng, and G. T. Gullberg. Application of spherical harmonics to image reconstruction for the Compton camera. *Physics in Medicine and Biology*, 43(4):887, 1998.

[Bergonzo2001] P. Bergonzo, A. Brambilla, D. Tromson, C. Mer, B. Guizard, F. Foulon, and V. Amosov. CVD diamond for radiation detection devices. *Diamond and Related Materials*, 10(37):631 – 638, 2001. 11th European Conference on Diamond, Diamond-like Materials, Carbon Nanotubes, Nitrides and Silicon Carbide.

[Bielajew1994] A. Bielajew et al. History, overview and recent improvement of egs4. Technical report, 1994. Technical report PIRS-0436.

[Bohlen2010] T. T. Böhlen, F. Cerutti, M. Dosanjh, A. Ferrari, I. Gudowska, A. Mairani, and J. M. Quesada. Benchmarking nuclear models of FLUKA and GEANT4 for carbon ion therapy. *Physics in Medicine and Biology*, 55(19):5833, 2010.

[Cirrone2010] G.A.P. Cirrone, G. Cuttone, F. Di Rosa, L. Pandola, F. Romano, and Q. Zhang. Validation of the Geant4 electromagnetic photon cross-sections for elements and compounds. *Nuclear Instruments and Methods in Physics Research Section A: Accelerators, Spectrometers, Detectors and Associated Equipment*, 618(1-3):315 – 322, 2010.

[Cree1994] M. J. Cree and P. J. Bones. Towards direct reconstruction from a gamma camera based on Compton scattering. *IEEE Transactions on Medical Imaging*, 13(2):398–407, 1994.

[Crespo2007] P. Crespo, G. Shakirin, F. Fiedler, W. Enghardt, and A. Wagner. Direct time-of-flight for quantitative, real-time in-beam PET: a concept and feasibility study. *Physics in Medicine and Biology*, 52(23):6795, 2007.

[Dedes2012] G. Dedes, M. Chevallier, D. Dauvergne, M. De Rydt, N. Freud, J. Krimmer, J.M. Ltang, M. Pinto, C. Ray, V. Reithinger, M.H. Richard, F. Roellinghoff, and E. Testa. 148 REAL-TIME PROMPT GAMMA RAY MONITORING FOR PROTON AND CARBON THERAPY: MONTE CARLO NUCLEAR MODELS EVALUATION AND IMPROVEMENTS. *Radiotherapy and Oncology*, 102, Supplement 1(0):S68 – S69, 2012. ICTR-PHE 2012 Conference.

[Dogan1992] N. Dogan, D.K. Wehe, and A.Z. Akcasu. A source reconstruction method for multiple scatter Compton cameras. *IEEE Transactions on Nuclear Science*, 39(5):1427–1430, 1992.

[Durante2010] M. Durante and J.S. Loeffler. Charged particles in radiation oncology. *Nature Reviews Clinical Oncology*, 7:37–43, 2010.

[Eberly2002] P. J. Schneider and D. H. Eberly. *Geometric Tools for Computer Graphics*. The Morgan Kaufmann Series in Computer Graphics and Geometric Modeling. Morgan Kaufmann, 2002.

[Eickhoff2003] H. Eickhoff, R. Bar, A. Dolinskii, T. Haberer, B. Schlitt, P. Spiller, U. Weinrich, and GSI Therapy Project Grp. HICAT - The German hospital-based light ion cancer therapy project. In Chew, J and Lucas, P and Webber, S, editor, *PROCEEDINGS OF THE 2003 PARTICLE ACCELERATOR CONFERENCE, VOLS 1-5*, pages 694–698, 2003.

[Enghardt2004] W. Enghardt, P. Crespo, F. Fiedler, R. Hinz, K. Parodi, J. Pawelke, and F. Pönisch. Charged hadron tumour therapy monitoring by means of PET. *Nuclear Instruments and Methods in Physics Research Section A: Accelerators, Spectrometers, Detectors and Associated Equipment*, 525(1-2):284 – 288, 2004. Proceedings of the International Conference on Imaging Techniques in Subatomic Physics, Astrophysics, Medicine, Biology and Industry.

[Envision2012] W. Enghardt D. Dauvergne. D3.1 Compilation of γ-ray yield data, estimation of radiation backgroundinfluencing prompt photon imaging. Technical report, European NoVel Imaging Systems for ION therapy, 2012.

[Fiedler2011] F. Fiedler, U. Dersch, C. Golnik, T. Kormoll, A. Müller, H. Rohling, S. Schöne, and W. Enghardt. The Use of Prompt γ-rays for in-vivo Dosimetry at Therapeutic Proton and Ion Beams. In *Nuclear Science Symposium Conference Record (NSS/MIC), 2011 IEEE*, oct. 2011.

[Fokas2009] E. Fokas, G. Kraft, H. An, and R. Engenhart-Cabillic. Ion beam radiobiology and cancer: Time to update ourselves. *Biochimica et Biophysica Acta (BBA) - Reviews on Cancer*, 1796(2):216 – 229, 2009.

[Folger2004] G. Folger, V. N. Ivanchenko, and J. P. Wellisch. The binary cascade. *The European Physical Journal A - Hadrons and Nuclei*, 21:407–417, 2004.

[Gottschalk2008] B. Gottschalk and E. Pedroni. Treatment delivery systems. In T. F. DeLaney and H. M. Kooy, editors, *Proton and Charged Particle Radiotherapy*, chapter 5, pages 33 – 49. Lippincott Williams and Wilkins, Philadelphia, 2008.

[Grevillot2010] L. Grevillot, T. Frisson, N. Zahra, D. Bertrand, F. Stichelbaut, N. Freud, and D. Sarrut. Optimization of GEANT4 settings for Proton Pencil Beam Scanning simulations using GATE. *Nuclear Instruments and Methods in Physics Research Section B: Beam Interactions with Materials and Atoms*, 268(20):3295 – 3305, 2010.

[Gudowska2004] I. Gudowska, N. Sobolevsky, P. Andreo, D. Belkić, and A. Brahme. Ion beam transport in tissue-like media using the Monte Carlo code SHIELD-HIT. *Physics in Medicine and Biology*, 49(10):1933, 2004.

[Gunzert-Marx2008] K. Gunzert-Marx, H. Iwase, D. Schardt, and R. S. Simon. Secondary beam fragments produced by 200 MeV/u ^{12}C ions in water and their dose contributions in carbon ion radiotherapy. *New Journal of Physics*, 10(7):075003, 2008.

[Harkness2009] L.J. Harkness, A.J. Boston, H.C. Boston, R.J. Cooper, J.R. Cresswell, A.N. Grint, P.J. Nolan, D.C. Oxley, D.P. Scraggs, T. Beveridge, J. Gillam, and I. Lazarus. Optimisation of a dual head semiconductor Compton camera using Geant4. *Nuclear Instruments and Methods in Physics Research Section A: Accelerators, Spectrometers, Detectors and Associated Equipment*, 604(1-2):351 – 354, 2009. Proceedings of the 8th International Conference on Position Sensitive Detectors.

[Henriquet2012] P. Henriquet, E. Testa, M. Chevallier, D. Dauvergne, G. Dedes, N. Freud, J. Krimmer, J. M. Létang, C. Ray, M.-H. Richard, and F. Sauli. Interaction vertex imaging (IVI) for carbon ion therapy monitoring: a feasibility study. To be published in Physics in Medicine and Biology.

[HenriquetPhd2011] P. Henriquet. *Study of the emission of secondary charged particles during ion beam therapy for beam monitoring purposes*. PhD thesis, Université Lyon 1, July 2011.

[Herzo1975] D. Herzo, R. Koga, W.A. Millard, S. Moon, J. Ryan, R. Wilson, A.D. Zych, and R.S. White. A large double scatter telescope for gamma rays and neutrons. *Nuclear Instruments and Methods*, 123(3):583 – 597, 1975.

[Hirasawa2003] M. Hirasawa and T. Tomitani. An analytical image reconstruction algorithm to compensate for scattering angle broadening in Compton cameras. *Physics in Medicine and Biology*, 48(8):1009–1026, 2003.

[ICRU2007Report78] *Prescribing, recording, and reporting proton-beam therapy*, volume 7. ICRU, Bethesda, MD, 2007.

[Jakel2001] O. Jäkel, M. Krämer, C. P. Karger, and J. Debus. Treatment planning for heavy ion radiotherapy: clinical implementation and application. *Physics in Medicine and Biology*, 46(4):1101, 2001.

[James2006] M. R. James, G. W. McKinney, J. S. Hendricks, and M. Moyers. Recent enhancements in MCNPX: Heavy-ion transport and the LAQGSM physics model. *Nuclear Instruments and Methods in Physics Research Section A: Accelerators, Spectrometers, Detectors and Associated Equipment*, 562(2):819 – 822, 2006. Proceedings of the 7th International Conference on Accelerator Applications.

[Jan2004] S. Jan et al. GATE: a simulation toolkit for PET and SPECT. *Physics in Medicine and Biology*, 49(19):4543, 2004.

[Jansen2007] F. P. Jansen and J.-L. Vanderheyden. The future of SPECT in a time of PET. *Nuclear Medicine and Biology*, 34(7):733 – 735, 2007.

[Jongen2010] Y. Jongen, M. Abs, A. Blondin, W. Kleeven, S. Zaremba, D. Vandeplassche, V. Aleksandrov, S. Gursky, O. Karamyshev, G. Karamysheva, N. Kazarinov, S. Kostromin, N. Morozov, E. Samsonov, G. Shirkov, V. Shevtsov, E. Syresin, and A. Tuzikov. Compact superconducting cyclotron C400 for hadron therapy. *Nuclear Instruments and Methods in Physics Research Section A: Accelerators, Spectrometers, Detectors and Associated Equipment*, 624(1):47 – 53, 2010.

[Kadri2007] O. Kadri, V.N. Ivanchenko, F. Gharbi, and A. Trabelsi. GEANT4 simulation of electron energy deposition in extended media. *Nuclear Instruments and Methods in Physics Research Section B: Beam Interactions with Materials and Atoms*, 258(2):381 – 387, 2007.

[Kang2009] B. Hwi-Kang and J. W. Kim. Monte Carlo design study of a gamma detector system to locate distal dose falloff in proton therapy. *IEEE Transactions on Nuclear Science*, 56(1):46 –50, 2009.

[Kataoka2009] J. Kataoka, M. Koizumi, S. Tanaka, H. Ishibashi, T. Nakamori, N. Kawai, H. Ikeda, Y. Ishikawa, N. Kawabata, Y. Matsunaga, S. Kishimoto, and H. Kubo. Development of large-area, reverse-type APD-arrays for high-resolution medical imaging. *Nuclear Instruments and Methods in Physics Research Section A: Accelerators, Spectrometers, Detectors and Associated Equipment*, 604(1-2):323 – 326, 2009. PSD8 - Proceedings of the 8th International Conference on Position Sensitive Detectors.

[Knoll2012] G.F. Knoll. *Radiation Detection and Measurement*. John Wiley & Sons, 2010. Chapter 3 Counting statistics and error prediction.

[Koi2010] T. Koi on behalf of the Geant4 Hadronic Working Group. New native QMD code in Geant4. In *Joint International Conference on Supercomputing in Nuclear Applications and Monte Carlo*, 2010.

[Kormoll2011] T. Kormoll, F. Fiedler, C. Golnik, K. Heidel, M. Kempe, S. Schoene, M. Sobiella, K. Zuber, and W. Enghardt. A prototype Compton camera for in-vivo dosimetry of ion beam cancer irradiation . In *Nuclear Science Symposium Conference Record, 2011 IEEE*, volume 1, pages 3484 – 3487, oct. 2011.

[Kozlovsky2002] B. Kozlovsky, R. J. Murphy, and R. Ramaty. Nuclear Deexcitation Gamma-Ray Lines from Accelerated Particle Interactions. *The Astrophysical Journal Supplement Series*, 141(2):523, 2002.

[Kramer2000] M Krämer, O Jäkel, T Haberer, G Kraft, D Schardt, and U Weber. Treatment planning for heavy-ion radiotherapy: physical beam model and dose optimization. *Physics in Medicine and Biology*, 45(11):3299–3317, 2000.

[Kroeger2002] R.A. Kroeger, W.N. Johnson, J.D. Kurfess, B.F. Phlips, and E.A. Wulf. Three-Compton telescope: theory, simulations, and performance. *IEEE Transactions on Nuclear Science*, 49(4):1887–1892, 2002.

[Kurosawa2010] S. Kurosawa, H. Kubo, K. Hattori, C. Ida, S. Iwaki, S. Kabuki, A. Kubo, E. Kunieda, K. Miuchi, T. Nakahara, H. Nishimura, J.D. Parker, A. Takada, M. Takahashi, T. Tanimori, and K. Ueno. Development of an 8×8 array of LaBr3(Ce) scintillator pixels for a gaseous Compton gamma-ray camera. *Nuclear Instruments and Methods in Physics Research Section A: Accelerators, Spectrometers, Detectors and Associated Equipment*, 623(1):249 – 251, 2010. 1st International Conference on Technology and Instrumentation in Particle Physics.

[Kurosawa2012] S. Kurosawa, H. Kubo, K. Ueno, S. Kabuki, S. Iwaki, M. Takahashi, K. Taniue, N. Higashi, K. Miuchi, T. Tanimori, D. Kim, and J. Kim. Prompt gamma detection for range verification in proton therapy. *Current Applied Physics*, 12(2):364 – 368, 2012.

[Lechner2010] A. Lechner, V.N. Ivanchenko, and J. Knobloch. Validation of recent Geant4 physics models for application in carbon ion therapy. *Nuclear Instruments and Methods in Physics Research Section B: Beam Interactions with Materials and Atoms*, 268(14):2343 – 2354, 2010.

[Lefoulher2010] F. Le Foulher, M. Bajard, M. Chevallier, D. Dauvergne, N. Freud, P. Henriquet, S. Karkar, J.M. Létang, R. Plescak, C. Ray, D. Schardt, E. Testa, and M. Testa. Monte Carlo simulations of prompt-gamma emission during carbon ion irradiation. *IEEE Transactions on Nuclear Science*, 57(5):2768 – 2772, 2010.

[LefoulherPhd2010] F. Le Foulher. *Monte Carlo simulation and measurements of prompt-gamma emission for on line beam monitoring ion ion beam therapy*. PhD thesis, Université Lyon 1, October 2010.

[Llosa2010] G. Llosá, J. Barrio, C. Lacasta, S. Callier, C. de La Taille, and L. Raux. Characterization of a detector head based on continuous LaBr3 crystals and SiPM arrays for dose monitoring in hadron therapy. In *Nuclear Science Symposium Conference Record (NSS/MIC), 2010 IEEE*, pages 2148 –2150, oct. 2010.

[Lojacono2011a] X. Lojacono, M. Richard, C. Ray, D. Dauvergne, E. Testa, N. Freud, J.M. Létang, V. Maxim, and R. Prost. Image reconstruction for Compton camera applied to 3D prompt γ imaging during ion beam therapy . In *Nuclear Science Symposium Conference Record, 2011 IEEE*, volume 1, pages 3518 – 3521, oct. 2011.

[Lojacono2011b] X. Lojacono, V. Maxim, and R. Prost. Calcul de la matrice des probabilités de transfert en imagerie compton 3d. In *XXIIIe Colloque GRETSI - Traitement du Signal et des Images (GRETSI'11)*, page ID432, 2011 2011.

[Mantero2007] A. Mantero, B. Mascialino, M.G. Pia, and V. Zampichelli. Validation of geant4 atomic relaxation against the nist physical reference data. *IEEE Transactions on Nuclear Science*, 54:594–603, 2007.

[Maxim2009] V. Maxim, M. Frandes, and R. Prost. Analytical inversion of the Compton transform using the full set of available projections. *Inverse Problems*, 25(9):095001 (21pp), 2009.

[Min2006] C H. Min, C H. Kim, MY. Youn, and J W. Kim. Prompt-gamma measurements for locating the dose falloff region in the proton therapy. *Applied physics letters*, 89(18):183517, 2006.

[Moteabbed2011] M. Moteabbed, S. Espana, and H. Paganetti. Monte Carlo patient study on the comparison of prompt gamma and PET imaging for range verification in proton therapy. *Physics in Medicine and Biology*, 56(4):1063, 2011.

[Niedermayr2005] T. Niedermayr, K. Vetter, L. Mihailescu, G.J. Schmid, D. Beckedahl, J. Blair, and J. Kammeraad. Gamma-ray imaging with a coaxial HPGe detector. *Nuclear Instruments and Methods in Physics Research Section A: Accelerators, Spectrometers, Detectors and Associated Equipment*, 553(3):501 – 511, 2005.

[Nose2005] H. Nose, K. Niita, M. Hara, K. Uematsu, O. Azuma, Y. Miyauchi, M. Komori, and T. Kanai. Improvement of Three-dimensional Monte Carlo Code PHITS for Heavy Ion Therapy. *Journal of Nuclear Science and Technology*, 42(2):250–255, 2005.

[Oonuki2007] K. Oonuki, T. Tanaka, S. Watanabe, S. Takeda, K. Nakazawa, M. Ushio, T. Mitani, T. Takahashi, and H. Tajima. A stacked CdTe pixel detector for a Compton camera. *Nuclear Instruments and Methods in Physics Research Section A: Accelerators, Spectrometers, Detectors and Associated Equipment*, 573(1-2):57 – 60, 2007.

[Paganetti2012] H. Paganetti. Range uncertainties in proton therapy and the role of Monte Carlo simulations. *Physics in Medicine and Biology*, 57(11):R99, 2012.

[Park2009] I. Park. A new approach to produce spread-out Bragg peak using the MINUIT fit. *Current Applied Physics*, 9(4):852 – 855, 2009.

[Parodi2008] K. Parodi, T. Bortfeld, and T. Haberer. Comparison between in-beam and offline positron emission tomography imaging of proton and carbon ion therapeutic irradiation at synchrotron- and cyclotron-based facilities. *International journal of radiation oncology, biology, physics*, 71(3):945 – 956, 2008.

[ParodiPhd2004] K. Parodi. *On the feasibility of dose quantification with in-beam PET data in radiotherapy with ^{12}C and proton beams*. PhD thesis, Fakultät Mathematik und Naturwissenschaften der Technischen Universität Dresden, 2004.

[Parra2000] L. C. Parra. Reconstruction of cone-beam projections from compton scattered data. *IEEE Transactions on Nuclear Science*, 47(4):1543–1550, 2004.

[Peters2008] A. Peters, R. Cee, Th. Haberer, T. Hoffmann, A. Reiter, M. Schwickert, and T. Winkelmann. Spill structure measurements at the Heidelberg ion therapy centre. *European Particle Accelerator Conference*, TUPP127, 2008.

[Phillips1995] Gary W. Phillips. Gamma-ray imaging with Compton cameras. *Nuclear Instruments and Methods in Physics Research Section B: Beam Interactions with Materials and Atoms*, 99(1-4):674 – 677, 1995.

[Podgorsak2003] E.B. Podgoršak and International Atomic Energy Agency. *Review of radiation oncology physics: a handbook for teachers and students*. International Atomic Energy Agency, 2003.

[Polf2009] J. C. Polf, S. Peterson, M. McCleskey, B. T. Roeder, A. Spiridon, S. Beddar, and L. Trache. Measurement and calculation of characteristic prompt gamma ray spectra emitted during proton irradiation. *Physics in Medicine and Biology*, 54(22):N519, 2009.

[Qi2006] J. Qi and R. M. Leahy. Iterative reconstruction techniques in emission computed tomography. *Physics in Medicine and Biology*, 51(15):R541, 2006.

[RebiszPomorska2010] M. Rebisz-Pomorska, M. Ciobanu, M. Kis, M. Pomorski, and B. Voss. Diamond detectors for the monitoring of carbon-ion therapy beams. *Nuclear Instruments and Methods in Physics Research Section A: Accelerators, Spectrometers, Detectors and Associated Equipment*, 620(23):534 – 539, 2010.

[Richard2011] M.-H. Richard, M. Chevallier, D. Dauvergne, N. Freud, P. Henriquet, F. Le Foulher, J. M. Letang, G. Montarou, C. Ray, F. Roellinghoff, E. Testa, M. Testa, and A.H. Walenta. Design guidelines for a double scattering Compton camera for prompt-γ imaging during ion beam therapy: A Monte Carlo simulation study. *IEEE Transactions on Nuclear Science*, 58(1):87 – 94, 2011.

[Richard2012] M.-H. Richard, M. Dahoumane, D. Dauvergne, M. De Rydt, G. Dedes, N. Freud, J. Krimmer, J.M. Létang, X. Lojacono, V. Maxim, G. Montarou, C. Ray, F. Roellinghoff, E. Testa, and A.H. Walenta. Design Study of the Absorber Detector of a Compton Camera for Online Control in Ion Beam Therapy. Submitted to IEEE Transactions on Nuclear Science.

[Robertson2011] D. Robertson, J.C. Polf, S W. Peterson, M.T. Gillin, and S. Beddar. Material efficiency studies for a Compton camera designed to measure characteristic prompt gamma rays emitted during proton beam radiotherapy. *Physics in Medicine and Biology*, 56(10):3047, 2011.

[Roellinghoff2011] F. Roellinghoff, M.-H. Richard, M. Chevallier, J. Constanzo, D. Dauvergne, N. Freud, P. Henriquet, F. Le Foulher, J. M. Létang, G. Montarou, C. Ray, E. Testa, M. Testa, and A.H. Walenta. Design of a Compton camera for 3D prompt-γ imaging during ion beam therapy. *Nuclear Instruments and Methods in Physics Research Section A: Accelerators, Spectrometers, Detectors and Associated Equipment*, 648(Supp. 1):S20–S23, 2011.

[Rossi2011] P. Rossi, G. Baldazzi, A. Battistella, M. Bello, D. Bollini, V. Bonvicini, C.L. Fontana, G. Gennaro, G. Moschini, F. Navarria, A. Rashevsky, N. Uzunov, G. Zampa, N. Zampa, and A. Vacchi. Design and performance tests of the calorimetric tract of a Compton Camera for small-animals imaging. *Nuclear Instruments and Methods in Physics Research Section A: Accelerators, Spectrometers, Detectors and Associated Equipment*, 628(1):430 – 433, 2011. VCI 2010 Proceedings of the 12th International Vienna Conference on Instrumentation.

[Schall1996] I. Schall, D. Schardt, H. Geissel, H. Irnich, E. Kankeleit, G. Kraft, A. Magel, M.F. Mohar, G. Mnzenberg, F. Nickel, C. Scheidenberger, and W. Schwab. Charge-changing nuclear reactions of relativistic light-ion beams ($5 \leq Z \leq 10$) passing through thick absorbers. *Physics in Medicine and Biology*, 117(3):221 – 234, 1996.

[Schardt2010] D. Schardt, T. Elsässer, and D. Schulz-Ertner. Heavy-ion tumor therapy: Physical and radiobiological benefits. *Reviews of modern physics*, 82:383–425, 2010.

[Schone2010] G. ; Kormoll T. ; Herbach C. ; Pausch G. ; Enghardt W. Schone, S. ;Shakirin. A common approach to image reconstruction for different applications of Compton cameras . In *Nuclear Science Symposium Conference Record (NSS/MIC), 2010 IEEE*, pages 2292 – 2293, oct. 2010.

[Seo2008] H. Seo, S.H. Lee, C.H. Kim, S.H. An, J.H. Lee, and C.S. Lee. Optimal geometrical configuration of a double-scattering Compton camera for maximum imaging resolution and sensitivity. *Nuclear Instruments and Methods in Physics Research Section A: Accelerators, Spectrometers, Detectors and Associated Equipment*, 591(1):80 – 83, 2008.

[Seo2010] H. Seo, C. H. Kim, J. H. Park, J. K.g Kim, J. H. Lee, C. S. Lee, and J. S. Lee. Development of double-scattering-type Compton camera with double-sided silicon strip detectors and NaI(Tl) scintillation detector. *Nuclear Instruments and Methods in Physics Research Section A: Accelerators, Spectrometers, Detectors and Associated Equipment*, 615(3):333 – 339, 2010.

[Singh1983] Singh M. An eletronically collimated gamma camera for single photon computed tomography. Part 1: Theoretical considerations and design criteria. *Medical physics*, 10(4):421–427, 1983.

[Smeets2012] J. Smeets, F. Roellinghoff, D. Prieels, F. Stichelbaut, A. Benilov, P. Busca, C. Fiorini, R. Peloso, M. Basilavecchia, T. Frizzi, J. C. Dehaes, and A. Dubus. Prompt gamma imaging with a slit camera for real-time range control in proton therapy. *Physics in Medicine and Biology*, 57(11):3371, 2012.

[Smith2009] Alfred R. Smith. Vision 20/20: Proton therapy. *Medical physics*, 36(2):556–568, 2009.

[Stichelbaut2003] F. Stichelbaut and Y. Jongen. Verification of the Proton Beam Position in the Patient by the Detection of Prompt γ-Rays Emission. 39th Meeting of the Particle Therapy Co-Operative Group San Francisco.

[Struder2000] L. Struder. High-resolution imaging X-ray spectrometers. *Nuclear Instruments and Methods in Physics Research Section A: Accelerators, Spectrometers, Detectors and Associated Equipment*, 454(1):73 – 113, 2000.

[Studen2004] A. Studen, D. Burdette, E. Chesi, V. Cindro, N. H. Clinthorne, W. Dulinski, J. Fuster, L. Han, H. Kagan, C. Lacasta, G. Llos, A. C. Marques, N. Malakhov, D. Meier, M. Mikuz, S. J. Park, S. Roe, W. L. Rogers, J. Steinberg, P. Weilhammer, S. J. Wilderman, L. Zhang, and D. Zontar. First coincidences in pre-clinical Compton camera prototype for medical imaging. *Nuclear Instruments and Methods in Physics Research Section A: Accelerators,*

Spectrometers, Detectors and Associated Equipment, 531(1-2):258 – 264, 2004. Proceedings of the 5th International Workshop on Radiation Imaging Detectors.

[Takada2005] A. Takada, K. Hattori, H. Kubo, K. Miuchi, T. Nagayoshi, H. Nishimura, Y. Okada, R. Orito, H. Sekiya, A. Tada, and T. Tanimori. Development of an advanced Compton camera with gaseous TPC and scintillator. *Nuclear Instruments and Methods in Physics Research Section A: Accelerators, Spectrometers, Detectors and Associated Equipment*, 546(1-2):258 – 262, 2005. Proceedings of the 6th International Workshop on Radiation Imaging Detectors - Radiation Imaging Detectors 2004.

[Takeda2010] S. Takeda, H. Odaka, J. Katsuta, S. Ishikawa, S. Sugimoto, Y. Koseki, S. Watanabe, G. Sato, M. Kokubun, T. Takahashi, K. Nakazawa, Y. Fukazawa, H. Tajima, and H. Toyokawa. Polarimetric performance of Si/CdTe semiconductor Compton camera. *Nuclear Instruments and Methods in Physics Research Section A: Accelerators, Spectrometers, Detectors and Associated Equipment*, 622(3):619 – 627, 2010.

[Testa2008] E. Testa, M. Bajard, M. Chevallier, D. Dauvergne, F. Le Foulher, N. Freud, J M. Létang, J C. Poizat, C. Ray, and M. Testa. Monitoring the Bragg peak location of 73 MeV/u carbon ions by means of prompt-γ ray measurements. *Applied physics letters*, 93(9):093506, 2008.

[TestaM2010] M. Testa, M. Bajard, M. Chevallier, D. Dauvergne, N. Freud, P. Henriquet, S. Karkar, F. Le Foulher, J. Létang, R. Plescak, C. Ray, M.-H. Richard, D. Schardt, and E. Testa. Real-time monitoring of the Bragg-peak position in ion therapy by means of single photon detection. *Radiation and Environmental Biophysics*, 49(3):337–343, 2010.

[TestaMPhd2010] M.Testa. *Physical measurements for ion range verification in charged particle therapy*. PhD thesis, Université Lyon 1, October 2010.

[Todd1974] R. W. Todd, J. M. Nightingale, and D. B. Everett. A proposed γ camera. *Nature*, 251:132–134, 1974.

[Uche2012] C. Z. Uche, W. H. Round, and M. J. Cree. Evaluation of two Compton camera models for scintimammography. *Nuclear Instruments and Methods in Physics Research Section A: Accelerators, Spectrometers, Detectors and Associated Equipment*, 662(1):55 – 60, 2012.

[Wightman1948] A. Wightman. Note on Polarization Effects in Compton Scattering. *Physical Review*, 74:1813–1817, 1948.

[Wilderman1998] S. J. Wilderman, N. H. Clinthorne, J. A. Fessler, and W. L. Rogers. List-mode maximum likelihood reconstruction of Compton scatter camera images in nuclear medicine. *IEEE Nuclear Science Symposium Conference Record*, 3:1716 – 1720, 1998.

[Wilson1946] R.R. Wilson et al. Radiological Use of Fast Protons. *Radiology*, 5(47):487 – 491, 1946.

[Yamaguchi2011] M. Yamaguchi, N. Kawachi, N. Suzui, S. Fujimaki, T. Kamiya, H. Odaka, S. Ishikawa, M. Kokubun, S. Watanabe, T. Takahashi, H. Shimada, K. Arakawa, Y. Suzuki, K. Torikai, Y. Yoshida, and T. Nakano. Development of head module for multi-head Si/CdTe Compton camera for medical applications. *Nuclear Instruments and Methods in Physics Research Section A: Accelerators, Spectrometers, Detectors and Associated Equipment*, 648, Supplement 1(0):S2 – S7, 2011. 4th International Conference on Imaging techniques in Subatomic Physics, Astrophysics, Medicine, Biology and Industry.

[Zeng2004] G. L. Zeng, J. R. Galt, M. N. Wernick, R. A. Mintzer, and J. N. Aarsvold. Chapter 7 - single-photon emission computed tomography. In Miles N. Wernick and John N. Aarsvold, editors, *Emission Tomography*, The Fundamentals of Pet and Spect, pages 127 – 152. Elsevier Academic Press, San Diego, 2004.

[Zoglauer2003] A. Zoglauer and G. Kanbach. Doppler broadening as a lower limit to the angular resolution of next-generation Compton telescopes. In Joachim E. Truemper and Harvey D. Tananbaum, editors, *X-Ray and Gamma-Ray Telescopes and Instruments for Astronomy*, volume 4851, pages 1302–1309. SPIE, 2003.

[Zoglauer2011] A. Zoglauer, S. E. Boggs, M. G., M. A., P. N. Luke, and R. M. Kippen. Design, implementation, and optimization of MEGAlib's image reconstruction tool Mimrec. *Nuclear Instruments and Methods in Physics Research Section A: Accelerators, Spectrometers, Detectors and Associated Equipment*, 652(1):568 – 571, 2011. Symposium on Radiation Measurements and Applications (SORMA) XII 2010.